Electromagnetic Simulations of Exotic Phenomena in Engineered Materials

Tyler E. Dodge

A dissertation

submitted to the Faculty of

the Department of Physics

in partial fulfillment

of the requirements

for the degree of

Doctor of Philosophy

Boston College

Morrissey College of Arts and Sciences

Graduate School

August 2023

Electromagnetic Simulations of Exotic Phenomena in Engineered Materials

Tyler E. Dodge

Advisor: Chair: Professor Krzysztof Kempa, Ph.D.

ABSTRACT

"Simulations are like an experiment but on a computer." – *K. Kempa*. Powerful ideas can be explored in immense detail and unmatched flexibility through computational resources. Combined with the beauty of electromagnetics, worlds of situations and problems can be uncovered. Of the many interesting phenomena available to study, a relatively recent explosion of engineered plasmonic materials has benefitted greatly from numerical breakthroughs in simulating Maxwell's equations. Using these tools on novel metamaterial systems, composite materials with precisely designed structural features, the analysis and optimization probes the unique capabilities they have interacting with light. Example phenomena from this work includes fundamental principle breaking, extraordinary optical transmission, negative refraction, and superconductivity enhancement. The systems that harbor such outstanding feats fall into the umbrella term of metamaterials, each with distinct geometry and contrasting electrical properties that allow for an engineered control of the effective structural dielectric function. As the response to electromagnetic radiation, manipulating the dielectric function is key to creating and discovering the effects that control light, without changing any chemistry. This work scales pedagogically through the different types of metamaterials, beginning first with 2D planar checkerboard structures with highly non-linear percolation. In

combination with spoofed plasmonics, the longstanding symmetry of the Babinet principle is challenged. Layers of checkerboards are then stacked and translated to create subwavelength gaps for which plasmonic coupling between layers aids in optical transmission. In fact, there is similar physics controlling other layered quasi-complementary structures shown by comparison to experimental transmittance data. A further stage introduces photonic crystals constructed out of 3D periodic lattice of nanoparticles. Photonic band structure calculations for properly designed systems suggest the possibility of bandwidths of the IR spectrum where the crystal has a negative refractive index. Such a material property allows for the invention of lenses that beat the diffraction limit, applicable to subwavelength imaging. Lastly, non-local extensions to plasmonics are theoretically worked into expressions for superconductivity, creating a resonant anti-shielding effect, in composite topological crystal/superconductor layered arrangements. Applying this to known topics, like Bi_2Se_3 and MgB_2, show significant boost to electron pairing and thus rises in superconducting critical temperature. Central to all the systems and effects explored are the modifications made to the dielectric function of each effective medium. Supported by electromagnetic simulations and theoretical efforts, the listed engineered materials transform the dielectric environment purposefully to originate the discussed exotic phenomena.

"New scientific ideas never spring from a communal body, however organized, but rather from the head of an individually inspired researcher who struggles with [their] problems in lonely thought and unites all [their] thought on one single point which is [their] whole world for the moment."

- *Max Planck*

ACKNOWLEDGEMENTS

There is no limit to the amount of thankfulness and acknowledgment given to those who brought me to and pushed me through this milestone moment. For as much as I can express that in person, nothing is quite as satisfying as receiving a mention in the culmination of that hard work. In my opinion, a person gets a lot of influence from those around them throughout their life. Support can come in many forms, whether that is direct and emotional or unassuming and motivational. Without that influence we have on each other, positive and negative, our collective human progression would never be able to reach a fraction of the heights we've brought it today. That mark left on me by everyone is returned by a mark in this work. Even just by reading this section, I thank you. To start with the beginning, my family has always set me on the right track. My mother Carol and father Wayne have given me every opportunity to achieve success. There doesn't go a single day where I don't consider that benefit, nor do I ever take their hard work for granted. They've always set a good example, and though I have taken my own individual path, their lessons and influence will always hold weight. My friends, old and new, deserve their credit as well. It may be over doing it listing the names of everyone who I can trace back and credit with a defining moment. Since that would fill more pages than this body of work, I elect to extend a huge thank you to anyone I consider myself lucky enough to call a friend. For the direct contributions, all my friends through growing up, attending school, and playing hockey/games, I want to

explicitly recognize. Greyson Monroe, Dalton Eberharter, Collin Kinchen, Matt Komitor, make up a strong group of people that I hope hold similar weight in my success for years to come. My classmates, and specifically my grad school cohort, have been tremendous to learn alongside with. These are the people who I share the most common experiences with, each day pushing each other to all get to this same outcome. Mark Schiller, Vincent Plisson, Farank Bahrami, Matt Gochan, Gavin, Osterhoudt, Alex LaFleur, Yiping Wang, Eliza Greiner, Danielle Lafferty, and truthfully so many more are to thank. For those who have reached this point before me, I'm happy to have celebrated with you. And for those who are so close to finishing, I can't wait to celebrate with you. You all made every day so much better. All my groupmates who made my starting position as far along as it was and taught me their experience along the way like Alex Shvonski, Jiantao Kong, (especially) Xueyuan 'Shirley' Wu, and Victoria Gabriele.

Arriving at one of the grandest acknowledgments I could give, to my girlfriend and partner, Amanda Chu. She knows the same challenges and success that someone can experience in their grad school career, and while going through it all herself, was always there to support me. She continues to inspire me, with no lack of motivation to be my best self. At the time of writing, she is inching closer to her own finish line, and I can only hope to match the same energy, love and support she shared with me during this difficult process. Academically, many are to credit with my education. Whether in a formal sense or not, there isn't a learning moment I take for granted, as it presents a new opportunity. Learning makes me genuinely excited, for there is nothing better in my opinion than seeing the world in a new light. Of the numerous thanks I must give to my educators, Mr. Taylor sparked and pushed me to see the world for what it truly is... a bunch of vector arrows. His physics classes gave me the most to look forward to in high school and became the only thing interesting enough for

myself to consider as a college major. For the joys of scientific research, Dr. Kate Ross guided me through. Her mentorship and eagerness in the pursuit of scientific success rubbed off became the ultimate reason for my aspirations to get to the doctorate level. Along the way, I've discovered what it truly means to know something: to be able to describe and teach it to others. While learning is one thing I never plan to give up, I also hope there will be someone willing to hear my teachings as well. It has become a hidden talent for myself to teach and I'm thankful to each student I've had the pleasure of explaining my knowledge to. Boston College has been integral in facilitating my education and career, as a whole. The faculty of the physics department are gamechangers in the field and look to pass down their expertise without hesitation. I'll always be grateful for how welcoming of a learning space it has been with them. Some faculty of which make up a portion of my dissertation committee. I give special thanks to Prof. Michael Naughton and Prof. Kevin Bedell for their many dedicated efforts towards my progress. Also on my committee, Dr. Apra Pandey, is owed immense gratitude for her advice and discussions. In all, my committee is made up of proud scientists and true professionals that I thank greatly for their contributions. Certainly not least however, spearheading my committee and championing my graduate school career is my advisor Prof. Krzysztof Kempa. He is the type of person that makes you proud of your work. To me, he is the idealization of 'work hard, play hard' and has given me lessons in life beyond just physics. It is always great to find someone that you work well with and watch that effort blossom into scientific achievement that I couldn't be prouder of. He deserves my truest thankfulness and appreciation for all his mentorship. I thank you all once last time, especially you reader, and hope that my work can live up to the expectations of everyone who's been acknowledged and contributed.

TABLE OF CONTENTS

LIST OF FIGURES

Figure

LIST OF APPENDICES

Appendix

LIST OF ABBREVIATIONS

1D One-Dimension

2D Two-Dimensions

3D Three-Dimensions

AC Alternating Current

BCS Bardeen Cooper Schrieffer

BP Babinet Principle

BZ Brillouin Zone

CEM Computational Electromagnetics

CST CST Studio Suite

DC Direct Current

EOT Extraordinary Optical Transmittace

EM Electromagnetics

FCC Face-Centered Cubic

FDFD Finite Difference Frequency Domain

FDTD Finite Difference Time Domain

FEM Finite Element Method

FIT Finite Integration Technique

FTIR Fourier Transform InfraRed

HMM Hyperbolic MetaMaterial

IR Infrared

LC Inductance-Capacitance

NB-NSL Nano-Bridged NanoSphere Lithography

NIM Negative Index Material

NIR Near InfraRed

NRI Negative Refractive Index

NSL NanoSphere Lithography

PEC Perfect Electrical Conductor

PS PolyStyrene

RAS Resonant Anti-Shielding

RLC Resistance-Inductance-Capacitance

RPA Random Phase Approximation

SEM Scanning Electron Microscopy

SPs Surface Plasmons

SPPs Surface Plasmon Polaritons

SRR Split Ring Resonator

SNG Single Negative

TE Transverse Electric

TEM Transverse ElectroMagnetic

TLM Transmission-Line Matrix

TM Transverse Magnetic

UV UltraViolet

CHAPTER I

Introduction

Electromagnetics stands as a fundamental pillar of physics, something each and every student of physical sciences finds themselves repeatably thrust into the theory to gain the foundational knowledge. With several courseloads and possibly one the most infamous textbooks to a graduate student in physics[1], one can begin to recede any of the illusions that modern technology hides behind. As simple as some products may seem to the consumer on the surface, underlying are the complex exploitations of fascinating physical phenomena. Take your current model of cell phone as an example, a device, at its current numbers, out populates humans by nearly a factor of two[2]. At the core, a smartphone contains several electrical components combined so sophisticatedly the average user is nearly blind to fantastical feats of engineering that give it the versatile functionality we desire. This is just one of many modern marvels easily oversighted. Of course, supporting the base of these devices is electromagnetic (EM) theory. Wireless communication, integrated circuits, magnetometers, cameras, speakers, touch displays: only a few of the basic examples to get the mind jogging. All individual pieces that start out by thinking about the physical rules of nature, in particular EM, and transforming those properties into practicality. Steps like these are not taken overnight, the cumulative research

hours of many before progress into society. This dissertation is meant to serve as a collection of time and research that adds but a small drop into the large ocean of our collective human progression. By now, it can be understood that EM will be the core, critical machinery with which this research is built upon. There is no discussion of EM that doesn't involve or start without Maxwell's Equations (1.1a)–(1.1d). The detailed breakdown of the relevant background physics, including an understanding of Maxwell's equations is done in Appendix A, but for here, we simply need to come to the agreement with nature that classical EM is constructed by the Lorentz force law and Maxwell's equations[3]. Like any differential equations, for Maxwell's equations to adequately describe a situation, proper conditions and boundaries need to be defined, aslo see Appendix A. It should not be understated how amazing these four coupled partial differential equations (and the Lorentz force law) can be solved for a complete understanding about every problem in EM.

$$\nabla \cdot \mathbf{E} = \frac{\rho_e}{\varepsilon_0} \qquad \text{Gauss's Law} \tag{1.1a}$$

$$\nabla \times \mathbf{E} = -\frac{\partial \mathbf{B}}{\partial t} \qquad \text{Faraday's Law} \tag{1.1b}$$

$$\nabla \cdot \mathbf{B} = 0 \qquad \text{Gauss's Law for Magnetism} \tag{1.1c}$$

$$\nabla \times \mathbf{B} = \mu_0 \mathbf{J} + \mu_0 \varepsilon_0 \frac{\partial \mathbf{E}}{\partial t} \qquad \text{Ampère's Law} \tag{1.1d}$$

Now, there is no statement that this is always easy, of course. Complex geometries and enormous calculation domains come with the territory once you move past some introductory problems. Computation must come into play now. Maxwell's equations, depending at what form they are in, are programable to solve for the electromagnetic interactions and dynamics for a given environment. Computational electromagnetics (CEM), as the field is referred to as, is a process of modeling and calculating electric and magnetic field dynamics for systems that

are too rigorous to solve analytically. Correct, these solutions are approximate, most of the time, but have proven to be excellent in agreement with the physical world[4]. There exists over a dozen commercial and open-source programs and algorithms for CEM[5][6], each with unique advantages. Appendix B specifies the particular software and algorithms used throughout this dissertation and an overview of how each transforms Maxwell's equations and a geometry into specialized understandings of the EM. Dassaault Systemes publishes a commercial CEM software, under their Simulia brand, called CST[7]. Through this software working as this body of work's primary computational tool, we're allowed to explore challenging and novel EM with trusted accuracy and reasonable effort. Having reliable simulations as a mechanism leaves an open world for exploring and understanding electromagnetic phenomena. This study now becomes a matter of which EM and systems to analyze. Each CEM software has its own individual technical limitations, but in general the forefront of discovery is marked at these. The symbiotic relationship with commercial CEM software and research help further both. Recent advancements in nanofabrication and graphene for example have pushed demand for development from software publishers, while terahertz devices and metamaterials have received critical insight from CEM[8]. Specific shortcomings to some algorithms is discussed elsewhere, Appendix B, but speaking broadly, the scope of CEM improvements is focused towards higher frequency and multiphysics applications, bettering computational performance (such as time and memory usage), and multiscale models (where the wavelengths of interest have changing comparisons to the model feature sizes). In this dissertation it will become apparent that most of this work pushes close to one or more of these general CEM limitations, all because it's the perfect setting for new and interesting physics. Beginning in Chapter II, structures that make up periodic lattices of metallic squares exhibit

principle challenging transmission effects in optical and near-infrared (NIR) frequencies. These structures can be seen as a checkerboard pattern in the perfect scenario and host plasmonic effects that extend criteria to the Babinet principle. The relatively short light wavelengths go through stretches of being smaller, larger, and comparable to structure sizes, posing unique simulation challenges. This leads nicely to Chapter III, that takes optical transmittance effects to an extraordinary level. As an expansion on the Babinet principle within the checkerboards, multi-layered structures add another dimension to the physical phenomena taking place. Bi-layered, complimentary structures facilitate extraordinary optical transmittance (EOT) effects at infrared (IR) wavelengths, being placed in a similar computational territory as the checkerboard structures with added geometrical complexity. The following chapter, Chapter IV, continues the three-dimensional (3D) structure nature by exploring photonic crystals in similar optical and NIR frequency ranges. Purposeful design of the geometry and materials in these photonic crystals opens windows of negative refractive index (NRI) in the simulated band structure. Calculated in a different CEM algorithm, these structures push the current limits of 3D EM simulation because of the feature size comparisons to the wavelength and sheer size of the calculations. To conclude, Chapter V once again stretches the expectations of commercial CEM software by considering non-local effects. Tying certain effects of metamaterials to superconductivity provides new schemes and calculations for superconducting critical temperatures with dramatic results. Each chapter beyond being tied to CEM should also require an introduction to several key players in these systems and effects. In those short chapter descriptions, there are some technical terms and buzzwords, explained in further detail within the specific chapter, but the common threads are continued here.

1.1 Dielectric Function

Electromagnetics is already quite interesting in the absence of a medium. An easily overlooked power but immensely critical understanding in EM, electromagnetic waves can and do propagate in a vacuum. Important when thinking about light and radiation reaching the Earth from the Sun across roughly 150 million kilometers of empty, medium-less space, but consider most interactions on Earth occur within a medium of some sorts. This is where we build upon the foundations built in Appendix A and beginning now with EM inside matter. Constitutive relations, describing a physical quantity in the specific context of its response in a material versus without, of Maxwell's equations form the macroscopic viewpoint in Equations (A.10a)–(A.10d) where bound charges have been wrapped up in displacement and auxilary fields, leaving the free charges explicit. These relations can heavily depend on the material in question. A large change from the microscopic Maxwell equations is the introduction of the displacement field $\mathbf{D}$. The relationship to the electric field is straightforward,

$$\mathbf{D} = \varepsilon_0 \mathbf{E} + \mathbf{P} \tag{1.2}$$

where the electric field $\mathbf{E}$ summed with the polarization $\mathbf{P}$, a density of the total electric dipole moments inside the material. Now becomes the moment of divergence depending on which materials we are talking about and those specific discussions are to come. For the sake of an understanding of the displacement field, we can strictly speak about linear, homogeneous, and isotropic dielectric that has instantaneous responses to electric field changes. With this list of qualifiers, the polarization density in our material can be written in terms of a

direct proportionality to the electric field,

$$\mathbf{P} = \varepsilon_0 \chi \mathbf{E} \tag{1.3}$$

where χ making up the proportionality constant is the materials electric susceptibility. This allows a direct relationship between the displacement and electric fields

$$\mathbf{D} = \varepsilon_0(1 + \chi)\mathbf{E} = \varepsilon \mathbf{E} \tag{1.4}$$

and to clarify the pre-factors describing the material permittivity with $\varepsilon = \varepsilon_0 \varepsilon_r$ and $\varepsilon_r = 1 + \chi$. We can see now that the manner of how the displacement field behaves is directly related to the behavior of the electric field. Most materials don't obey all the qualifiers set out to derive this relationship, so we can begin to peel back on those. For example, taking an anisotropic material instead turns the constant ε into a matrix, while nonhomogeneous materials deal with a position dependent permittivity. Interesting avenues to pursue in their own right, but let us consider striping back the qualifier about instantaneous time response of the internally induced electric fields. It is quite natural to suppose that when an electric field is imposed on a given media that the resulting polarizations of the molecules or atoms take some time to adjust. Albeit quite quick[1], just not immediately. In such a case, the response function is the electric susceptibility and when combined, in mathematics one would use convolved instead, with the imposing electric field, the polarization density can easily be described in terms of frequency. Following some mathematical rigor involving a Fourier transform and we arrive at the following relationship of $\mathbf{D}$ and $\mathbf{E}$,

$$\mathbf{D}(\omega) = \varepsilon(\omega)\mathbf{E}(\omega) \tag{1.5}$$

qualified that the medium is linear and time-invariant, as well as the response is local. We see that the constant permittivity that we started with has now turned into a function of frequency ω. At this point, it becomes safe to call this permittivity the dielectric function. It should also be stated that the dielectric function in totality is not only a function of frequency but wavenumber as well. This will be explored more with non-local systems in Chapter V. A medium having a dielectric function is also described as material dispersion, a description for the behavior of light waves propagating within the medium. The colloquial view for light dispersion is the best-selling Pink Floyd album art for The Dark Side of the Moon, where white light is slowed and spread within a material to create the colorful rainbow on the other side. This is expected for optical frequencies like glass for example because of material dielectric properties cause different behaviors for differing frequencies. Many elementary problems in EM will deal with a dielectric constant ε, because of the consideration that the frequency band in question is narrow enough that the frequency dependance is negligible. However, understand that in general all materials have a dispersion. Why? The physical world is constrained by causality, mathematically known as the Kramers-Kronig relations.

$$\varepsilon'(\omega) = \frac{1}{\pi}\mathcal{P}\int_{-\infty}^{\infty} \frac{\varepsilon''(\omega')}{\omega' - \omega}\, d\omega' \tag{1.6}$$

$$\varepsilon''(\omega) = \frac{-1}{\pi}\mathcal{P}\int_{-\infty}^{\infty} \frac{\varepsilon'(\omega')}{\omega' - \omega}\, d\omega' \tag{1.7}$$

Without diving too deep into complex analysis, these Kramers-Kronig relations in Equations (1.6)–(1.7) can be thought of as synonymous with causality. Taking some complex response function, the dielectric function in our case, the real and imaginary parts can be interchangeably computed with one or the other. The

special catch is that the function needs to be analytic and a function like this being analytic implies causality in the physical system being described by the function[9]. A little circular, but the argument boils down to a response function is a causal function and is therefore analytic. One can then use the Kramers-Kronig relations, needing analyticity as a requirement, and imply the system is then therefore causal. A small divergence into some complex analysis but we return back to the dielectric function knowing the rather simple statement that for there to be any change in the internal electronics of a material, there must first be a change in the applied field i.e., causality. Now that we are constrained by the rules of time and the limitations have been set on the frequency dependence of the dielectric function, we can ask: What does it look like? We see now the polarization of a material, a constitute of the

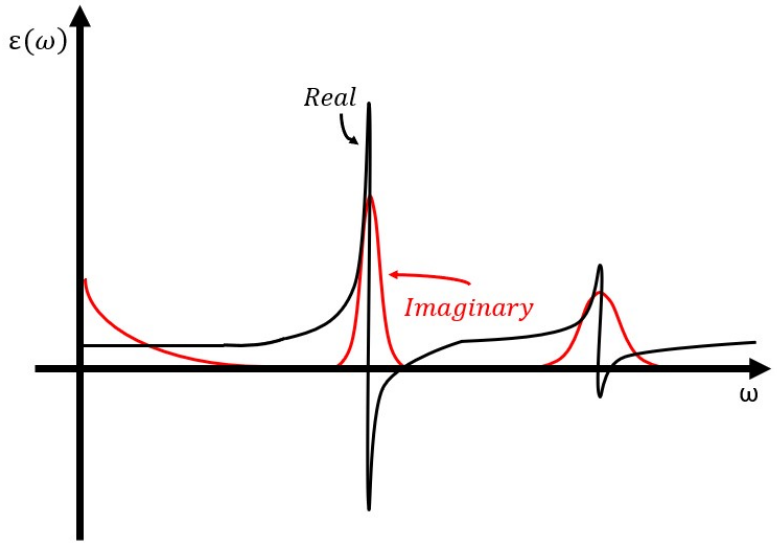

Figure 1.1: -
The example model of the dielectric functions behavior as a function of frequency, containing the exaggerated features at resonance and low/high frequency. The black curve is representative of the real part, while the red illustrates the complex (imaginary) part.

dielectric function, can only depend on electric fields at prior times, let's look

into the frequency dependence. The frequency under study is that of the externally applied electric fields, light for example. Shown in Figure 1.1, is an example plot describing the dielectric environment. Because the dielectric function is representing the phase difference between the applied and induced fields, it becomes convenient to describe it within the complex number language. Plotted are the real and imaginary parts of the dielectric function as a function of frequency in some example medium. Starting at low frequency, this is the static limit where most of those introductory EM homework questions lie. The real part of the dielectric function remains a constant for all intents and purposes. Imagine an external electric field applied to a material that is oscillating very slowing. This gives the corresponding displacement field, causally lagging, enough time to keep up with the oscillations. There isn't much of a time delay in this scenario. If we go to the high frequency limit, the dielectric function approaches another steady, constant state where the real part levels off at a value referred to as ε_∞. In this limit, the situation imagined before changes to the external electric field, now so rapidly oscillating that the summation of all the little fields induced in the molecules and atoms comprising the material can't react in time. The electric field changes back and forth so quickly that the polarization in the material almost becomes frozen. By the time the internal fields react to the external changes, it is already too late because the external field has once again already changed. So these fields instead choose the happy medium and hold in place, letting the external electric field continue its rapid oscillations. It is only more interesting as we shift to some more dynamics at the in-between frequencies. Examining this region on Figure 1.1, there are some noticeable behaviors in the dielectric function that might seem bizarre at first glance, some bumps and wiggles. As a rather complicated function, describing the entire frequency dependent dispersion of a material, the dielectric function

rises and falls at specific frequencies because of resonances with the medium. Generally, these can be attributed to dielectric relaxations or atomic and electronic resonances depending on the frequency scale. Isolating one of the

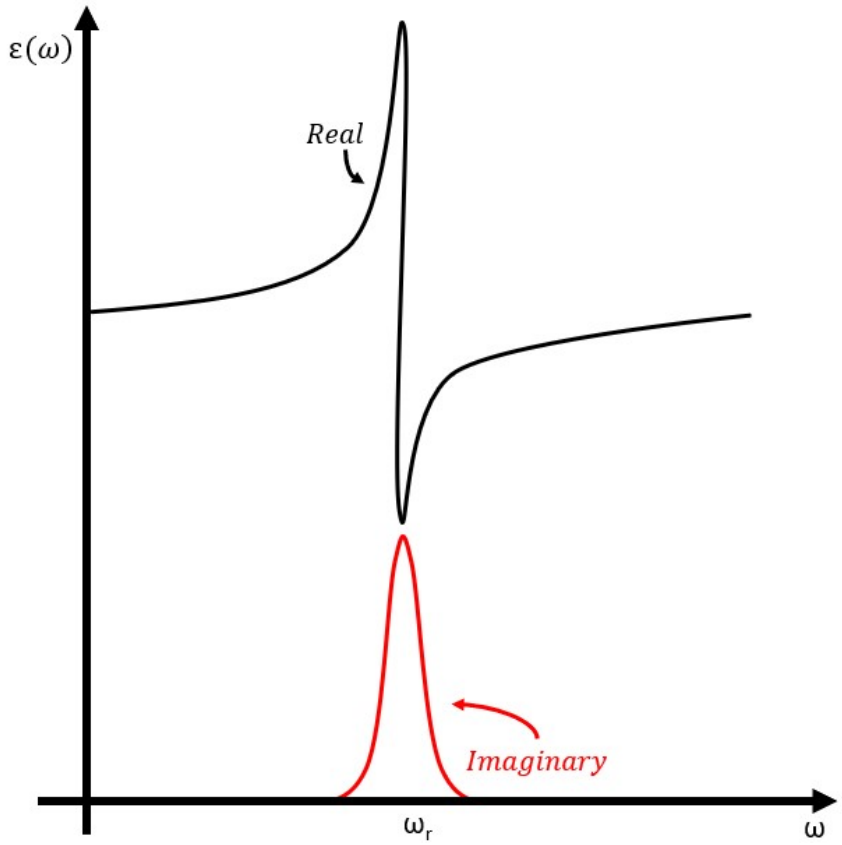

Figure 1.2: -
Zoomed view of one particular resonance, located at ω_r of the model dielectric function. The black curve is representative of the real part, while the red illustrates the complex (imaginary) part and are offset from each other for visualization.

resonances in the dielectric function, as shown in Figure 1.2, we return to a microscopic description of the charges within the medium. On the left (lower frequency side) of the resonance, the internal electric field arising from the polarization will be countering an external electric field. The real part is sharply increasing because the polarization process intensifies its response. Recall that the permittivity built into the dielectric function is considered a measure of the

strength of the relationship between the electric field and polarization. The exchange between the two quantities bolsters, thus the permittivity increases. This is described as a screening effect of these fields within the material. To personify the situation a bit, the individual charges are feeling a weaker electric field because the local electric field created by the responding other charges is neutralizing some amount. This happens until we reach the singular resonant frequency, ω_r, where there is more contribution from the imaginary part. Aside from these resonant frequencies, the dielectric function is approximately real. We call this normal dispersion, where the real part is linked to increase as a function of frequency. Now here at the resonance, the imaginary part becomes substantial, and by Kramers-Kronig decreases the value of the real part. Having a significant contribution from the imaginary part represents, physically, appreciable EM energy dissipation in the material. Any decrease in the real part like this is referred to as anomalous dispersion, nomenclature mainly used in optics such as the aforementioned Pink Floyd prism. Returning to the microscopic description, the charges in the medium have found a particular frequency in which their oscillations and the oscillations of the external fields are resonant. This causes the sharp spike seen in the dielectric function because of the strong amplitude gains from being in resonance. Once on the other side of the peak, the charges find themselves attempting to keep up with the external fields but ultimately lagging behind once again. So much so, the field produced by the charges goes from being nearly completely out of phase to suddenly so far out phase that they have returned back to being in phase. Around a 360 degree phase delay at this point has the two electric fields working together instead of against each other. Instead of the screening effect before, this region harbors the opposite anti-screening effect. A resonance can be associated with absorption in this picture. This section has cartoonishly described the physical meaning of the

dielectric function, of course painting over details with a broad brush. Certainly, there has been little distinction between an insulator, full of bound and polarizable charges, and a conductor, possessing extra charges with available states to freely move to. This is purposeful. In the context of describing the behavior of the dielectric function, and soon to see its relationship to conductivity, especially in the static limit, the distinction is blurry. The dielectric function plays the role in this story as the 'costume' each medium 'wears'. Distinct and unique to them all and can even be artificially modified.

1.2 Plasmonics

Our previous description of the dielectric function was more conceptual. Now to explore this in specific media, we can dive into some of the mathematics more. In the simplest model of the dielectric function, the equation of motion

$$m[\ddot{\mathbf{x}} + \gamma\dot{\mathbf{x}} + \omega_0^2\mathbf{x}] = -e\mathbf{E}(\mathbf{x}, t) \tag{1.8}$$

comes from taking Newton's second law for an electron charge restrained by a restoring force in an external electric field with some damping term coming with γ. A couple standard approximations are taken, where effects from magnetic fields are ignored and these harmonic oscillations are of small amplitude. The primary purpose of these simplifications is to give a more averaged-out viewpoint for the bound charge. Differential equation analysis suggests to solve this equation of motion by considering solutions of the same form as the driving force supplied by the electric field. The cases we care to consider are for electromagnetic waves with a field varying harmonically in time with frequency ω. For one electron in this scenario, we now have a solution for the average

position.

$$\mathbf{x} = \frac{-e}{m}(\omega_0^2 - \omega^2 - i\omega\gamma)^{-1}\mathbf{E} \tag{1.9}$$

Broadening to the whole medium now with N molecules per unit volume, each with Z electrons per molecule, we take Equation 1.9 into a dipole moment and create an equation for the electric susceptibility. As we've seen previously the relationship with the electric susceptibility, the dielectric function takes the form

$$\varepsilon(\omega) = 1 + \frac{4\pi N e^2}{m}\sum_j f_j(\omega_j^2 - \omega^2 - i\omega\gamma_j)^{-1} \tag{1.10}$$

where we can generalize to many binding frequencies ω_j and phenomenological damping constants γ_j for f_j electrons in each molecule. This needs to be restricted by a sum rule where $\sum_j f_j = Z$ and voila, we have a manageable mathematical description of atomic contributions to the dielectric function. To the keen trained eye, it becomes quite clear where the low frequency, the high frequency, and the resonant behavior arise from. In low frequency, contributions from the sum are generally small and positive because the frequency factor in the denominator will be positive for $\omega < \omega_j$. But as more terms in the sum contributing and the frequency increasing to a point beyond $\omega > \omega_j$, the denominator term begins to make negative contributions. Lastly, in the resonances where $\omega = \omega_j$, the denominator vanishes for the real part, while the imaginary part dominates. Not bad for a simple model. There are no additions or changes needed for the qualitative description in the previous section now that we have some mathematical basis. Instead, we can further expand, specifically into charges (of course at this point we can call them what they are inside materials, electrons) that are considered 'free'. The label 'free' for these electrons simply means that they are not particularly bound to an atom. The atoms that

make up the material are organized and bonded in a way that there are loose electrons in the outer shells that have no assigned task. So these electrons form a 'sea' of delocalized charges that can go wherever they are needed. Of course, the type of materials referred to here with such a sea of electrons are labeled conductors or metals. For the purposes of this dissertation, we can avoid the nuance of here about quasiparticles and effective mass[10]. The important thing, instead, is when a fraction of electrons (per molecule) f_0 are free, we can separate the contributions in the dielectric function based on the descriptor of electrons. The previously derived expression in Equation 1.10 becomes

$$\varepsilon(\omega) = \varepsilon_0 + i\frac{4\pi N e^2 f_0}{m\omega(\gamma_0 - i\omega)} \tag{1.11}$$

where the lump contribution of all other dipoles in the medium are ε_0. We are all but a few simple steps away from the famous Drude model for conductivity that, as an aside, which can be seen with detail[11]. The takeaway for the dielectric function for this context is the relationship with conductivity. Importantly for computational purposes, is that for a dispersive description of a medium there are two equivalent attributes: a complex dielectric function or a dielectric constant paired with a frequency dependent conductivity. Either will work accurately and makes creating a simulation model from experimental data rather straightforward. Armed with the model dielectric function in Equation 1.11, we can venture into plasmonics. By taking the limit of frequencies well above all the resonant frequencies in the dielectric function, a simplification seen in Equation 1.12 comes out where we've grouped together some material properties, like n the charge carrier density, e the electron charge and m_* the effective carrier mass, and call it the plasma frequency, Equation 1.13.

$$\varepsilon(\omega) \simeq 1 - \frac{\omega_p^2}{\omega^2} \tag{1.12}$$

$$\omega_p^2 = \frac{4\pi N Z e^2}{m} \tag{1.13}$$

There are many ways to think about the concept of a plasma frequency for a material but we see its consequences every day. Mirrors are one example to conceptualize plasma frequency. To start, given Equation 1.12, there imposes a limit of k the wavenumber.

$$\omega^2 = \omega_p^2 + c^2 k^2 \tag{1.14}$$

Just like frequency is thought of as the inverse to a period (not how much time to do one wiggle but how many wiggles in a unit time), wavenumber is analogous but for wavelength (not how long in distance is a wiggle but instead how many wiggles are done in a unit distance). When someone discusses a dispersion relation, they generally mean this, a frequency that is a function of wavenumber. Free space light propagation in a vacuum is the simplest example to compare to where $\omega = ck$. A standard linear line with the speed of light as the slope, known as the light line. Referencing 1.3, the plasma dispersion relation at zero frequency begins with the value ω_p and increases from there. For there to be any kind of mode or propagation of a mode, there needs to exist a dispersion relation. With there being nothing of the sort besides the standard light line below the plasma frequency, then these modes are forbidden to propagate, the wavenumber is purely imaginary. This would manifest in the macroscopic as a material (i.e., a metal) that is reflective below this frequency and can be transparent above. A mirror happens to have a plasma frequency above optical such that to us it appears reflective but 'see-through' at much higher energies like the ultraviolet (UV) spectrum[12]. The nice thing about this formalism is that this critical frequency is purely a property of the medium, which makes creating simulation models once again easier. The modes that do follow the

dispersion in Equation 1.14 do have a name. They go by as bulk plasmon waves or just 'plasmons', propagations of collective charge oscillations in the metal. Like other waves, they can be transverse or longitudinal where the latter only arises for vanishing dielectric functions. There are also other ways for these collective charge oscillations to propagate. For example, there is also a dispersion for surface plasmons (SPs) that propagate on metallic-dielectric interfaces[13], seen as well in Figure 1.3. This lower branch of the plasmon dispersion is long

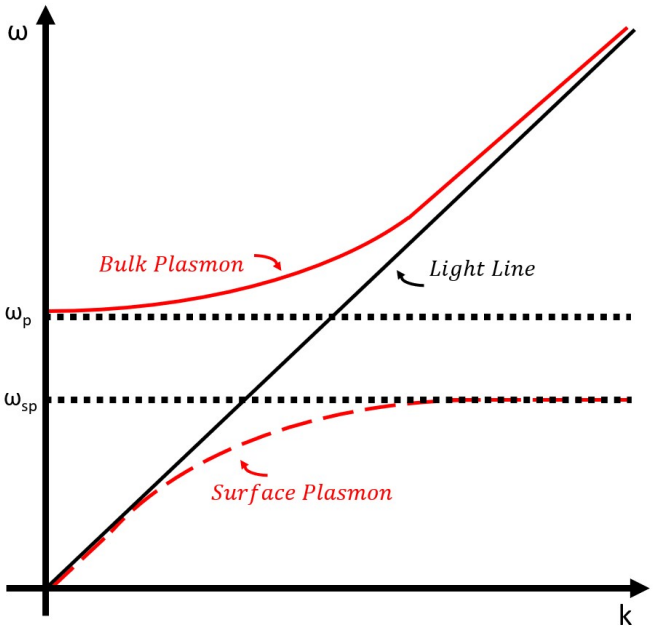

Figure 1.3: -
A dispersion diagram shows the phase space of frequency (energy) versus wavevector. Plotted in red are the dispersion constraints for bulk (solid) and surface (dashed) plasmons where each is asymptotic to a particular plasma frequency and the light line, shown in black.

lived unlike the upper branch where re-radiation occurs, thus sometimes giving the distinction of bound and radiative modes respectively. Many other mechanisms can hybridize the plasmon modes, most commonly, interacting with phonons[14], teaming up with single electrons[15], and coupling with light to establish the surface-plasmon-polaritons (SPPs)[16]. Each of these various

couplings can augment system properties depending on the underlying mechanism, such as optical and thermal. The optical transparency, as discussed in the context of mirrors, is governed by the bulk plasmons[17] where we view the medium as a large structure when compared to the wavelengths of the incident radiation. However, different aspects come to the forefront when we discuss the more interesting limit of metallic structures with sizes comparable to the wavelength. Boundaries become the overseeing factor now due to the confinement of sea of electrons to specific spaces. To continue this analogy, in large structures the ocean knows really no bounds and gives the appearance of endlessness, being lost at sea for example with no land in sight. In a confined space now of smaller structures, we examine mechanics much closer to shore where the sea of electrons is confined. These smaller structures can be labeled as 'plasmonic structures' and instead have the optical properties and physics controlled by the surface plasmons. It is no stretch to think that a plasmon bound to surfaces of metals will have a sensitivity to the geometry of those surfaces. It becomes our goal now to explore the limits of what is possible for the material optical properties through manipulation of the surface geometries.

1.3 Metamaterials

The electromagnetic spectrum is quite long with many different subdivisions, shown in Figure 1.4. Each region has its own use with a multitude of reasons why or why not. The ends of the spectrum are capped by the inverse relation between wavelength and frequency, where for light in a vacuum goes like $c = \lambda f$. One end of the spectrum is bounded by zero frequency, our static limit, having electromagnetic waves with very long wavelengths. On the other end, wavelengths can get extremely short, with high frequencies which is related to high energies. Everything in between has amazing functionality and unique

advantages but, to keep the motivation of this work simple, there is no stretch of the spectrum as relatable as optical. Naturally, due to the visible spectrum of humans (between 380 and 750nm (788 and 400THz)), it is easy to find this region as intuitive and less abstract. It's safe to say that this is that way because of our scale when compared to that of the EM radiation. Once we venture down

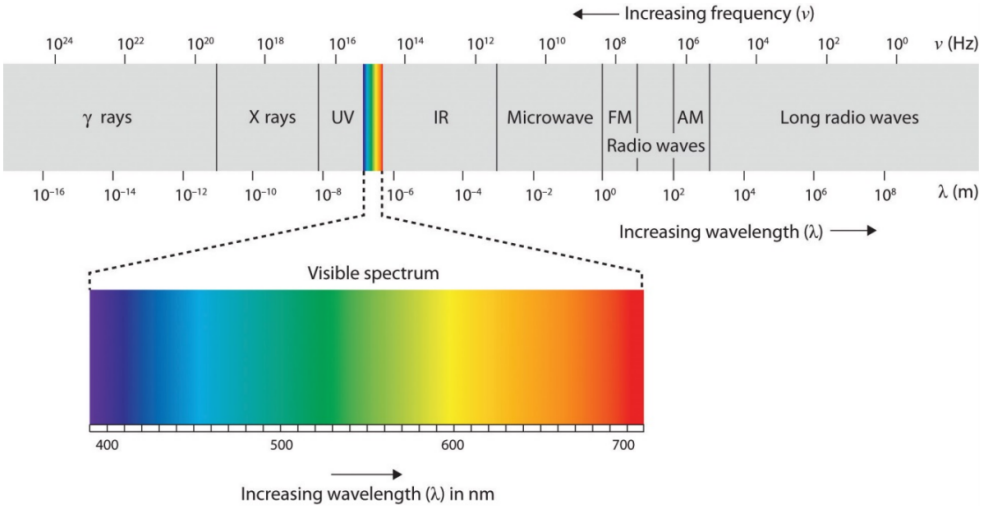

Figure 1.4: -
Labeled illustration of the electromagnetic spectrum with shortest wavelengths/highest frequencies on the left and longest wavelengths/lowest frequencies on the right. Inset is a zoomed-in scale of the visible spectrum with color representation. Image credits[18].

to a scale comparable to that of the wavelength of light, the interactions can be explosively compelling. Exceeding scales beyond the wavelength for the size of objects and structures only compounds the fruitful physics. As mentioned, any region of the EM spectra can be probed, but for the purposes of this discussion, we will narrow in on the IR, TeraHertz, and visible windows generally thought of as optical. One reasoning behind this is the ever-evolving achievement of fabrication of structures at the scales comparable to the light in these spectral windows. The field of nanomaterials and nanofabrication aren't quite at the full commercialization stage yet[19] but are becoming commodities[20]. With the

assistance of CEM software, discovering the possibilities of the rare optical properties in these nano-scale systems has never been more approachable. The general sentiment being that with CEM software, many iterations of design and tuning can be done cheaply and quickly before moving into the challenges faced with fabrication of structures so small. With the solid agreement known between CEM and experiment, this can be used predictively. The limitations are only ingenuity and the laws of physics. Of the progressive ideas in the world, from this field stems some of the more incredible and science-fiction-like realizations. The works of manipulating light such that an object can be transparent in particular frequencies. Actual cloaking technology where an object is engineered to guide EM waves in such a way that the object is camouflaged as if it were not there[21]. This work[22] is considered the one of the sparks that ignited this field roughly 15-20 years before the writing of this dissertation. Along with stealth technology, there is superlens technology that has been well explored[23]. To push past the theoretical bounds thought to cap the furthest resolution of imaging, the diffraction limit, a superlens can be designed to achieve resolution beyond this[24]. The list continues to perfect absorbers[25], antenna improvements[26], radar cross-section reduction[27], and much more. The common thread to the physical accomplishment of all these technologies is metamaterials. Given the Greek prefix 'meta' to denote the meaning of 'beyond' because these materials go past the capabilities of standard media. Metamaterials are composite, signifying that they've been purposefully engineered. The goal in mind is to provide material properties otherwise not attainable in ordinary materials. However, the catch is the novel properties are derived from physical structure, not chemistry. Usually the constructed geometry is arranged in repeating patterns with the crucial element scale being smaller than the wavelength of interest. In this scaling, large wavelengths, when compared to the geometric scales of the

metamaterial elements, will see the whole material as one homogeneous effective medium. After precise design and fine tuning of the geometric parameters, the metamaterial is adequate at influencing the behavior of incident EM radiation to a specific designed purpose. Whether that purpose is for cloaking or beating the diffraction limit is entirely up to the design and creativity input. With the realm of possibilities seemingly endless and many ingenious concepts realized, one may wonder where there is to move forward. It is not quite the picture painted here, the hidden 'Gotcha!' moment has been lurking. In the current state of nanofabrication, there are numerous restrictions on the possibilities that can be made useful. For example, there exists no fabricable cloaking technology for optical wavelengths. The science fiction dreams of wearing a coat and suddenly disappearing from sight are still just dreams, at the timing of writing. However, the concept is scalable. The references provided show working concepts for other windows of the EM spectrum, microwave for example. To get devices down to the scale to become meta-media for visible light, there needs to be manufacturing on the tens of nanometers scale, which just hasn't been achievable. The driving idea of metamaterials is still the core working principle and new concepts will continue to push the boundaries as the need arises. The metamaterial label can specifically imply certain geometries and is generalized to meta-media, nonetheless it is still common to use those terms interchangeably as will be done here. It is not by chance that one can think up a metamaterial design, simulate the EM effects, build a working prototype, and now have some revolutionary technology. Light interacts in specific and calculable ways with meta-media, generally following one simple analogous model, an RLC circuit. One signature metamaterial design pattern, the split ring resonator (SRR)[28] uses metallic features to create miniaturized versions of these circuits. As shown in Figure 1.5, the ring models the inductor (L) behavior as a storage device for

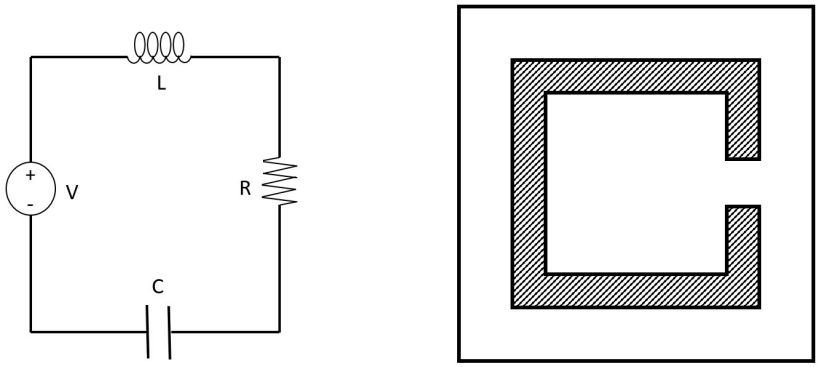

Figure 1.5: -
Left: Circuit diagram of a series RLC circuit that is analogus to disappating electromagnetic oscillations. Right: A single unit cell a split ring resonator metamaterial design that repeats as a lattice. The shaded region represents a metal while the surrounding is the contrasting dielectric material, usually in a stacked fashion. The placement of metal and dielectric can easily be reversed as well.

magnetic energy while the open split section acts as the systems capacitor (C) storing electrical energy. Naturally the resistance comes from having constructed a design with a metal of finite conductivity, meaning that there is loss or a resistance (R). Of course, in simulations however, we can take a perfect metal and return to a more perfect case LC circuit model. The voltage source for this circuit is the incident light where the oscillating EM fields work like an AC voltage source and induce a current. Signature to an LC (or RLC) circuit would be the resonant frequency $\omega_0 = \frac{1}{\sqrt{LC}}$ that only depends on the values of the circuit elements. Note that adding the resistance just adds damping, so we will stick with LC circuits for the moment. In circuits, capacitance and inductance are purely geometrical quantities that are designated by the size and shapes of the elements. So in metamaterials, we get back to the central definition that these special properties are arising solely from geometry. When the light, working as the AC source, has a frequency tuned to the resonant frequency of

the circuit, that is where large amplitude EM effects can take place. Harnessing the magnifications of those fields is how metamaterials are able to manipulate light. There are several other models and equivalent analogies for other types of metamaterials, but the LC circuit is central to the definition. The big picture is to bring plasmonics into play and return to the idea of confinement and dipoles again. Taking the metallic elements of the metamaterial and shaping them in a way such that the metal can act in an isolated fashion is one design technique. Effectively making small polarizable dipole elements that work in the same way the bound electrons in an insulator would, except on larger scales with stronger fields. The specific interaction at play defines the class of metamaterial, such as negative refractive index (NRI), single negative (SNG), hyperbolic (HMM), bandgap, and so on to name the primary few to this work. Each class is further defined and elaborated in the chapters relevant. Having a theme centered around manipulation of the dielectric function that represents the effective meta-medium ties back to the previously used personification for the dielectric function. We see now that metamaterials are purposefully designed, which changes the dielectric function that acted like the costume for a material. It contains all the useful information to how the material will respond to EM fields. Now with meta-media, that costume can be easily swapped out to serve many different purposes. At the intersection of all the topics discussed in this introduction lies the crux of the research within this dissertation. Using CEM software, alongside analytical EM theory when applicable, this dissertation approaches the modulation of the dielectric function through the geometric design of metamaterials to achieve enhancement of desired plasmonic effects that can create novel, exploitable optical phenomena. The chapters each approach this general idea from a unique aspect and individualized outcome, featuring published, unpublished, and yet-to-be published work.

CHAPTER II

Periodic Plasmonic Checkerboard Series Structures

2.1 Checkerboard Structures

One of the most fascinating components about plasmonic meta-media is design. There is an art to it that isn't captured completely by rigorous theory. It is sometimes seen as a rarity in science but rest assured, artistic vision creeps into many facets of scientific research. For example, most would consider material synthesis to involve a lot of creativity. Device fabrication is right up there too. There takes a certain touch and vision that a lot of success in these fields can be attributed to Reference [29]. By reading through the literature in the metamaterial field with this in mind, the origin of various abstract designs makes a little more sense. Every physicist comes to understand how a capacitor and inductor work. From those building blocks, next is how those components work when together. That abstract idea is conceptualized via circuit diagrams and schematics but, breaking that mold and applying those concepts in other ways is the challenge that design and creativity make their mark. Thus forms the split ring resonator (SRR) metamaterial, Appendix A goes deeper into the background electromagnetics. So simple yet sophisticated, and the SRR achieves

the exact design outcome. It doesn't stop with the SRR design, the literature[30] has rapidly expanded since a lot of the early work introduced in Chapter I. The general outline starts with a goal in mind, what is this device meant to do, what purpose will it serve. That can be thought of in terms of applications or on a fundamental research level. Then it is asked, what designs and features get to that outcome. How complex does the geometry need to be or is the simplest way the best way. This can take fabrication limits into account but leads to the ultimate exploratory tool, CEM. Countless iterations can be simulated and explored at a fraction of the effort. With the path forward outlined, let's start at the beginning.

2.1.1 Basic Checkerboard Series

Chronologically, this section of the work was not the starting place but is the intuitive beginning that will lead into the other chapters. This is an example of when ambitions are too large, and one must take a step back to analyze the simplest case. The goal is to computationally explore various plasmonic resonant features created by geometrical conditions. Having the simplest structure makes it realistic to have a complete understanding of the dynamics at play in the system. Checkerboard designs have been studied in the literature[31] because of its interesting tie to the Babinet Principle and as a critically percolated structure, both of which are further defined below. Part of the intrigue of the checkerboard as a plasmonic structure is in its simplicity, possessing that geometric beauty humans have had design interest for centuries, well before even the invention of chess in the 6th century. The pattern of repeating squares of two competing domains is the minimalist's idealization. With plasmonics in particular, those differing domains form the borders that surface plasmons call home. Consider the light squares of a checkerboard as the dielectric, vacuum,

while the dark squares represent the metallic material. Each square is nearly isolated from all its similar neighbors, with only the corners just barely touching. In that configuration, the canonical checkerboard is referred to as the perfect checkerboard, shown in Figure 2.1 middle panel. For many reasons, to be discussed throughout this chapter, the perfect checkerboard exists mostly as a concept. On nanofabrication scales, it is currently a challenge to achieve such precision to have the corners of a square matched up with the precipice of every single other square. Even computationally, the perfect checkerboard falls into a bifurcation to where the squares must either be connected or isolated, leading to strong numerical instabilities. Typical failings in CEM algorithms are attributed to iterations being exponentially sensitive to initial conditions due to the chaos of a singular geometry. In the classic logistic map problem, this would be thought of as a Lyapunov exponent[32]. Because of these issues, studying this system requires taking another approach, rather than the perfect checkerboard. There are related structures that can be obtained by fixing the center positions of each square, then subsequently adjusting their sizes. The first side is to reduce the size of the dark squares while increasing the size of the light squares, uniformly adjusting the edge lengths by the same fraction. Exampled in Figure 2.1 left panel, the dark squares have become islands in a connected sea of light. Countering this by doing the opposite adjustment of sizes, where the dark squares grow and the light squares shrink, there is the complementary structure. The diagram of Figure 2.1 right panel illustrates the dark squares taking over and leaving holes of light behind. One side, the first, is referred to as the island structures while holes structures is the label for the other.

To formally give geometrical definitions to the adjustments made of the square sizes, begin first with the perfect checkerboard case that will act as the barrier between the two sets of structures. Since this is just simple scaling, let's

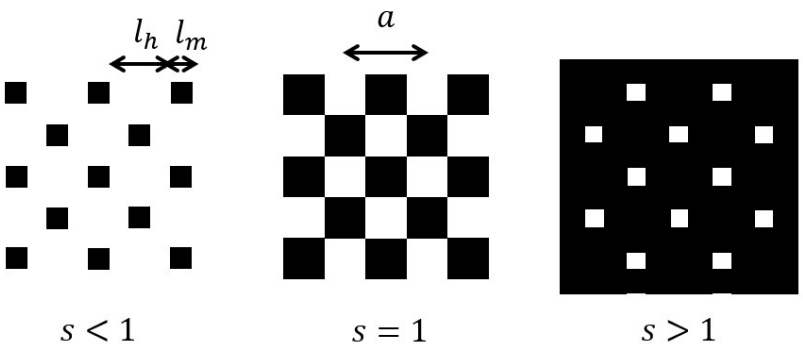

Figure 2.1: -
An example for each phase of the percolation checkerboard structures with center to center distance a and metal and hole edge lengths l_m and l_h respectively. Left: Underpercolated where the scaling parameter is less than one, creating metallic islands. Center: The perfect checkerboard existing right at the threshold. Right: Overpercolated where the scaling parameter is greater than one, creating holes in a metallic sheet.

introduce a scaling factor s that by definition is bound by the condition $0 < s < 2$ and sets $s = 1$ to signify the perfect checkerboard. The square-to-square center distance, the period a, is kept as a fixed constant within a checkerboard set. Scaling changes are then made to the edge lengths of the squares, labeled as l_m and l_h for the metal and vacuum hole squares, respectively. In the perfect checkerboard, these edge lengths are equal, $l_m = l_h$. For the island series of structures, the metallic islands have a length set by $l_m = \frac{sa}{2}$ controlled by the scaling factor that is bound by $0 < s < 1$. In the other series, hole structures, the scaling factor is instead bound by $1 < s < 2$ where the edge length of the light, dielectric holes within a continuous dark, metal region is set by $l_h = a(1 - \frac{s}{2})$. Regardless of being in the island or hole structure series, the periodicity is always $a = l_m + l_h$ and the scaling parameter can be written as $s = \frac{2l_m}{a} = 2(1 - \frac{l_h}{a})$. With the definition of the scaling parameter s, the two sets of complementary structures can now undergo a parametric study to explore how the geometric plasmonic effects change when diverging from the perfect

checkerboard.

2.1.2 Bowtie Checkerboard Series

A simple modification to the standard checkerboard was to introduce a scaling parameter that adjusts the sizes of the squares when they are fixed about their respective centers. By changing how you view the unit cell, there is another adjustment to the scaling of the checkerboard squares that yields a different set of structures. Instead of the edge lengths scaled about fixed centers, what if they were scaled about fixed corners? This would manifest as two squares of like contrast, both dark or both light, being permanently asymptotically touching at a corner. The square edge lengths would shrink or grow via the opposite corner and the pattern would be made up of two squares making a bowtie or butterfly shape. Thus, this particular structure series governed by this scaling is dubbed the bowtie checkerboard where Figure 2.2 shows the planar geometry. The scaling parameter s and all the geometrical definitions from the previous section on the standard checkerboard continue to hold the same meaning as the bowtie checkerboard. But by fixing the corners now, the resulting island ($s < 1$) and hole ($s > 1$) series have paired up islands or holes. The perfect checkerboard, Figure 2.2 middle panel, is still the dividing line between the topologically distinct geometric series and is really the only commonality with the standard checkerboard series. Whether on the island or hole side of the division, Figure 2.2 left and right panel respectively, there will always be doubled up squares that nearly touch at their corners. It is this singularity that stands as the biggest difference from the standard checkerboard. Each structure, independent of the value of s, still holds that strong singularity of corner touching. In the standard checkerboard, this feature is only present in the perfect situation at $s = 1$. Plasmonically, this distinction would be expected to manifest differently in the

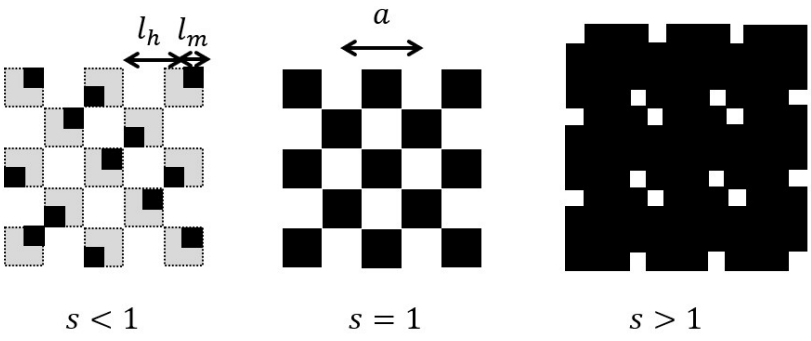

Figure 2.2: -
An example for each phase of the percolation bowtie checkerboard structures with center to center distance a and metal and hole edge lengths l_m and l_h respectively. Contrasting to the standard checkerboard is the always present corner to corner point contact. Left: Underpercolated where the scaling parameter is less than one, creating metallic bowtie islands. Center: The perfect checkerboard existing right at the threshold. Right: Overpercolated where the scaling parameter is greater than one, creating bowtie holes in a metallic sheet.

spectra and will be an interesting point to compare.

2.2 Background

With the geometry defined and interest coming purely from the unique symmetries and scaling of the checkerboard, it's important to think of the possible physical mechanisms at play. Just as metamaterial design looks for equivalent circuit that becomes the analog from a theoretical perspective, the checkerboard system needs a similar conceptualization. Exploring plasmonic responses allows for simplicity since there are signatures in the optical spectra (reflectance, transmittance, and absorbance), which are natural to calculate via computational methods. There needs to be an understanding of how the structure design will appear in these spectra, the physical principles and laws that bridge the two.

2.2.1 Percolation

By just glancing at the structures studied here, connectivity seems like a key concept. Taking the standard checkerboard as an example (but the same goes for the bowtie checkerboard), the perfect checkerboard is the division between two sets of structures. One side stands disconnected. The scaling factor is less than one and each metallic square becomes an isolated island. Trying to measure any conductivity from one side of the square array to the other will yield nothing. On the other side, the scaling factor greater than one makes a square array of holes in a metallic sheet. Metal squares began to overlap and simply are just a single connection now. Measuring the conductivity of this array is now achievable. There is clearly a transition from a state of no long-range connectivity into a state that does. There is an analogous problem to exactly this situation, filtration. Canonically, people think about coffee or ground water. Movement of fluids amongst this porous medium can be constricted if the density of the tiny particles that make up the material is too large. For the coffee (or rainwater) to be able to flow down and drip into a mug (an aquifer), the particle concentration of the grounds (dirt) must be spacious enough. Percolation is this concept, and it extends to many other examples, predominately in mathematics and networks. In the scaling of the checkerboard, the sizes of the squares works exactly as the 'concentration' or 'density'. The flow of electricity is restricted in the island phase while the hole phase is connected. That point in the middle, the barrier of the perfect checkerboard is known as the percolation threshold. Systems involving percolation fall into a universality class, where people study renormalization and fractals in the context of phase transitions and criticality[33]. And that is exactly what is occurring in this system. A sharp phase transition occurs at the perfect checkerboard, separating a conducting and non-conducting phase. Conductivity is also notoriously tied to the dielectric

function, see Appendix A, which of course has significant effect on the optical spectra. This is more than just typical percolation as well. Percolation, think particle concentration, is talking about creating a single path of connection amongst the medium. Once there is one connection from end to end for the system, that system has reached the percolation threshold. In the checkerboard system however, every connection path opens at the same moment. There is not just one path for electrons to flow, there are many. Withing the renormalization group, this type of system shows different scaling than just percolation and is aptly named explosive percolation[34]. The network of squares undergoes instantaneous and simultaneous connection along every node when transitioning through the percolation threshold of the scaling parameter s. Having a connection to percolation and everything that comes with it, the checkerboard systems, under this square edge length scaling, is a playground to interesting mathematics and electromagnetics. One could suspect more beauty in the physics than there is simplicity in the design.

2.2.2 Babinet Principle

Before even a rigorous collection of Maxwell's equations were collected and understood, there were fragmented conjectures that formulated classical EM. One of the most fundamental being the Babinet Principle (BP)[35][36]. Proofs have been given in a couple different manners since the heavy mathematical machinery has evolved and is given in any standard EM textbook[1]. At its core, the BP is quite general and intuitive. One of the standard forms gives a formula for understanding the transmittance in complementary planar structures[1]. It is assumed that these structures are defined by highly reflective films that need to be considered thin. The structures can have any arbitrary planar geometry for the holes/openings, in terms of shape, size, and number. Complementary

structures are the inverse, or the negative, of one structure. Wherever an opening exists, it is swapped with the screen material, while wherever the screen material exists, it is swapped by an opening. An example of structures that are complementary is shown in Figure 2.1, as well as the self-complementary standard checkerboard. With the visualization of a pair of complementary structures, it feels very initiative to think about how they are related. Specifically in the context of transmittance, allowing EM radiation of frequency f to pass perpendicularly through the plane, the structure has a total transmittance of $T(f)$ and the complement has $T_c(f)$. Under the above specified conditions and the plane wave polarization rotated by $\pi/2$ for the complement, the relation for the transmittances is

$$T(f) + T_c(f) = 1 \tag{2.1}$$

As mentioned, the BP is rather intuitive, simply stating that the light transmitted through a planar, reflecting structure, is equal to the light blocked from its complement. And vice-versa is true as well. After undergoing theoretical scrutiny, the BP emerged to be generally valid for specifically planar structures made only of perfect electrical conductor (PEC) that is vanishingly thin[1]. Even conditioned further down by this, there still exists doubts in the literature[37]. In the many proofs for the BP, each seem to lack nuance and detail about what zero thickness and a PEC material physically mean. PEC is simply a theoretical material that requires certain conditions be placed on the electric fields surrounding it, mostly to make calculations simpler. One definition for a PEC is to forcibly apply the condition of zero electric field in the tangential component to the surface while near the surface. This is independent of the frequency of the

electric fields and requires the charge carriers to react instantaneously, even if the wave oscillations are fast. As a model material for high conducting metals, PEC is quite accurate in generally small frequency ranges. Negligible loss and retardation of the charge carriers no longer applies at higher frequencies, which is why real metals experience plasmonic effects. Plasmonic effects certainly are what ruin the BP, but the validity has stood up to experiments when well below the plasmon frequencies with metamaterial structures made of good metals at THz[38] and IR[39] frequency bands. The PEC material is inherently non-plasmonic, aside from when specific geometric conditions are constrained upon it. Since the definition prevents surface electric fields that are tangential and no charge wave can form, then any resonances are forcibly caused by pure standing waves of the structures geometry. Recent demonstrations give examples of plasmonic response in certain structures made of non-plasmonic metals[40]. These structures are planar films that are perforated throughout and undergo exposure to EM waves. Even these non-plasmonic metals, which includes PEC, can create plasmonic effects when structured, referred to as 'spoofing'. Similar to standard plasmons, the 'spoof' plasmons are also obeying causality and thus are naturally delayed responses. As was the case before, one would expect this leading to a violation of the BP. Of these perforated metallic film structures, there is a demonstration of a failure in the BP in a checkerboard structure. The checkerboard, when in the perfect state of no scaling parameter ($s = 1$), is an example of a self-complementary structure. For a structure to be its own complement, following the rule of Equation 2.1 leads to the result $T(f) = T_c(f) = \frac{1}{2}$, simple but extraordinary. For all frequencies and every period length, the BP expects a constant transmittance for this structure. Structures like this have been used as broadband radio antennas[41]. As mentioned previously, the perfect checkerboard is mostly just a concept, as the structure is

extremely singular[32]. Experiments have attempted to achieve this remarkable result, though in relatively lower frequencies and larger sizes, but has proven to be a difficult challenge[31]. In this reference, it is described in detail how the self-complementary structure is actually a violation of the BP. Because of the bifurcation into either connected or disconnected, slight imperfections require masterful fabrication of the structure. One method, this reference has remarkable success with, is to add resistive modifications as little contacts on the corner-to-corner touching points for the whole array. The addition of some weak coupling, via the lossy contacts, is exactly what is needed to be pulled away from the percolation threshold. In turn, removing the singular behavior is what restores the expectation of the BP, in sufficiently low frequencies[31]. Measuring the transmittance in these modified checkerboards with weak coupling between squares, the nearly constant transmittance spectra is observed, as expected by the BP. All this to say, the BP has clear failings around the percolation threshold of a singular structure, such as the checkerboard systems.

2.3 Babinet Principle in Checkerboard Series

With all this so far on the table, the checkerboard series, and bowtie series, parameterized by a scaling factor to vary throughout the percolation threshold, seem to be ideal candidates for possible violations of the BP. Even with the conditions of infinitesimally thin PEC, spoofed plasmonic effects can still result in violations from geometric resonances in the structure, which differ in origin for the arrays that are complements. To start, take a few lessons from previous work published in the literature. Analytical and computational analysis will avoid the concept of the perfect checkerboard ($s = 1$). Using the BP in Equation 2.1, begin by taking a frequency derivative (or two) to arrive at

$$\frac{dT(f)}{df} + \frac{dT_c(f)}{df} = \frac{d^2T(f)}{df^2} + \frac{d^2T_c(f)}{df^2} = 0 \tag{2.2}$$

which, on the surface level, limits the extrema of the transmittance spectra for complementary pairs. For example, having a transmittance minimum in a structure at a particular frequency automatically enforces a transmittance maximum that corresponds one to one at that same frequency for the complementary structure. Explore this first through a simple model for each phase of the percolation threshold. In the hole side of the checkerboard structures, the holes can be considered an array of square waveguides that are subject to a cutoff frequency for waves propagating given by (derived in Appendix A)

$$f_c = \frac{c}{2}\sqrt{(\frac{n}{x})^2 + (\frac{m}{y})^2} \tag{2.3}$$

where c is the speed of light, x and y are the rectangular dimensions of the waveguide, and n and m are integers representing the mode numbers $(n, m \geq 0)$. In the square checkerboard hole system, $x = y = l_h$ and the lowest fundamental mode supported by the waveguides is TE_{10} (or TE_{01} since square), this formula simplifies to [1]

$$\lambda_c = \frac{c}{f_c} = 2l_h \tag{2.4}$$

As a consequence, one should expect transmittance to spike at this frequency f_c, which is purely dependent on the size of the hole. Adding the fact that these

'waveguides' are just short holes would lead to corrections to this simple approach, as well as any array effects coming from interactions between waveguides. For now, stick to this simple idea and later include further details. Moving on to the islands side of the threshold, the comparison will lie at what frequency the transmittance will dip and what geometric dependency does it have. According to the BP in Equation 2.2, this should complement the hole mode and line up exactly. The island side of the structures can also be modeled in a simple way, an large multi-core coax[42]. Already the physics on this side is differing because now there are fewer restrictions on the EM modes supported and the TEM mode can propagate. TEM modes do not have a cutoff frequency and are known for broadband transmittance. To get towards the expected transmittance minimum for this structure, according to the BP, consider the array effects occurring in the free space between islands. Pure photonic resonances create transmittance dips because the scattered waves can constructively interfere. These standing waves are scaled by the spacing of the islands. When that spacing is matched to multiples of the incident wavelength, the resonance formula for large island period a is given approximately by

$$\lambda_r = \frac{c}{f_r} \approx a' \tag{2.5}$$

where $a' = \frac{a}{\sqrt{2}}$ is the distance to nearest neighbors. Resulting transmittance dips on this side of the percolation threshold scales with the structure period monotonically. Comparing back with the holes side, which was only dependent with the hole size l_h, there is completely different scaling on independent structural parameters. All this means that there should be no expectation that the transmittance extrema (maximum and minimum) should correspond between

complementary structures. Each side of the percolation threshold would need identical scaling in a situation where the BP is valid. Analytically, this structure poses a wrinkle to the universality of the BP, but now it'll be further investigated in simulation. Modeling the checkerboard series is straightforward, as the geometry is rather simple. To confirm the scaling proposed above for each side of the threshold, numerical simulations can be done for structures made of PEC that has zero thickness and fixed hole (or island) sizes to $1\mu m$. Plotted in Figure 2.3 is a simulated color map, corresponding to the transmittance spectra for these structures across a frequency range while showing the dependence on the unit cell size a. Simulations for this series of figures in this chapter are primarily done implementing the finite integration technique (FIT) on CST Studio Suite[7]. Models for the checkerboards use geometries made of PEC and vacuum form a periodic array by boundary conditions that enforce a TEM mode wave on a single unit cell. Results from the simulations are unaffected by changing to TE or TM modes for the EM excitation, nor by in plane rotation by $\pi/4$. For even further confirmation and cross-checking, there is agreement of results between different solver algorithms in CST, which includes finite element method (FEM) and transmission-line matrix (TLM) method. One further degree of confirmation is achieved using a completely different CEM software by using COMSOL Multiphysics[43], supplying the utmost confidence in the results presented here. Beginning with Figure 2.3(a), the hole geometry is highly non-transmitting except for a series of high frequency resonances, featuring a strong transmittance maximum near $120THz$. This marks the first cutoff frequency in the waveguide model given previously, which was expected to be independent of a, especially at when large. Having the hole size fixed, the expectation is confirmed that hole structure checkerboards scale in this manner. With that being said, the exact frequency calculated in the waveguide model

(plotted as the vertical dashed line), is red-shifted nearly 20%. Naturally, there are modifications that need to be accounted for in that simple model, such as the short waveguide length and multiplicity of having an array. In the spoof plasmon theory by Pendry et al.[40], the red-shift is consistent. That work uses structures with subwavelength holes, like this checkerboard, and exhibits EOT (extraordinary optical transmittance) because of plasma-like behavior being spoofed by the array. They take a similar waveguide approach to explain the dielectric function for the plane of the holed, thin film takes on a Drude formula ($\epsilon \sim 1 - \frac{\omega_p^2}{\omega^2}$ from Appendix A). The definition of the spoofed plasmon frequency is $\omega_p = 2\pi f_h$ where f_h is the cutoff frequency given in Equation 2.4. Following from this formalism, they later arrive at a spoofed plasmon dispersion for the holed, thin film involving this geometric plasma frequency. The main branch of this dispersion naturally follows the light line at first in the small wavevector region before asymptotically approaching the cutoff frequency[40]. Since the spoof plasmon governing the transmission through the holes is bound to this dispersion, its frequency will always be strictly smaller (red-shift) when compared to the cutoff frequency, as is the case with the simulation.

On the other side of the perfect checkerboard percolation threshold, the complementary islands structures, simulated and plotted in the same fashion, are shown in Figure 2.3. As naively expected, the structures are highly transmitting with pockets of minima at resonant locations. In complete contrast to the hole structures, the resonant locations have strong, monotonic dependence on the period a. Looking closer at the lowest resonance, the dependency derived back in Equation 2.5 agrees quite well. The black star symbols on the plot designate the frequencies calculated directly from Equation 2.5, where agreement with simulation improves for larger a. To further support this, there is other work in the literature that explores thin PEC arrays of circular discs through a dipole

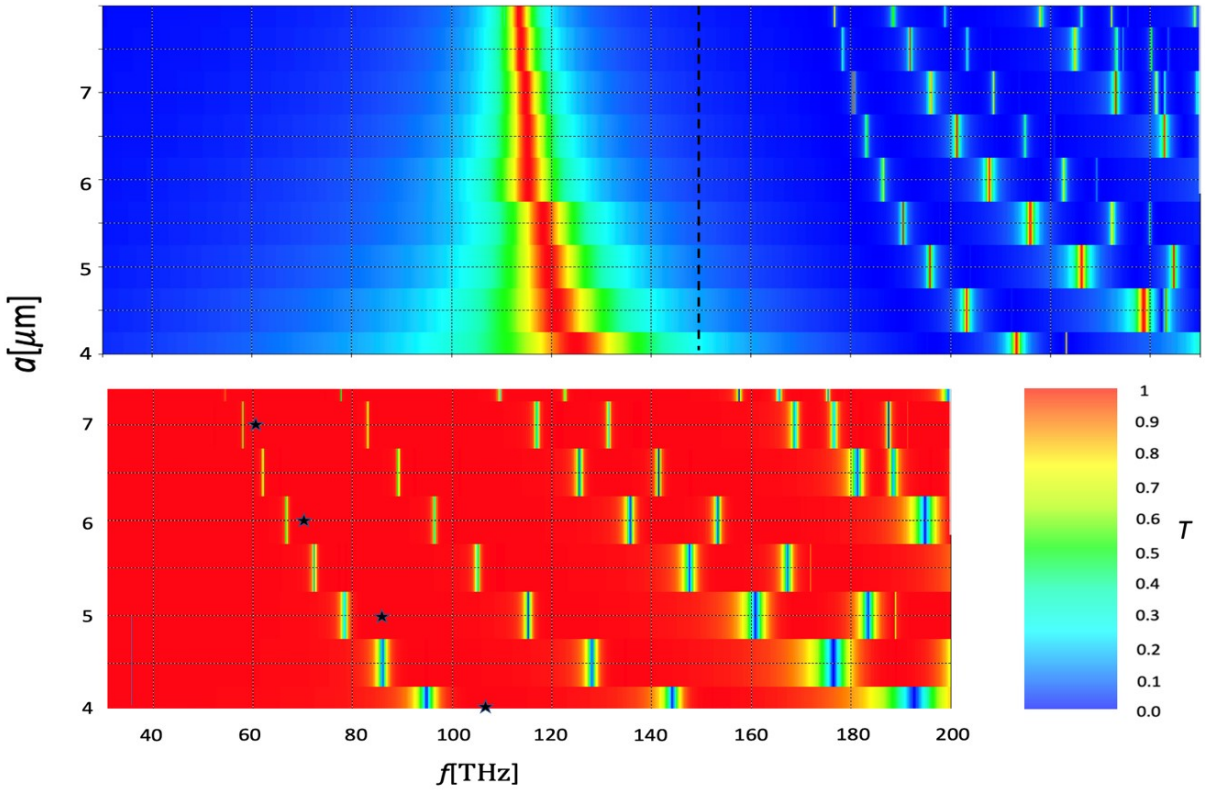

Figure 2.3: -
Top: Transmittance heatmap for a checkerboard with $l_h = 1\mu m$ fixed in the hole phase. The unit cell size is varied over the whole frequency range of a normal incidence EM wave. The black dashed line marks the estimate resonant frequency based on Equation 2.4. Bottom: Identical plot and setup to the above, but for island phase checkerboards with $l_m = 1\mu m$. The stars mark the estimate resonant frequency based on Equation 2.5.

model[1]. In the limit of a small disc radius, each disc is thought of as an individual electric dipole because they dwarf the strength of any induced magnetic dipole moments created from circumferential surface currents. Naturally, the structures are highly transmitting, they also observed a series of near-zero transmittance minima corresponding to the expected model frequencies given by Equation 2.5. Another conclusion from that study was observing no dependency on the radius of the discs. Similarities between the disc structure

and island checkerboard lead to agreement in the EM response, both simulated and model expressions. All the evidence coming together can be summarized simply by there being two completely different scalings on each side of the percolation threshold in the checkerboard structure. Simulations and independent theories, using spoofed plasmons and dipole models, have all converged on the idea that there are severe violations to the BP when resonant physics is split between complementary structures.

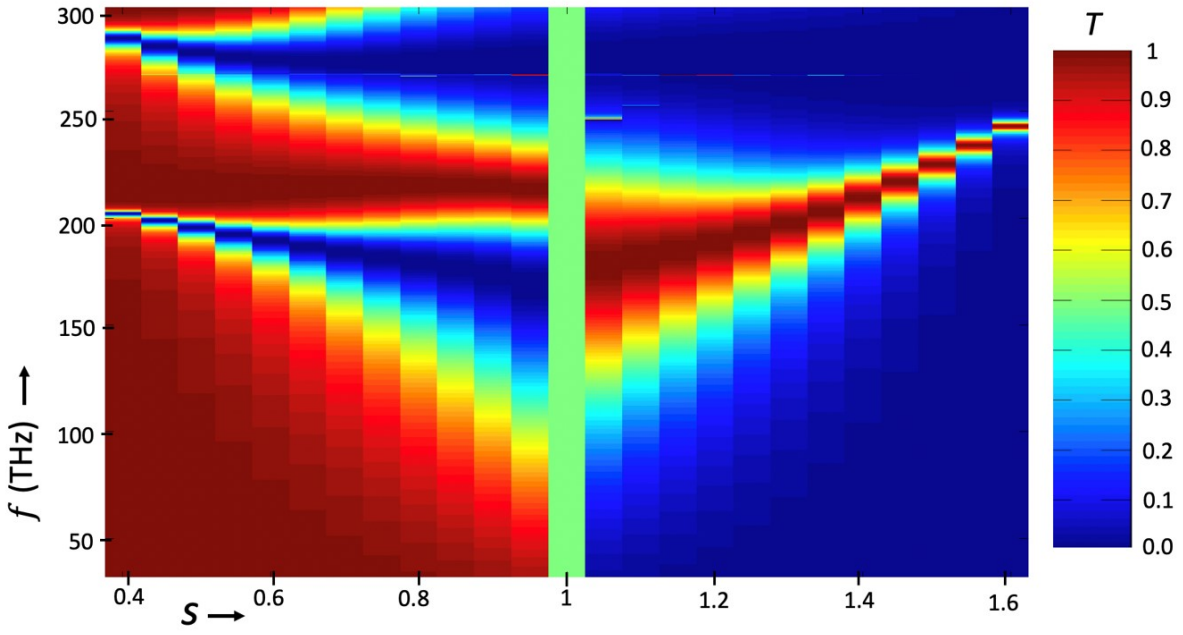

Figure 2.4: -
Color heatmap showing the transmittance spectra for many, infinitely thin PEC checkerboard structures ($a = 2\mu m$) scaled by s through a broad frequency range of normal incident EM waves polarized parallel to the squares edges. The percolation threshold is replaced by the expected BP condition since computation is bifurcated.

For this checkerboard series, the fundamental BP is failing on an enormous level. Having different resonance scaling for the complementary pairs lies as the root cause. A way to picture the distinction across the percolation threshold would be to keep the unit cell fixed but vary the scaling parameter that tunes the

island/hole sizes. The next structures simulated, plotted in Figure 2.4, keep the period fixed to $a = 2\mu m$ and parameterize the checkerboard percentage s. Colors in the plot are identical in representation to the previous figure, mapping out the parameter space of frequency and s by transmittance. Firstly, the data representing the perfect checkerboard at $s = 1$ has not been simulated, because of the aforementioned bifurcation difficulties, and is just assumed to be the trivial self-complementary BP result of $T(f) = \frac{1}{2}$. In the plot, the main resonances take shape and show their diminishing bandwidth as the structures extend, either towards a complete metal sheet or towards empty space. Due to this shape and coloring of the heatmap plot, these are referred to as 'lobster diagrams', resembling the claws of a lobster. By rule of the BP that is defined in Equation 2.1, a lobster diagram would necessarily be symmetric about the central perfect checkerboard stripe. However, the simulation data shows otherwise with sharp asymmetries in certain regions of the figure. Some of the colormap appears to have great satisfaction of the BP, particularly at frequencies below $100THz$, and near BP agreement between 100 and $150THz$. As for the rest of the spectrum, especially above $200THz$, the BP has completely broken down. The most dramatic of differences is in the central resonances as the structures stray further from the perfect checkerboard case. Resonances on the hole side (right side) clearly follow the trend set by Equation 2.4, where decreasing hole size, blue-shifts the peak. Even more egregious than that, the island side (left side) has its next highest order resonance coming into the picture at higher frequencies, of which the hole structure doesn't have. Further simulations showed that this result is unsensitive to changes in the film thickness, given that the thickness is an order of magnitude or more below the wavelength. Isolating a pair of complementary structures from this series and plotting them together will illustrate the collapse of the BP. Figure 2.5 (left panel) takes the

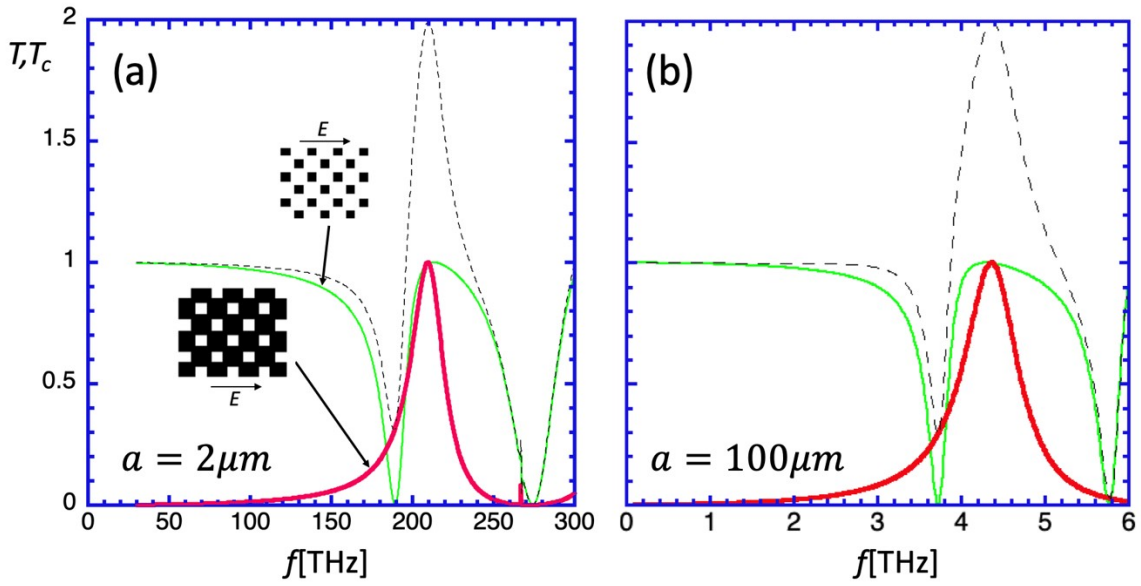

Figure 2.5: -
Simulated transmittance for BP complementary pairs, singled out from Figure 2.4. The green line is for islands while red is for holes and the combination equating to the BP is the black dashed line. Left: Unit cell $a = 2\mu m$. Right: Unit cell $a = 100\mu m$.

structures with a scaling parameter set to $s = 0.6$ (thin green line) and $s = 1.4$ (thick red line), a BP complementary pair, and plots their transmittance over the same frequency range. The black, dashed line is the sum of the two transmittances which by the general requirements of the BP, should obey Equation 2.1. For low frequencies leading up to $100THz$, the BP is mostly satisfied, but then completely fails when reaching the resonant frequency locations. There is a frequency location ($210THz$) where the sum reaches a point where both structures are fully transmitting and a location ($275THz$) where the sum shows the opposite. Figure 2.5, (right panel), shows the same calculation done for checkerboard structures of the same scaling factor but with a fifty fold increase to the geometric dimensions. Naturally, the frequency range has shifted lower by roughly the same factor, but all the same spectral features are still

present. This is of course expected because the structures are made of PEC and the entire physics falls under the influence of EM field dynamics that is size scalable. Checkerboard structures also violate the BP even at low frequencies.

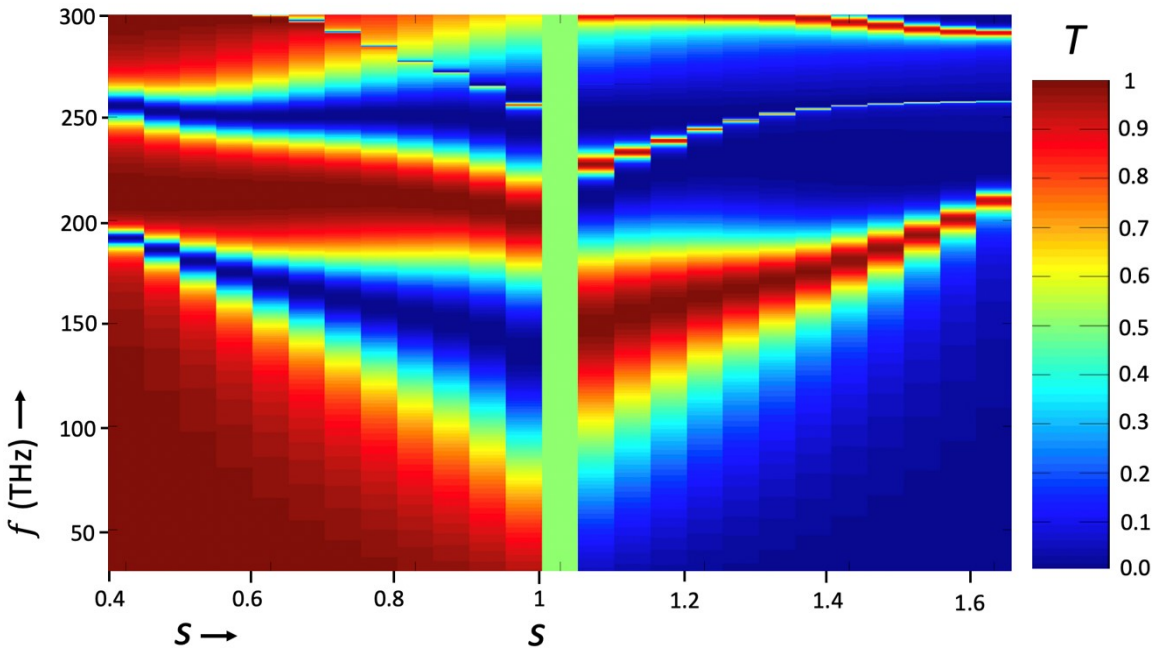

Figure 2.6: -
Color heatmap showing the transmittance spectra for many, gold ($20nm$ thickness) checkerboard structures ($a = 2\mu m$) scaled by s through a broad frequency range of normal incident EM waves polarized parallel to the squares edges. The percolation threshold is replaced by the expected BP condition since computation is bifurcated.

Failure in the BP for the checkerboard structures can be mainly attributed to the different scaling of geometric resonances across the percolation threshold. Hole structures interact intra-hole while on the island side the interaction is inter-island. One could guess if the scaling were to be the same on both sides, the BP could be salvaged. This is the case, with experimental demonstration, for metamaterials with a SSR geometry. As mentioned in the introduction, the SRR is the quintessential metamaterial design, where it is the analog to an LC circuit. The spectral response of electric and magnetic fields is strongly tuned to the

geometric resonance that is controlled by circumferential quantization. Multiples of the structures circumference mark the allowed wavelengths for the propagation of a spoofed plasmon mode along edges[44]. For this example, the BP is approximately satisfied without much of an issue[38]. In the checkerboard structure, however, the percolation threshold sits as a sharp discontinuous boundary between the two distinct scalings and is irreconcilable. There appears to be a topological distinction that can be seen in the spectral resonances. Returning to the lobster diagram in Figure 2.4, the lowest resonance is present on both sides of the threshold, just at different frequencies. Of course, the scale differently but at least there is a one-to-one correspondence. Once reaching the higher frequencies, there is a breaking of that topological complementarity coinciding with the failure of the BP. To rule out the cause of this deriving from the use of infinitely thin PEC, the same lobster diagram can be simulated using a real, plasmonic metal with thickness. A color transmittance plot for the checkerboard structures made of gold ,with dispersion parameters consistent with experimental data[45], is shown in Figure 2.6. By inspection with the lobster diagram for PEC, the two aren't much different, in a general sense. The same scaling, same topology, and the same collapse of the BP. Small differences, like the appearance of a narrow transmittance window for the hold side structures only faintly seen for PEC, add to further failure of the BP, not resolving it. One redeeming trait about the switch to gold is the scaling, of the lowest order resonance on each side of the perfect checkerboard, is closer to symmetric. In total, both geometries have issues with the BP.

Without a doubt, the open-ended question left in the light of these theoretical and simulation results is: Within the proof(s) of the BP, what issues amount to the largely unrestricted criteria for the BP being overreaching? One assumption used in the BP validation was the treatment of having zero thickness PEC. In

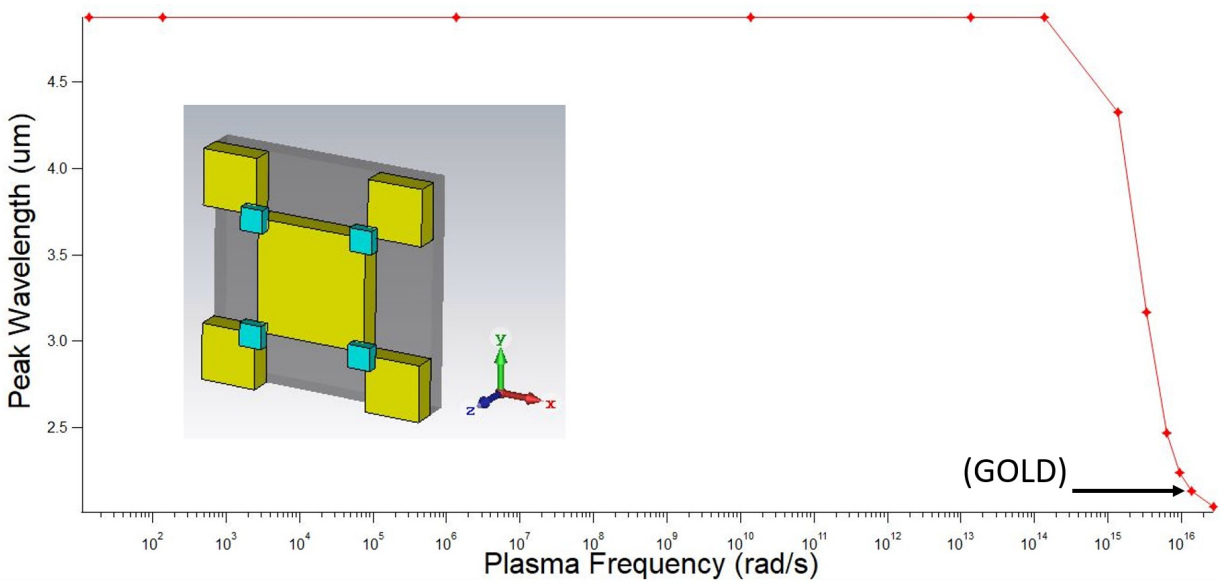

Figure 2.7: -
Simulated transmittance peak wavelengths for a realistic checkerboard structure with $s = 0.95$ and $a = 1\mu m$ where weak coupling between islands is done through a contact material with a parameterized plasma frequency Drude model. Model in the inset and plasma frequency equal to that of measured gold is highlighted.

particular, how to treat the EM wave interaction at the infinitesimally thin edges. On the vanishing cross-sectional edge, enforcement of the PEC condition is glossed over and instead made that the incident wave scattering is also disappearing. In theory, this strict boundary enforcement would surely disallow standing waves and exhibit little to no back reflections. But, this is not the correct enforcement of the consequences for a PEC material. Recall, PEC requires zero penetration by fields and that the tangential component of the electric field goes to zero at the material surface. This can be thought of as identical to the waveguide condition for holes or the coax model for islands. Having the electric field tangentially go to zero along the edges leads directly to the validity of Equations 2.4 and 2.5. FIG dielectric phase map

fig:dielectricphase

Finding inconsistencies with the BP and edge effects, perhaps the bifurcated

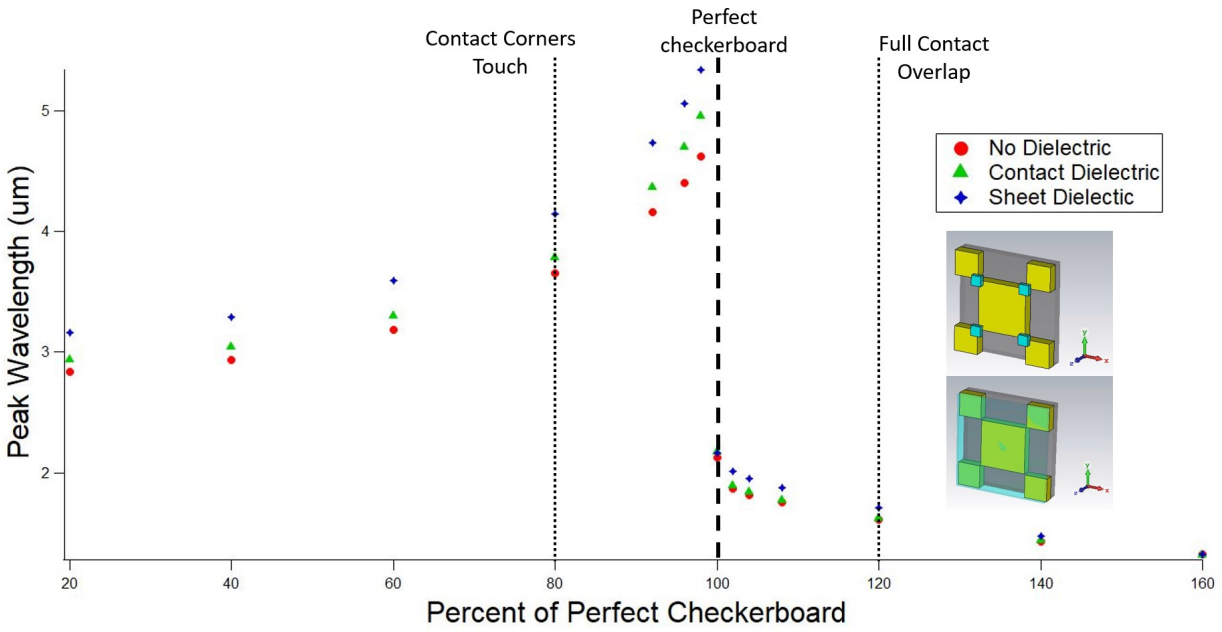

Figure 2.8: -
Simulated is the peak wavelength of the resonance in the transmittacne of checkerboard structures that have either no dielectric material (red circles), corner contact dielectric material (green triangles), or full coverage dielectric material (blue stars). Insets show models with $a = 1\mu m$.

scaling can be literally bridged. As done before, resistive sheets were used to weakly couple the perfect checkerboard into a more stable zone, dealing away with these inconsistencies along the corners[32]. In a similar fashion, computation allows exploration of the tunability of the addition of dielectric contacts. Taking a slightly under-percolated checkerboard ($0.9 < s < 1$) and adding dielectric corner contacts with a parameterized material plasma frequency gives the results in Figure 2.7. Plotting the wavelength location of the resonant peak against this tunable plasma frequency gives an abrupt step function as the dielectric material reaches conductivity levels of metals. The window of bridging between the bifurcated peak values is narrow on a log plot in terms of the plasma frequency but does span a considerable gap in the peak wavelength for this structure. One possible consideration for utilizing this effect

would be in any sort of sensor device configuration where the dramatic change is abrupt and two level. Going back to the BP, the dependency on the scaling parameter is most important, so for a fixed plasma frequency (in the dielectric regime) Figure 2.8 marks the explosive percolation transition. Using different markers of the peak wavelength for three different structures, no contacts, corner contacts, and full sheet contact, shows no major resolution to lining up the two sides of the BP. The overall trend remains constant and so does the difference in scaling across the phases. A study of interest now, would be to adjust the material plasma frequency to higher, but intermediary values where possibility of unification could be seen. Another route taken was to explore how dispersion within the dielectric material changed the transmittance response. For example, the inclusion of a resonant material, both on the peak frequency and away from it. Displayed in Figure 2.9 is a multi-panel evolution through the percolation threshold of an island checkerboard structure connected by resonant dielectric contacts (model in panel (c)). Firstly, the Lorentzian model for the dielectric function of the contact material is shown in the (b) panel. There are two different structures tested, one where the dielectric function is resonant at the same frequency/wavelength location as the transmittance and one which is off resonance from that (at wavelengths of $4.6\mu m$ and $2.3\mu m$ respectively). The figures main panel (a) is the transmittance spectra for both structures (red for on and green for off resonance), as the structure is percolated. Initially, for island structures under a scaling parameter of around $s = 0.8$, the spectra are identical, mainly for their lack of major contact with the dielectric material. As the overlap starts to increase with the resonant material, the main transmittance peak splits for the on-resonance setup. The two structures meet back up across the percolation threshold, essentially the same. Seeing the unique effect that the insulating material having a resonant dielectric function has on the checkerboard

spectra is quite interesting. There is a Fano-like split within the peak as the value of epsilon diverges and forces a zero-transmittance condition on the whole film at the resonant wavelength, which has been analogized as two coupled oscillators[46]. A possibility could remain from further study on how dielectric materials change and can manipulate the validity of the BP for complementary structures like the percolated checkerboard.

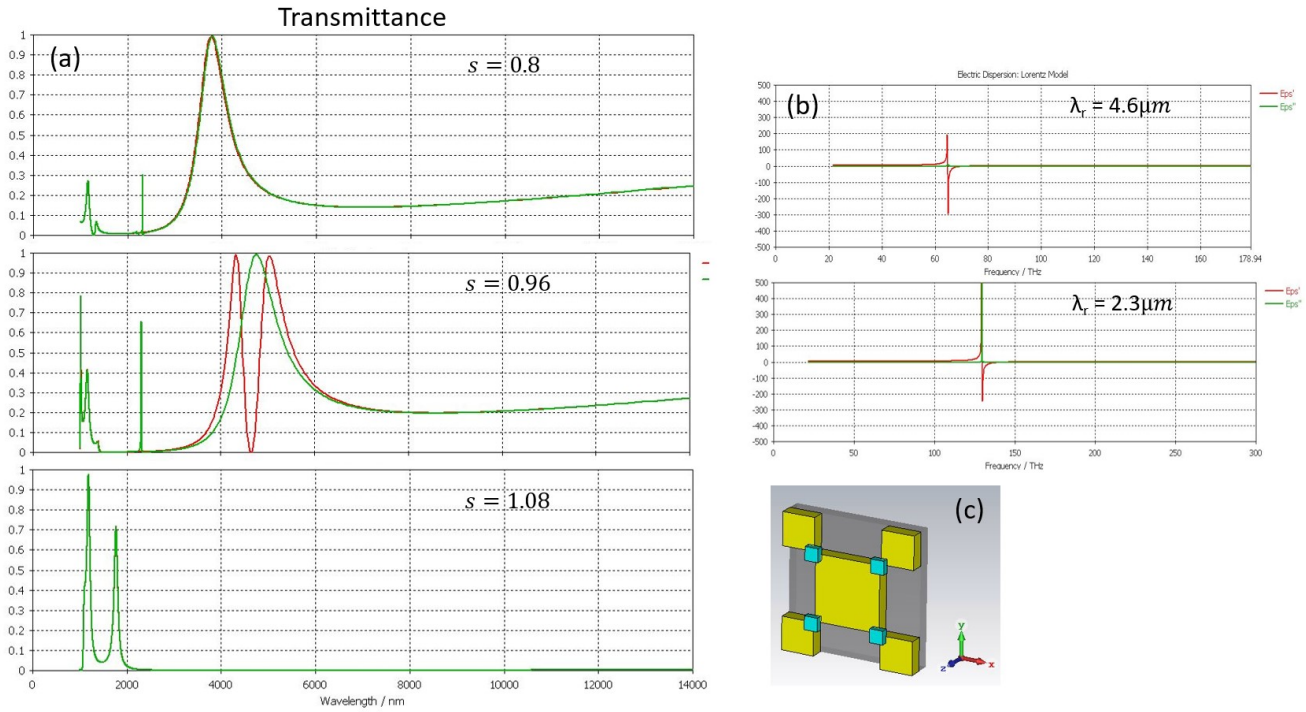

Figure 2.9: -
Simulated in the same fashion as the previous work but the contact dielectric material contains Lorentz model resonances in the dielectric function. (a) Three panels showing the evolution of the transmittance peak for $a = 1\mu m$ in the percolation threshod region. Green curve is for the low wavelength resonance (bottom panel of (b)) while red is for the high wavelength resonance (top panel of (b)). (b) Dielectric function model (real and imaginary parts) for contact material. (c) Model geometry.

Overall, the checkerboard structure is basic on a geometric level, but the understanding of the interaction with electromagnetic waves holds many quirks. Failure in the BP is the most striking of simulation observations, challenging a

longstanding conjecture of EM theory. The percolation threshold and all its non-linearities carry through to the separate scalings across the phase boundary, making it difficult to reconcile the BP around plasmonic resonant frequencies. Still, there remains a lot to understand further about this particular structure.

2.4 Other Complementary Structures

After some geometrical modeling mishaps, the bowtie checkerboard, as previously introduced, contrasts with the regular checkerboard only when being scaled by the scaling parameter. Squares are fixed by a corner instead of the at the center, leading to the unique bowtie shapes for the islands and holes when scaled past the percolation threshold. One interesting point to that island/hole shape is constant singularity feature of corner to corner point contact, as seen in Figure 2.2. Sending this bowtie checkerboard structure through the percolation threshold and simulating the transmittance, in the same fashion as the regular checkerboard, obtains the lobster diagram shown in Figure 2.10(b) that is meant to directly compare back to the Figure 2.4 (re-printed in panel (a)) using the same geometric sizes (unit cell length of $a = 2\mu m$). The further panels in the figure, (c) and (d), take snippets of the bowtie lobster diagram and rescale them to be on the same level as the above plots. The starkest of comparisons is between the basic checkerboard and the low frequency ($30 - 180THz$) of the bowtie, panels (a) and (c). In nearly half of the frequency range, the bowtie seems to reproduce, nearly identically, the same plasmonic resonances nearly identically and the same BP violation as the standard checkerboard. Both sides of the percolation threshold look to scale in the same fashion as the models suggested previously for the hole and island sides of the basic checkerboard. Higher frequency resonances in the bowtie pattern could be other geometric resonances or could be high order standing waves produced in the finite size

calculation domain, further computations are required for verification. However, if indeed caused by the true EM interaction with the structure, there appears to be some extensive quasi-fractality in the spectra. With each zoom in the pattern seems to almost be reproduced in the same way, such that this gives impressions of the self-similarity in a Hofstadter butterfly[47]. The original work plotted the spectra for 2D Bloch electrons relying on periodicity but there have been physical realizations as well. Particularly in EM, the microwave regime was used for producing self-similar transmittance bands for an array of scatterers inserted into a waveguide[48]. A continuation of exploring the similarities to this experiment should be considered, where the bowtie checkerboard is brought into the Bloch framework Hofstadter and others have used to try and get a similar reproduction.

This idea is, however, not unique to just the bowtie structures but can be seen in the basic ones as well. Seeing the similarities in between the two lobster diagrams and the notable near factor of two bandwidth scaling suggests the two structures might not be so different. Take the basic checkerboard for example, and scale the unit cell by two to bring the periodicity to be double that of the bowtie checkerboard. Figure 2.11 gives a direct comparison between the two set up this way in the same simulated lobster diagrams, on the same frequency scale. Finding differences in the spectra is an actual challenge. Only minor differences in spurious resonances and feature sizes can be acknowledged as distinct from one another. Beyond that, it is incredibly remarkable how alike the lobster diagrams are. How can two different, albeit close, geometries show identical transmittance spectra? One thought to be pursued is the idea of circumferential quantization, mentioned in the previous section. Having the doubling of the unit cell length being the only geometrical difference apart from the where the squares are scaled from, lines up the circumference of the islands/holes. In the

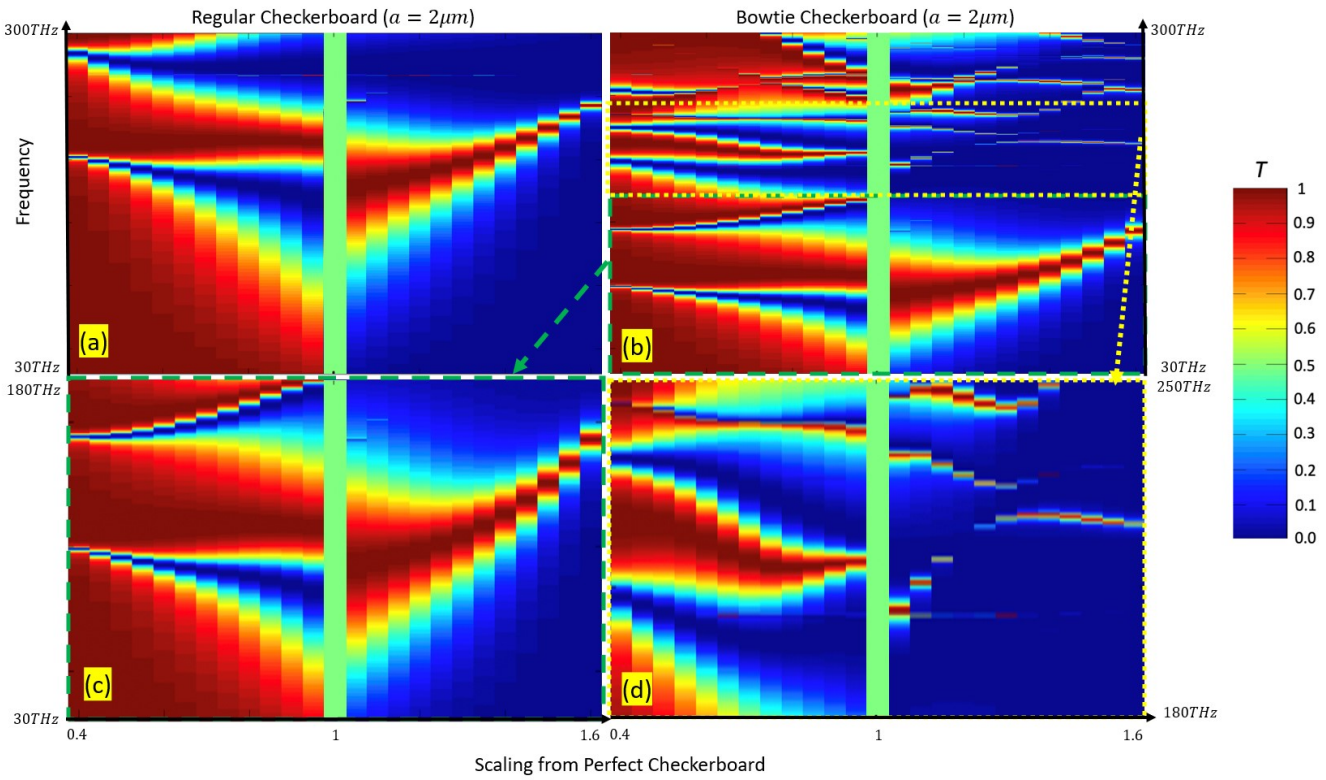

Figure 2.10: -
Simulated transmittance color maps for checkerboard structures done in the same fashion as before. (a) Reproduction of Figure 2.4. (b) Lobster diagram for the bowtie checkerboard of the same period as panel (a) ($a = 2\mu m$). (c) Zoomed cropping taken from panel (b) to be compared with panel (a) highlighted in green. (d) Zoomed cropping taken from panel (b) highlighted in yellow.

basic checkerboard, the island/holes are just one square, and therefore have a circumference of four, square edge lengths. While in the bowtie checkerboard, squares are always paired up and thus the island/hole circumference is eight, square edge lengths, double that of the standard checkerboard. Now there seems to be a bit more insight as to why the two spectra in Figure 2.11 are the same when the basic is double the size of the bowtie. Though the exact one to one correspondence requires further study and verification.

In similar fashion to the regular checkerboard, the idea of introducing weak coupling to the percolation system in attempt to increase stability, can be

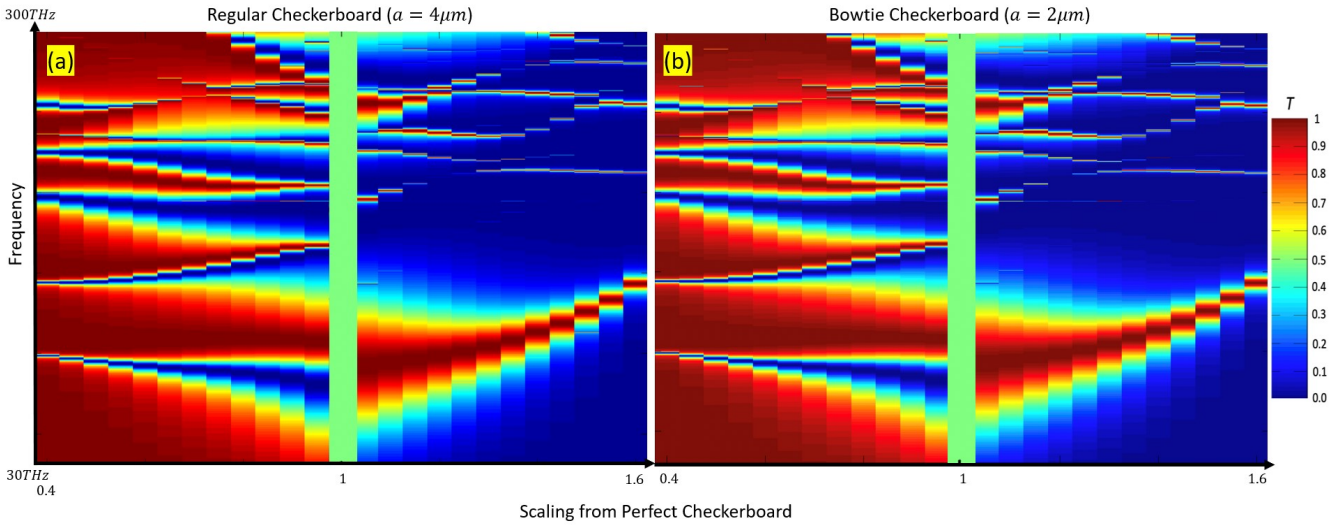

Figure 2.11: -
Simulated transmittance color maps for checkerboard structures done in the same fashion as before. (a) Scaled up to double the unit cell size for the regular checkerboard. (b) Reproduction of the plot in Figure 2.10(b) to be compared with panel (a).

carried over to the bowtie. For the bowtie though, the constant point to point contact of the two squares that make up the bowtie shape is always a source of non-linearities. Therefore, taking any under-percolated, island, structure and attach more dielectric contacts that have a parameterized conductivity. Figure 2.12 is the heatmap for a collection of transmittance spectra for this bowtie structure with $s = 0.8$ shown in the inset. The x-axis now serves as the conductivity for the contacts, to explore the possibility of spectral changes purely due to some connection across the bowtie. For the frequency dependence, these spectra look much different than the PEC film cases before, just as the regular checkerboard did. The coupling brings the structure to the other side of the percolation threshold, showing broad minimal transmittance in the low frequency before hitting a high frequency resonant spike. This feature remains continual over the whole range of simulated contact conductivities, but a second little transmittance bump is formed in the high contact conductivity range. It

seems as if there is an onset of a change in the topology of the spectra as the peak appears without suggestion of being there without the contacts. A lot remains to be further tested and verified among this set of work however, but there are signs of great exploitable properties for sensors of sorts suggested in this one heatmap. Regardless, the inclusion of contacts playing the role of weak couplers does give dramatic transformation to the spectra and is the ultimate region of interesting physics at play with the phase change.

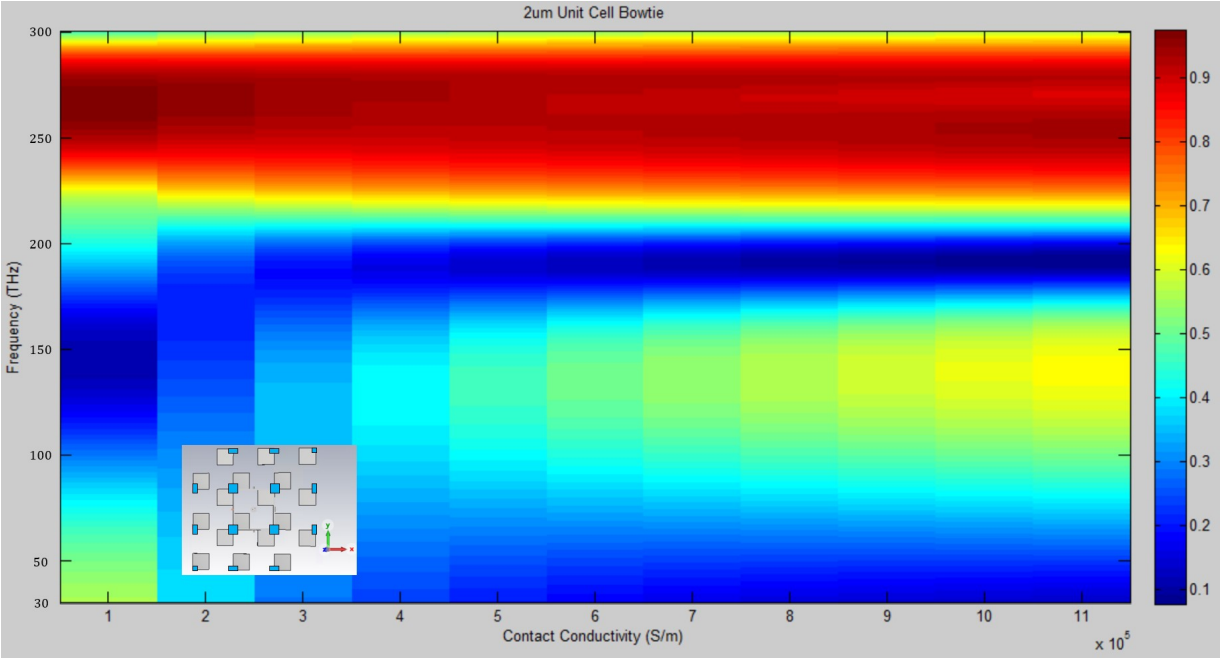

Figure 2.12: -
For a fixed value of $s = 0.8$ and $a = 2\mu m$ bowtie checkerboard with contacts placed on the bowtie corners with parameterized conductivity, the simulated transmittance spectra over the same frequency range and manner. Inset shows the model.

For the final set of investigated percolation structures, of which there are many more, are checkerboards made of circles. Circles can be stacked into a lattice array, in this case either triangular or square lattice, to make up another island/hole pair. In the middle of the percolation threshold ($s = 1$), there is no more self-complementarity and no more Babinet pairs across the threshold. The

circles make up one side while the space between the circles is the other, in shapes known as hypocycloids. Deltoids are the result of three touching circles, in the triangular lattice, while in the square lattice of four touching circles, these are astroids. In theory, this can extend further, increasing the amount of circles, but in the next lobster diagrams shown in Figure 2.13 are just these two. At the bottom of the figure shows the perfect, percolation threshold case for each geometry, with left for deltoids and right for astroids. Each geometry has the same unit cell length of $4\mu m$ but are simulated through the same frequency range, consistent with the checkerboards. The complex shapes involved here make modeling using the waveguide or dipole approaches previously fall a little flat, so these lobster diagrams are meant to serve as a much more observational set. There should be no expectation of symmetry along the vertical middle point, since these structures don't fall into the Babinet pair setup that easily came with square checkerboards. Instead, the spectral behavior about the percolation threshold should stand as the most interesting point. In both diagrams, the middle is mostly a barren zero-transmittance zone across most frequencies, despite tiny and sporadic resonances. Deeper study of these structures goes down the path of exploring more of what occurs close the percolation threshold, optically, as a structure is parameterized through it. What looks to me the main plasmonic resonance, for both shapes, seems to be cut off when too close to the threshold, only to recontinue later on the other side. These structures could also further aid the weak coupling discussion. If contacts were placed here to bridge the percolation threshold, perhaps continuity can be restored the main plasmonic resonance. Without a doubt interesting but straying a little too far from the central body of this work.

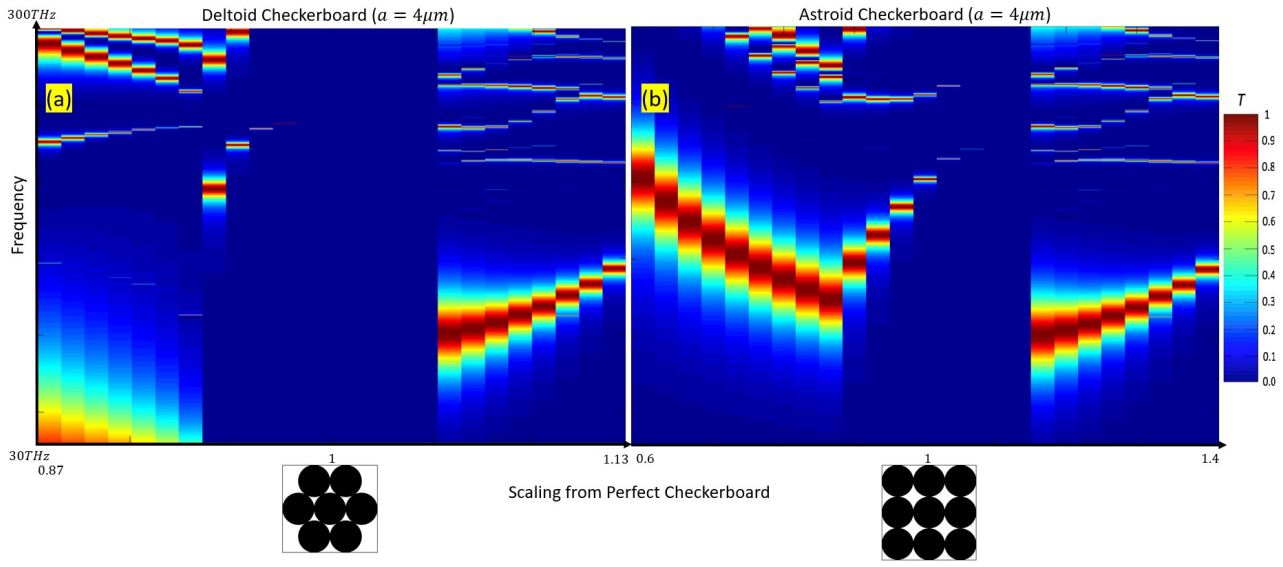

Figure 2.13: -
Simulated transmittance color maps for checkerboard structures done in the same fashion as before. (a) Deltoid structure geometry where the percolation threshold schematic is seen at the bottom. (b) Astroid structure geometry where the percoaltion threshold schematic is seen at the bottom.

2.5 Conclusions

The total summary of this work was meant to explore complementarity and the BP. Checkerboard structures are the Occam's Razor in studying this, for their simplistic geometry and ability to be posed as toy analytical models. Having the presence of the percolation threshold was known to cause some trickiness, especially computationally, but adds a complex dimension to the underlying physics. Collectively, the takeaway is about the failures in the thought to be all encompassing BP. Even when all conditions are met, there are theoretical and computational violations. The geometric resonances developed by standing wave patterns of (spoofed) plasmons follow different scalings across the percolation threshold. There is some irreconcilability, where contacts of various electrical properties don't show signs of bettering the expected symmetry. Even with other geometries and structures, the BP does not always hold and is now the jumping

off point for more complex studies.

CHAPTER III

Extraordinary Optical Transmittance of Bilayer Structures

One standard of detector schemes is to exploit the highly nonlinear in systems. With rapid changes in a functional response of various physical properties, a detector can employ a measurement that notices this change with high sensitivity[49]. These types of nonlinearities are the product of systems undergoing a phase transition, such as the mentioned percolation threshold[50]. It has been shown that undergoing a renormalization group transformation, this threshold represents the critical fixed point, implying large nonlinear response[51]. Previously discussed in Chapter II were checkerboard structures that consisted of distributed conducting squares in some dielectric medium (vacuum). The perfect checkerboard was considered the critical concentration of metallic squares that reaches the percolation threshold where in the structure parameter space there is a phase transition. That junction separates a non-conducting phase of the structure with a conducting one. This radical change in electric conductive response can serve as the backbone to an extremely sensitive detector scheme for several physical properties like temperature, pressure, particle/molecule concentration, optical radiation, etc. In addition, due to the underlying connection between conductivity and the dielectric function

[11], the percolation threshold can drastically alter optical response Ref. [52] as already theoretically explored in Chapter II and Ref. [31] for planar checkerboard structures. The thematic carry over remains the chaotic and nonlinear plasmonic optical response. Such responses have non-trivial consequences to the macro-scale optics. This chapter focuses on one such resulting effect called extraordinary optical transmission (EOT), where plasmonics in periodic metamedia facilitate increased sub-wavelength transmittance of light. Light is assisted through a subwavelength aperture in an opaque surface (generally metallic) by the presence of surface plasmon resonances[53]. Combined with interference effects that come with the territory of apertures, particular wavelengths of incident light, corresponding to resonances in the structural geometry, enable the EOT. There exists analytical explanations of the phenomenon in the cases of simple geometries of arrays of holes[54], but for more complicated features CEM becomes a requirement for preliminary studying. With diffraction as a leading contributor to the EOT phenomenon[55], the computations exist in a naturally tough regime for CEM where structure feature sizes are nearly equivalent with that of the incident radiation. Because of this, there lies a wealth of fundamental electromagnetics and a rather unexplored parameter space of possible systems harboring unique, non-trivial effects. This chapter is broken into two parts that separate different structure geometries and their physics. The first part serves as a continuation of the checkerboard idea, now shifting to bi-layered Babinet structures. The checkerboard geometries are spaced by a layer of dielectric and laterally offset to give the appearance of total coverage of normal incident radiation. Structures based on this scheme for certain dimensions exhibit EOT, via simulations and preliminary experiments. Light, through plasmonic responses of the structure, can transmit wavelengths that seemingly wouldn't naively fit. Tuning of the physical device properties has

direct control over the EOT response and provides an interesting way to explore novel optical filter and sensor applications. The second part of this chapter considers a more practical and fabricable bi-layer system involving nanospheres. Finding the critical point of the percolation threshold and adding weak couplings that restore device stability is a sensible addition when considering applications. Simulation results, matched with experimental data, give strong insight to the physics of the bi-layer Babinet structures that feature a EOT plasmonic response in the IR. All discussed structures show promising potentials for detection schemes based on the effects studied.

The key concept remains as the manipulation of the dielectric function via creating a metamaterial with an effective medium that is geometrically tunable. Exploring with CEM techniques gives a study of non-trivial optical effects, such as EOT, and the underlying plasmonic mechanisms at work in 'difficult to fabricate' or novel systems. This chapter is fundamental to this dissertation as a whole and does provide a significant progression towards future work in the field. Let's discover further the plasmonics on these systems and how beneficial the resulting optical phenomena are in applications.

3.1 Multi-Layered Checkerboard Structures

Taking the lessons and results of the underlying Babinet physics explored with the checkerboard structures in Chapter II, a higher level of abstraction on the geometry can deepen the understanding of the EM mechanisms that allow for sharp, narrow band transmission of light. One point of the checkerboard structures was the extraordinary geometric resonances that harbor plasmons (or spoofed plasmons) that can continue the forward propagation of light waves with a wavelength larger than the orifice of the structure. These excitations capture photons that naively are 'too big' to squeeze through a hole of the checkerboard

and reemit them on the other side, in a simplistic picture. Edges play a critical role in this phenomenon as the surfaces for propagation of the plasmon excitations. Before, the concept was about the Babinet physics of complementary pairs across a percolation threshold on the structures, but the abstraction taken in this chapter aims to instead see these Babinet complements work together in the same structure. By having two complementary structures stacked as layers with one another provides an unique opportunity to understand the combined Babinet behavior of complementary structures, with no better choice to start with than the ultimate self-complementary structure, the checkerboard.

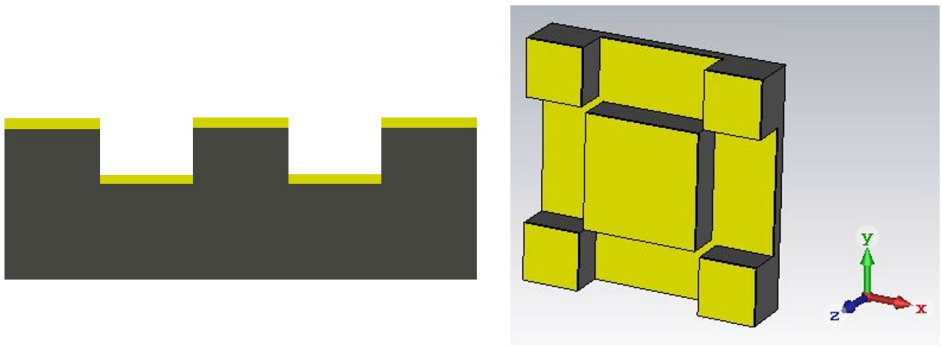

Figure 3.1: -
Two checkerboard complementary arrays have been stacked on top of one another with a spacing buffer of a dielectric material and then offset such that from a top down perspective gives total metallic coverage. Left: Side on view of how a fabricated device would look. Right: CST model of a unit cell for a bi-layered checkerboard with the top at 90% and bottom at 110% of a perfect checkerboard.

Geometrical features between the checkerboards in Chapter II will carry over to the structures in this section, including the definition of the checkerboards' perfect percentage that works as an order parameter for percolation. For this section, two separate checkerboard arrays will stack and then offset from each other to produce the effect of having total metallic coverage when viewed top down at normal incidence, shown in Figure 3.1. Each individual array is designed

to be the complement to its counterpart in the structure with Figure 3.1 showing the top layer at 90% and bottom layer at 110% of the perfect checkerboard. The first layer lies on top of a substrate and built into the holes of that structure are pillars of a dielectric material for which the second layer is built upon. The easy parameters that can be tunned in this situation are the thickness (separation of each layer) and the deviation from a perfect checkerboard for each array.

Both layers are under control of the Babinet physics of an individual checkerboard, so one expects interesting EOT effects, despite there being full metal coverage at normal incidence. One starts by examining these structures with simple metamaterial arguments. The simplest model of Babinet complementary pair layers can be cartoonishly sketched with dipoles representing the holes and islands of each array, as before in Figure 3.2. Incident light with an in-plane electric field component is assumed to have a wavelength that is long in comparison to the structure's geometrical features, effective media approximation. By induction, these fields create an electron gas whose displacement is confined by the metallic structures, seen as surface charge buildup of competing polarizations per layer. Each island and corresponding hole then are each represented as a dipole in this picture and are illustrated in Figure 3.2 as darker rectangles at a particular phase of material polarization.

Separately, each array layer can be thought of as many antennas all being simultaneously driven by the external fields of the light waves. As antennas do, all the absorbed and induced EM radiation can be re-radiated as new light waves. The top layer, in absence of its counterpart, tends to have a re-radiated wave that would cancel the initial excitation wave moving forward at large distances, in the farfield. Expected transmission would be vanishingly small and contain a high back reflection signal. The addition of the complement layer below undoes the cancelation. The bottom array, being the complement and

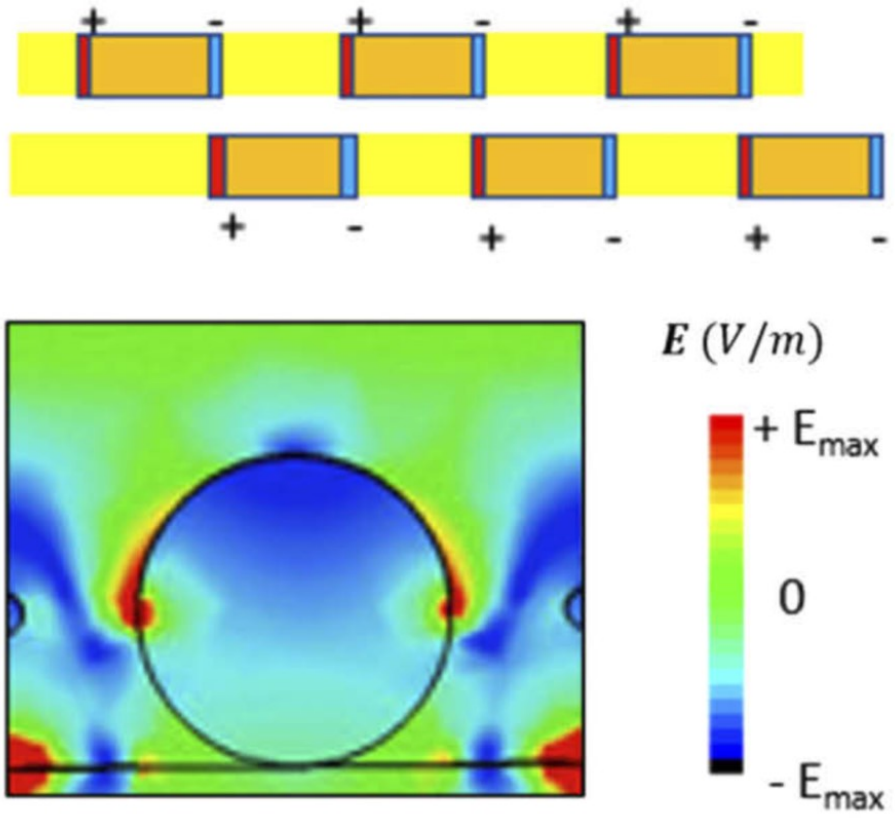

Figure 3.2: -
Top Panel: Simple model illustration of the charge densities in an array of metallic islands (darker rectangles) and its corresponding Babinet complement stacked below. Bottom Panel: Simulated electric field magnitude color map confirming the illustration in the top panel. Image credits [56].

having reversed charge polarization of its dipole representation, cancels out the action of the first antenna layer. Where once the initial wave was blocked in the farfield, now with layered complementary arrays that excitation radiation easily navigates through the complex structure, relatively unperturbed. Simulation affirms this explanation when examining the electric fields calculated by the FIT algorithm in CST, shown in the second panel of Figure 3.2 for a different bi-layer structure that is explored in the next section.

Under the expectation of stimulated transmittance in these structures compared to the naïve expectations of having full metallic coverage, simulations provide the ability to explore with minor consumption of the resources it would take for

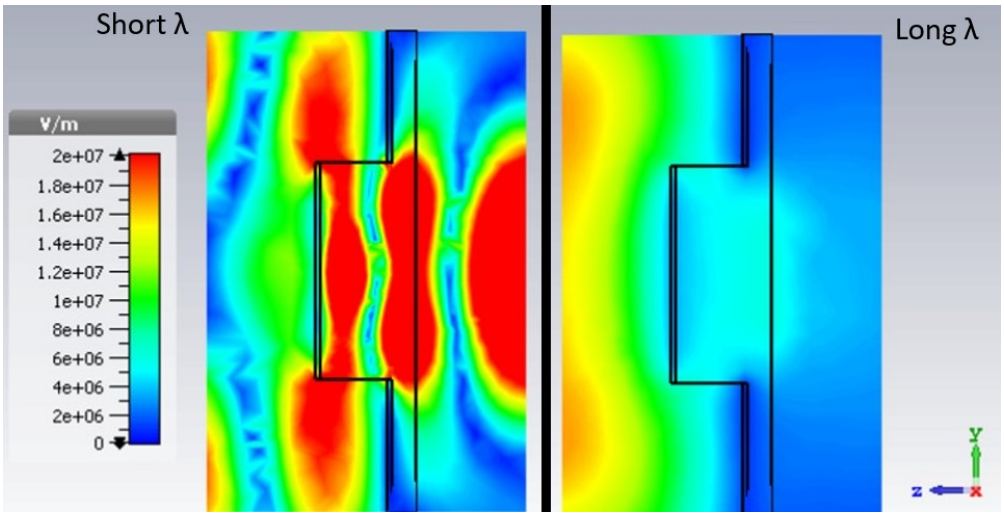

Figure 3.3: -
Using time domain simulations to have a transient understanding of the transmittance for normal incidence TEM light waves. Both panels are of the electric field magnitude in a side-on view cross-section and share the same geometrical feature sizes and color scaling. Left: The wavelength of the excitation is short, falling into the range of the fundamental resonance in the transmittace spectra. Right: The wavelength of the excitation is long, located deeper into the IR regime where the transmittance is near-zero.

fabrication. There are swaths of parameters in this system that can be tuned as a control, but first return to the simple idea of Chapter II about the perfect checkerboard percentage and percolation threshold. The constant for this structure is ensuring total metallic coverage from a perspective of normal incidence, that is to say the two layers of checkerboard are required to have percentages of a perfect checkerboard that sum to 200%. If the checkerboard percentages of each individual array are denoted by s_{top} and s_{bot} then the relationship is fixed at $200\% = s_{top} + s_{bot}$. With the knowledge given so far about percolation thresholds generally, applying that to this situation would simply suggest that at the point of self-complementarity ($s_{top} = s_{bot} = 100\%$) holds the most dramatic optical response. To begin, simulations near that threshold, enough away for stable calculations, can show the potential for discovering in this structure. For the bi-layer checkerboard, the simulated electric fields paint

the picture of how the waves interact with the structure for various frequencies. Exampled in Figure 3.3, short and long wavelengths, in the context of the IR spectrum, are incident normal on the self-complementary bilayer structure. For the short wavelengths (of order of geometric features), strong fields form around the edges of the top layer and are carried to be reemitted on the other side. Lensing and funnel of the light is the contribution of the bottom layer, working with an array of plasmonic dipoles that are completely out of phase with the top. The net sum shows light at these wavelengths be forward scattered and emerge from the structure with strong intensity. The comparison to long wavelengths is stark. Long wavelengths (of order much larger than geometric features), are stopped by the arrays, with only a weak intensity transmitting. The corners and edges are the focal point for transmitting the electric fields, but only for comparable wavelengths to the geometric structural features. The spectral dependence is seen in detail by looking at simulated transmittance for these structures in Figure 3.4. First order resonances appear in the structure series of $2\mu m$ unit cell at a wavelength around $4 - 6\mu m$. While nearly 70% transmission isn't remarkable on the surface level, one must consider that to the normal incidence TEM mode waves in these simulations, the structure appears to be completely reflecting as a plane of gold[45]. Further higher order resonances appear at decreasing wavelengths, naturally. Dependency on the checkerboard percentage of the complementary pairs shows that as the percentage of the top array decreases (deviating more from the perfect checkerboard towards disconnected islands), these resonances occur at shorter and shorter wavelengths. This would suggest that the limitations placed on transmitted light are directly tied to the geometric feature sizes of the top array. A systematic decrease in the transmittance amplitude is expected for lowering percentage of the top array, as one would expect when moving away from the strongly non-linear percolation

threshold[52]. Additionally, as expected for any periodic structure, simulations (not included) show that increasing the unit cell size will redshift the corresponding resonance peaks in the transmittance deeper into the IR, with marginal truncation of the percentage transmitted amplitude.

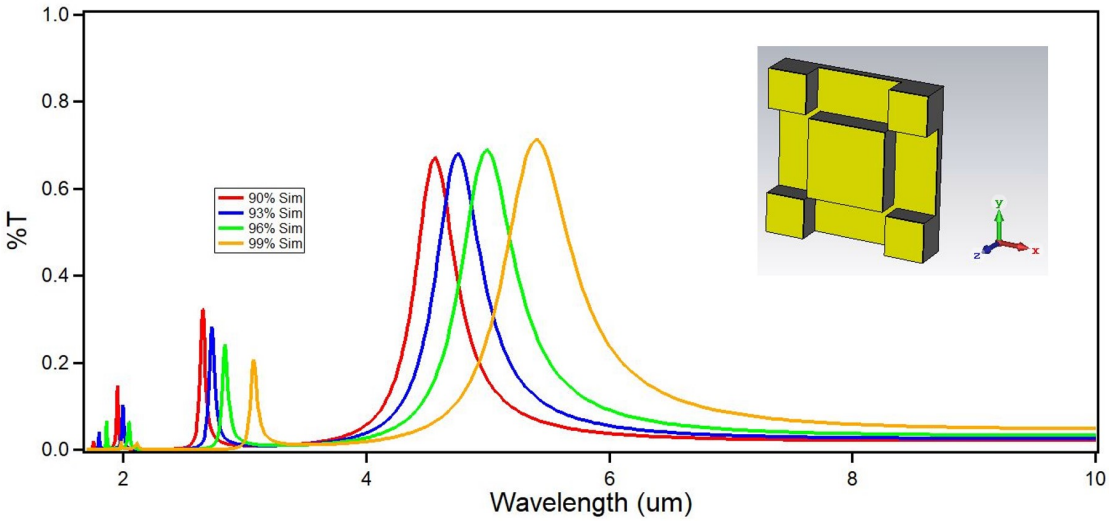

Figure 3.4: -
The inset gives the model geometry example for which the transmittance data was simulated for. Transmittance is plotted against wavelength in the IR spectral range with the four colors representing different checkerboard percentages of the top array. One stark resonant peak for each percentage shows a redshift as the two checkerboard arrays approach being identical, the self-complementary phase. Higher order resonances are observed to the same effect at shorter wavelengths (higher energy).

One possible idea for the explanation of a decently large transmittance response in a near-full coverage metal sheet, is to look towards a well-studied family of band pass filters. It all starts with the idea of a Fabry-Perot interferometer[57], where light is forced to reflect multiple times by two parallel, flat mirrors spaced by a movable distance. The creation of interference fringes from a single beam increases the accuracy and resolution of other multiple beam interferometers. Because of this specialization, many schemes have been introduced over the years for light filter systems based on Fabry-Perot[58]. In order to get to the

single-sourced multiple reflections, multi-layered systems are abundant. Physical and geometric properties of these structures, layer spacing being critical, set the optical path length which ultimately governs the interference band, creating spectral regions of sharp transmittance changes ideal for a filter[59]. Metamaterial designs have been utilized for further improvement of the band pass filter characteristics[60], which are not so dissimilar from the bi-layered checkerboard structure. Looking at the simulated transmittance for these systems throughout this chapter, it is possible an engineer with applications in mind would see strong filter characteristics in the spectra. The results from a parametric simulations of the bi-layer checkerboard with controlled dielectric spacing height are shown in Figure 3.5. Models use a Drude formula with literature values for gold[45] and a dispersion-less dielectric constant to represent a standard fabrication spacer in titanium dioxide. Holding the unit cell size fixed at $1\mu m$ and the scaling parameter of the top (and bottom) layer to 75% (125%), the height of the spacing layer can be tuned, seen in the models inset to Figure 3.5. For these structures, a set of three transmittance spectra have been selected to guide through the sweep of buffer layer height, throughout the NIR window. On the plots are tracking arrows meant as a visual guide to the evolution of two of the peaks. Although seeing the intermediary steps in the simulation truly shows it best, the three stages picked out here give the impression of a strong metamaterial filter. Beginning with the second labeled peak, it starts quite broad at low spacer height with even a shoulder at longer wavelengths. These features nearly disappear as the spacer height increases. As for the first labeled peak, it starts out very unremarkable, existing below 20% transmittance until after the spacer height is doubled twice which is when this peak reaches over 90% transmission levels. More important is the formation of a strict zero-transmittance band around a wavelength of $1500nm$. The first peak is

shifted across that gap and stands as the clear defining line between nearly 'all or nothing' transmittance. Since this gap forms for larger dielectric spacing heights, it is reasonable to suspect that the structure has become sort of band-gapped material. It is not too unfamiliar to see band pass filters made out of metallic meshes in the IR[61]. For example, fabrication of pillared structures with roughly similar geometric sizes to these checkerboards have produced the effects of a periodic array of nanoantennas[62] via a plasmonic resonance localized on the grating that creates a Rayleigh-Wood anomaly. Within such a scenario, an effective diffraction grating steers the diffracted incident light perpendicular to the surface normal of the film[63]. There has been already a lot of work done in this area, both theoretically[64] and experimentally[65], where the plasmonic understanding of the EOT taking place has some explanation. Based on the symmetry between these examples and the bi-layered checkerboard, it seems this structure would fall under this category and would be a worthwhile follow-up to fabricate and test.

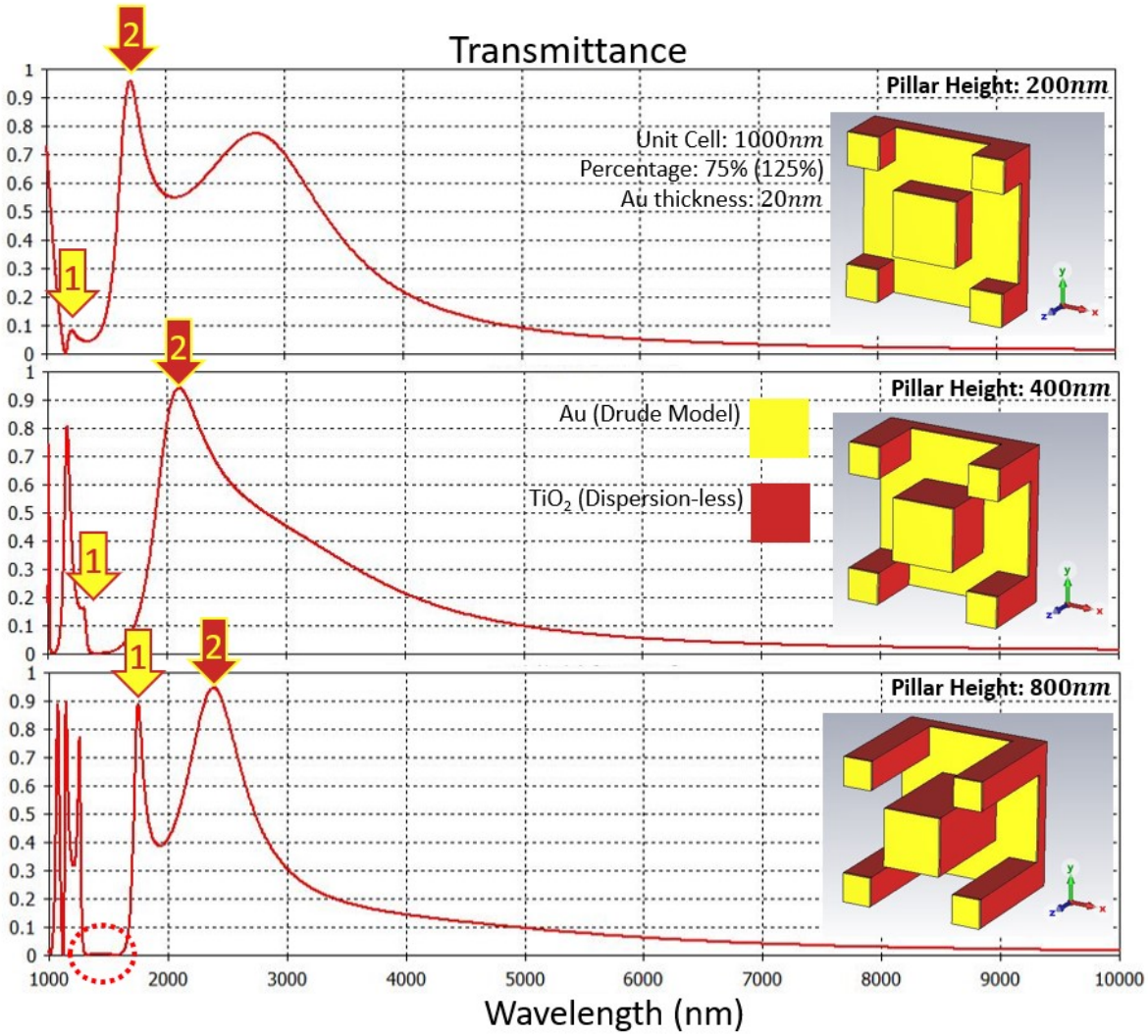

Figure 3.5: -
The evolution of the simulated transmittance spectra verus wavelength of the periodic bi-layer checkerboard structure as the separtion thickness between layers is changed provides a ton of insight. For each spectra, there is an inset showing the structure geometry with the corresponding separation (pillar) height labeled above in bold. The first plot gives global structural parameters that are fixed while the middle plot provides a color legend for the model materials and properties. Arrows in each plot are a visual aid for tracking the evolution of the dominant peaks. A visual aid in the third plot focuses on an area of zero transmittance for further analysis.

An extensive effort was put forward by collaborators to attempt to create a fabrication procedure for cheap and reproducible bi-layered checkerboards coated

in a metal. One workflow was found to be quite successful but measurements from the FTIR (Fourier transform infrared) spectrometer were difficult to capture the transmittance spectra in the same way as simulations. Figure 3.6 displays the results of the measurement to computation comparison. The top panels are dedicated to highlight the SEM (scanning electron microscope) images of the fabricated patterns and simulated 3D models. In total, three patterns were used that kept the period fixed at $2\mu m$ and uniform pillar height (difficult to determine exactly but within a tolerance range) while varying the percentage of the complimentary top and bottom layer checkerboards. Respectively, Pattern 1 (red), Pattern 2 (green), and Pattern 3 (blue) have the top layer set to be at 105%, 85%, and 65% of the perfect checkerboard. Resulting measurements and simulations make up the bottom half of the figure where three simulations spanning the tolerance range of the spacer height are plotted to be compared on the same transmittance scaling as FTIR measurements across the IR wavelength range. Additional baseline measurements are provided since they set the transmittance scaling for the FTIR to what is completely reflecting, thick gold, and what is fully transmitting, germanium substrate. Immediately, the agreement is abyssal for the comparison, which could be due to multiple issues explored for another system later in this chapter (coming from a mismatch in the amount of collected light in the FTIR), but is not void of information. The pattern with the top layer closest to the percolation threshold, but approaching from the island side, shows the most transmittance promise of any of the patterns, in both cases of simulation and experiment. There is something that can be said for the overall shape and behavior to the spectra for each pattern when compared, just some major issues with the magnitude and wavelength shifting. Pattern 1 and 2 in simulations are redshifted by nearly 20% and four times smaller in height, while Pattern 3 is accurate in the absence of peaks in the

whole explored IR range. Many intrigues arise from the checkerboard pattern, and particularly the bi-layered system, so a lot more characterization should be put forward for attempt to fully understand the extraordinary transmittance in a seemingly full coverage, Babinet film with an offset.

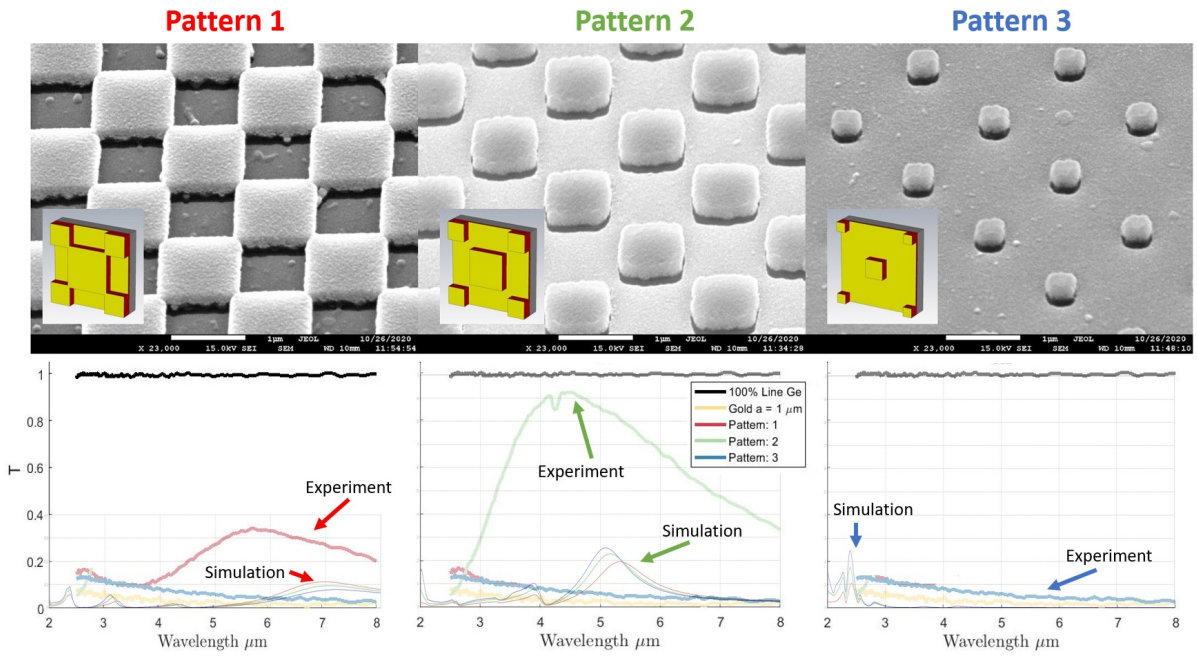

Figure 3.6: -
For three different bi-layer checkerboard structures, shown as a model and SEM image of fabricated patterns, the measured and simualted transmittance spectra are plotted. Simulations have three separate calculations showing some variability in spacer layer. Measurements show a base spectra for a Ge substrate (black) and thick Au (yellow). Both model and fabricated patterns have a $2\mu m$ period with top layer scaling parameters for Pattern 1 (red) $s = 1.05$, Pattern 2 (green) $s = 0.85$, and Pattern 3 (blue) $s = 0.65$.

3.2 Nanosphere Structures

After exploring the structure geometries of the checkerboard and its adjacent configurations, then expanding that to a bi-level system of complementary Babinet pairs, we take one further abstraction. In these multi-layer geometries, the motivation continues to lie at exploiting extreme non-linear responses of

systems lying around percolation threshold of some type. With the inspiration from pre-cursor work[66], we progressively developed a fabrication technique of nanosphere lithography (NSL) to create a bi-layer structure capable of being Babinet complementary pairs. The expansion taken on the fabrication technique allows weak links to be created in the form of 'nano-bridges' between spheres, leaving us with two metallic arrays of either isolated islands or isolated holes. This work parallels that in Chapter II except the complementary pairs are instead stacked. Use of percolation structures in sensor applications is not a trivial demonstration. The extreme nonlinear response is beneficially exploitable for sensitivity purposes but comes at the cost of device instability. This is notorious due to the critical nature of the threshold where small design parameter changes can have significant effects on measurable characteristics. As previously highlighted in the planar self-Babinet checkerboard structure with the bifurcated optical response, the singularities in the geometry make this a near impossible system to realize. One demonstrated solution for this issue is by introducing weak links that gently settle away from the critical nature of the threshold point[32]. Thus, the stability can be restored while still maintaining the desired sensitivity. We show an EOT plasmonic response in the IR, both measured experimentally and simulated via CEM, that has potential geometric tunability and possible sensor applications by exploiting this logic.

Firstly, we begin with the structure geometry. The design does have fabricability in mind, thus it follows a novel form of NSL. As a technique, NSL is quite economical and consistent with the creation of a single layer of spheres in a hexagonal array, typically made of polystyrene. Standard size scales fall under a micron but over the commercialization of the methodology, diameters of the spheres can be precisely controlled. One key component to the fabrication of these periodic arrays, where an example is shown in Figure 3.7, is the utilization

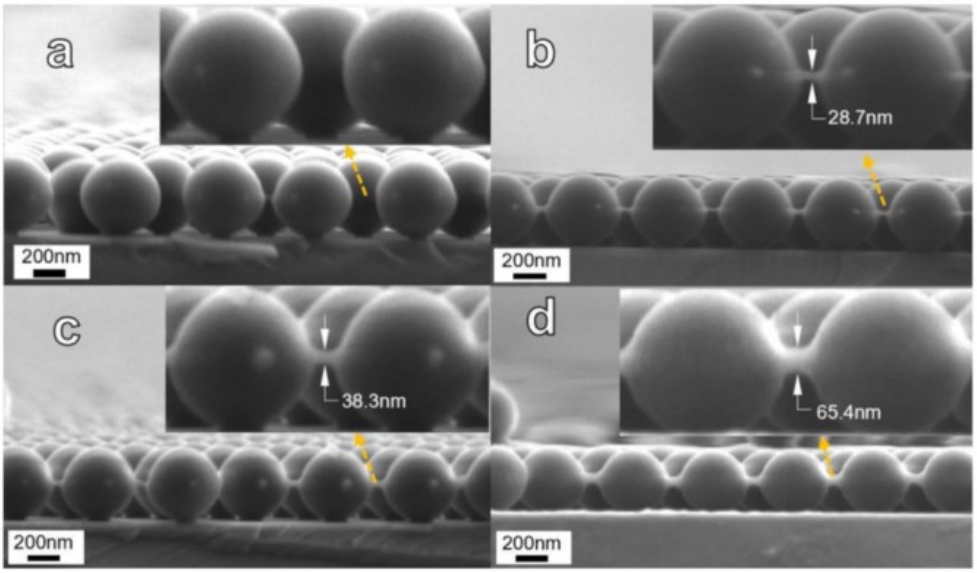

Figure 3.7: -
Four separate cross-sectional SEM images of 500nm PS spheres all etched for the same time duration. Distinction between panels is the amount of styrene concentration to an ethanol solution added to the NSL process where each is (a) 0%, (b) 5%, (c) 7.5%, and (d) 10%. Image credits [66].

of self-assembly. The ordering and organization of the arrays is all done spontaneously and naturally, usually through adsorption. It's simplicity has been well explored and is standard for the production of various spectroscopic templates[67][68], photonic crystals[69], catalysts[70][71], other plasmonic nanostructures[72][73], and several other applications[74][75][76][77]. Each possible application takes a particular modification to the template, with variations on material deposition for example. Taking an array of nanospheres and depositing a metal (via sputtering for example) on top serves as the basis for the construction of the structures discussed in this chapter. Examining Figure 3.8 the top row of panels illustrates what the resulting metallic arrays come out looking like. The spheres have introduced a shadowing effect where depositing the metal collects on the tops of the spheres and falls into the cracks between them. The top array, viewed from the top down, looks like circular, isolated islands. Whereas the bottom array develops as the Babinet complement to the

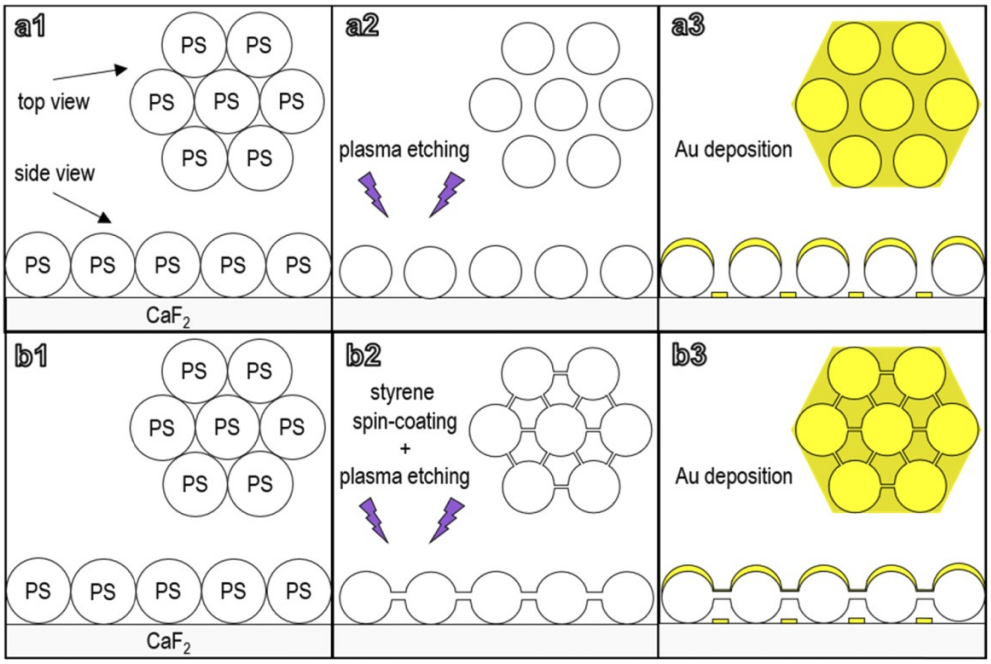

Figure 3.8: -
Top panels (a1-a3) give a top and side view of the simplified fabrication process for disconnected nanosphere arrays while bottom panels (b1-b3) are for the nano-bridged version. Nanosphere template begins the process in both cases (a1, b1) where then plasma etching (a2) shrinks the sphere sizes while fixing their center location. For the formation of nanobridges, there is a pre-treatment of styrene solution (b2). Both structures are metalized in the same way, yeilding the respective structures (a3, b3). Image credits [56].

top array. Notable the top array is disconnected metal while the bottom array has long range connectivity (i.e. islands and holes). In this description of Babinet pairs, the two arrays when placed over one another show total coverage. Having the thought experiment of shining normal incident light appears to naively conclude the light is completely blocked out. This is the central idea behind having Babinet complementary pairs introduced last section and the chapter previously. And similar to the previous discussion of layered checkerboards, these layers are spatially separated by being stacked and having a dielectric spacing. Other than the changing of squares and circles, there is a subtler difference in the structures described in this section. Referring back to

Figure 3.8, in the side view showing the deposition of a metal, such as gold, the top layer on the spheres is curved. These metallic islands are really domed caps on the spheres. All this to say, the geometry is no longer planar, there exists some curvature. The effects of this will be discussed further but for now should be taken as a unique variation to multi-layered structures with non-trivial physics and computational challenges.

Acting as the contrast to the nanosphere structure in this study is the bridged scheme of NSL. This work is in collaboration with a modification to the conventional NSL fabrication technique where a controllable two-step process is introduced[66]. By diluting the spin-coating with a styrene solution and then followed up by oxygen plasma etching the template, the nanospheres create a link with one another. We refer to this process as nano-bridged nanosphere lithography (NB-NSL) as these links are consistent, uniform bridges between each neighboring sphere. The process and differences with traditional NSL is outlined in Ref. [66] where a similar schematic to Figure 3.8 in detail describes the fabrication process. Similar to the standard template, the new bridged version will also have metal deposited as a coating on top. Two arrays are once again formed, the tops of the spheres and the underlying shadowing effect. However, the connectivity of them is opposite from before. The top array now has the nanobridges coated, serving as connections of the dome caps. There is long range connectivity in this case. While on the surface of the substrate, the nanobridges cast a shadow below them, isolating the gaps between the spheres. The leftover structure is a 2D Kagome lattice of quasi-triangular shapes that are electrically disconnected. The roles of the two layers has flipped, in terms of connectivity, with the addition of nanobridges. Without nanobridges the top array stands as the isolated islands with the bottom array as the connected Babinet complement of an array of holes. With nanobridges, the opposite where

the top array becomes connected via nanobridges while the bottom array is the Babinet complement series of islands due to the nanobridge shadows. Each array consequently consists of two plasmon active, periodic, metallic layers that are only submicron distance separated in the vertical direction. The purpose of this contrast is to explore how these structural distinctions manifest into the plasmonic environment. This can be studied via EM simulations, and later verified by experiment on fabricated devices, by looking at the optical consequences of the underlying plasmonic physics.

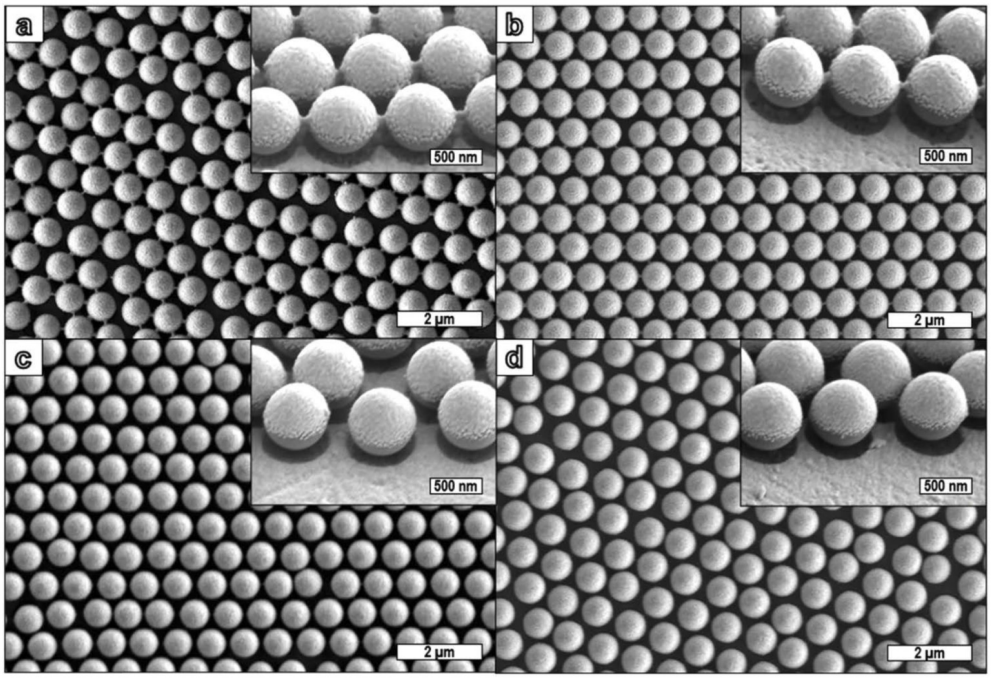

Figure 3.9: -
Each panel gives a top-down view of an SEM image and an inset of a perspective view of an SEM image for (a) a 690nm and (b) 702nm period nano-bridged array and (c) a 690nm and (d) 702nm disconnected array, all with a 784nm pitch. Image credits [56].

As simulations and experiment go hand in hand, the results and discussions are lumped together in this section as a direct way to view the comparison and better understanding the interworking physics at play. To begin, the morphology of both arrays is shown in Figure 3.9 as scanning electron microscope (SEM)

micrographs, with insets showing a magnified version. Sizes and dimensions of the polystyrene (PS) spheres and pitch are determined prior to fabrication based on anticipated plasmonic responses in the NIR. Multiple arrays were fabricated to have sphere diameters varying around the range of $700nm$. They are laid in a closely packed, hexagonal lattice that collaborators conclude to only have a 1.94% error stemming from small divergences away from monodispersity.

Creating structures like these, vertically coupled Babinet complementary plasmonic arrays, have been already demonstrated to accomplish applications with visible light. Examples include plasmonic pixels and surface enhanced Raman spectroscopy[78][79][80]. Taking one step further, there have even been studies on the disconnected PS sphere structures that have been metallized into two vertical arrays. The visible optical response revealed the possibility to modulate plasmonic resonance wavelength location and enhancement of the nanostructures EM fields[81]. Not only is there tunability previously demonstrated for similar structures, but also EOT effects. In slightly adjacent, but simpler structure, EM simulations exemplified a remarkable IR transmittance peak[82]. Theoretical framework has lastly be laid out to give understanding for the EOT at a plasmon resonance of a plasmonic pixel device[83]. Because of the underlying Babinet physics of coupled complementary layers, there was reduction in the spectral width of the resonance and suppression of higher harmonics. The literature provides plenty of documentation around similar structures, but none have taken the extra step of including weak coupling, specifically in the form of nanobridges.

Both structures, disconnected and nano-bridged, are under control of the Babinet physics as discussed in other work. This leads to the expectation of interesting EOT effects, despite being highly metalized structures with nearly full metal coverage at normal incidence. One starts by examining these

structures with simple metamaterial arguments, as done in the previous section for stacked checkerboards. The simplest model of Babinet complementary pair layers can be cartoonishly sketched with dipoles representing the holes and islands of each array, as before in Figure 3.2. But, metamaterial analysis only can loosely ascertain the innerworkings of these more complex structures and expected high transparency. More rigorously, in an effective medium picture there can be analytical expressions for the response function of the structures as a whole [31]. The effective electric susceptibility can be written as a superposition sum of each individual array

$$\chi_{eff}(\omega) = \chi_i(\omega) + \chi_h(\omega) \tag{3.1}$$

where the island and hole array contributions are $\chi_i(\omega) = \Omega^2 \frac{A}{B}$ and $\chi_h(\omega) = -\frac{\omega_d}{\Omega\omega}^2 \frac{B}{A}$ respectively. The parameter Ω is a constant along with $\omega_d = 2c/d$ being only dependent on the thickness of the 'film' (d). The other parameters A and B are products of all the possible harmonic resonances, written out as $A = \prod_n(\omega_{0n}^2 - \omega^2)$ and $B = \prod_n(\omega_{rn}^2 - \omega^2)$. Now, the effective susceptibility can be plotted, showing only the real part if we are to take the metallic losses to be negligible. Figure 3.10 has the top panel graphing all the susceptibilities against frequency ω where the thick solid line (red) is Equation 3.1 built out of the individual susceptibilities $\chi_i(\omega)$ as the thin solid line (black) and $\chi_h(\omega)$ as the dashed line (blue). Using the effective susceptibility in an effective picture, the total transmittance through the pair of structures is given by

$$T_{tot} = \frac{1}{1 + (\frac{\omega}{\omega_d})^2 \chi_{eff}^2(\omega)} \tag{3.2}$$

and is sketched out in the bottom panel of Figure 3.10. A story begins to unravel

now of the origins of EOT within a structure defined in this way. Large peaks, maximizing $T_{tot} \approx 1$, are occurring at near-zero and vanishing values of $|\chi_{eff}(\omega)|$ when the two plots in Figure 3.10 are compared. This is because of the effective medium approximation being taken saying that the combined structure thickness d is much smaller than the light wavelength λ, seen through $(\frac{\omega}{\omega_d})^2 = \pi^2(\frac{d}{\lambda})^2 \ll 1$. One condition for the presence of surface plasmons in an effective medium falls right into this region of the susceptibility, requiring $|\chi_{eff}(\omega)| = 2$. Evidence strongly suggests that these surface plasmon excitations are critical in achieving surprising transmittance maxima, as is the case in conventional EOT. Looking back to the transmittance plot in Figure 3.10, this is a quantity that is standardly simulated, as seen throughout this dissertation. Using FDTD solvers, specifically FIT, a reproduction of these successive maxima and minima of the transmittance spectra can be given for the specific nano-bridged and disconnected nanosphere structures. Displayed in the main plot of Figure 3.11 is the simulated transmittance for a model of both types of structures studied here, where the solid line represents the separated sphere array and dashed line representing the nano-bridged array. Simulations utilized the appropriate boundary conditions that approximate a normal incident wave in the TEM mode. The model consisted of dielectrics for PS spheres and the CaF_2 substrate modeled as dispersionless medium with an index of refraction of $n = 1.6$ and 1.4 respectively. Metal coating used a Lorentz-Drude model for gold based on literature parameters[45]. For each of the two structures, the focus of the simulated transmittance spectra is the maximum peak and the local minimum. At these spectral locations, the simulated electric field profiles on each structure are also shown in the figure with arrows pointing to the particular energy (eV) location. Two panels are exampled for both structures at each point of interest where the upper panel gives a perspective view of the top of the PS spheres and

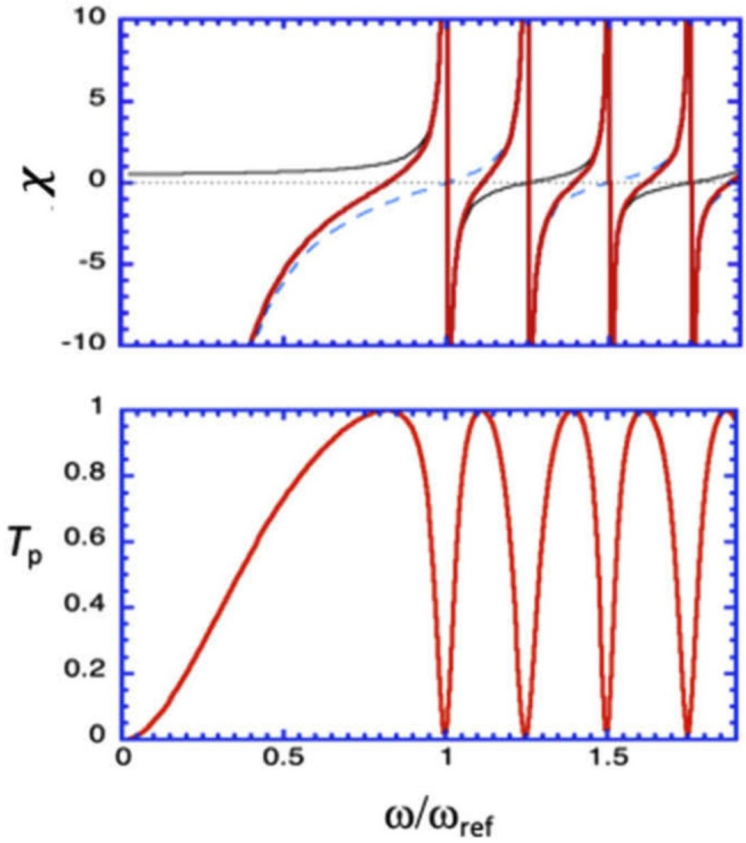

Figure 3.10: -
Top Panel: Plots of the susecptibilities versus frequency ω for the Babinet arrays where there is (thin-solid black line) χ_i, (thin-dashed blue line) χ_h, and (thick-solid red line) χ_{eff}. Bottom Panel: Plotted T_{tot} against frequency ω for complementary Babinet pair arrays. Image credits [56].

the bottom panel gives a top-down view of the base layer structure. Absolute electric field strength is signified by color, following the provided qualitative scaling bar. These simulation figures give identification to the points of the structure that harbor the strong (and weak) fields to give insight to the underlying EM mechanisms. To begin dissecting the field profiles, examine the minima first. Transmittance is at its local lowest value, with light not making it through the structure well. The corresponding field profiles are displayed below the transmittance spectra and show strong field activity on the gold coating of the spheres near where they come closest to each of their neighbors. Intuitively,

this can be thought of as interaction amongst spheres, both in bridged and separated structures. When looking at the Babinet bottom array on the substrate, the absolute electric field is weak or absent. The fields are telling the story here that only the top array of the metal coating on top of the spheres is active when transmittance is at a minimum, fitting exactly into the expectations of the dipole cartoon picture discussed previously. Switching to examining the peaks in transmittance now, which are notable large, the electric field profiles look more active than when at the minima. Particularly, the Babinet bottom arrays have significantly stronger electric fields around the near-touching points of neighboring spheres. Both the top and bottom arrays are active when at the maxima, as suggested by the simulations. This fits nicely into the same narrative theorized in the effective medium framework. To have maximal transmittance in these multi-layer systems, it is a requirement for both layers to be active and provide some field cancelation with one another. Simulations provide insight to the main physics of these systems and completely back the theoretical explanations.

Since the nano-bridged and separated arrays have been, from the start, considering fabrication capabilities, collaborators can perform optical characterization using a Fourier-transform infrared (FTIR) spectrometer to compare to simulation, highlighted in detail in our paper[56]. Plotted in Figure 3.12 (panels (a) and (b)) are the experimental results for each structures transmittance with vacuum wavelength along the x-axis. Simulated comparisons matching the dimensions fabricated are plotted below those (panels (c) and (d)). The last panels of Figure 3.12 replots the measured spectra after correcting for a measurement artifact (panels (e) and (f)). Similarities within the measurements and simulations include main peak locations and peak widths but noticeably they differ in the overall strength of transmittance, independent of structure.

Experimental transmittance is significantly weaker than expectations from simulations. The attribution of this discrepancy goes to scattering. On top of this, in the measured spectra there are also vibrational modes coming from the atmospheric environment (water vaper and CO_2) causing slight fluctuations.

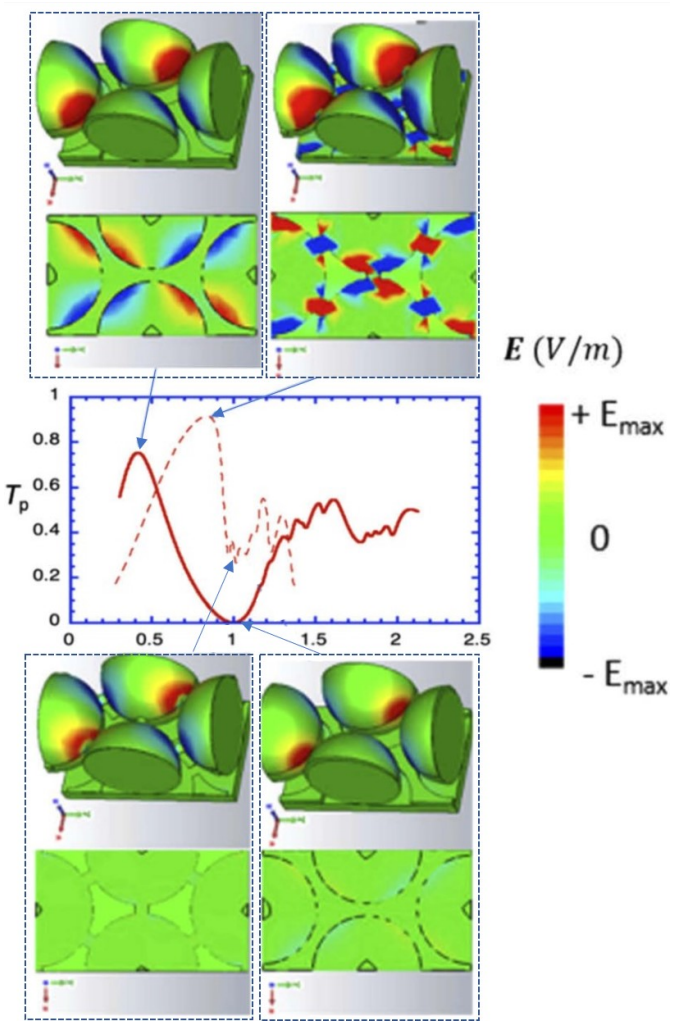

Figure 3.11: -
Plotted in the middle is the transmittance spectra simulated for the (thin-dashed line) nano-bridged and (thick-solid line) separated sphere ($702nm$ diameter) arrays plotted versus energy in eV. Arrows direct the surrounding electric field magnitude plots to the energy (frequency) location that was simulated at. Each model gives a perspective view of the whole structure and a top-down view of the isolated bottom substrate layers. Image credits [56].

Calculating the stray/non-forward scattering alone in simulations and taking

that out is a much more difficult task than a phenomenological model since the models will necessarily require defects and a lack of periodicity that is computationally costly. Mathematically the expression for incorporating scattered light is written as $T_{eff} = T_{exp}\sigma$ where σ is a model for relative scattering cross section. The dominant scattering phenomena would be Rayleigh and Mie types and have already been computational explored [80]. A simple model for the scattering cross section within these mechanisms looks like $\sigma = \frac{A}{1+B\lambda^4}$ with A and B being phenomenological parameters. Just as what occurs for the blue color of the sky, Rayleigh scattering is the dominant effect for large wavelengths due to the large exponent. For large λ or large B the formula for the scattering cross section model is simplified to $\sigma = \frac{A}{B\lambda^4}$ and shows short wavelength components of a transmittance spectra drowning out compared to the longer wavelengths. Exactly as seen in the blue sky. Mie scattering, on the other hand, handles the lower wavelength or smaller B regions[84]. In this limit the cross section approaches equaling the value of A. Scattering of this type happens for larger particles/scatterers with little dependence on λ and leads to generally larger effective transmitted light. Through using this phenomenological model to account for any non-forward scattered light in the experimental setup, the plots shown in the bottom panels (panels (e) and (f)) of Figure 3.12 can be obtained. For the nano-bridged structures, they contain very small scatterers that the separated array does not have, the nanobridges themselves. In this case, Rayleigh scattering will have a strong effect, so the model used is a mixed Rayleigh-Mie limit ($B = 0.001\mu m^{-4}$). The separated structures were set to lie completely in the Mie limit ($B = 0$) for some presence of large scatterers in the spheres. For the values of A, they were calculated by optimization with simulations derived via least square fitting to be fully consistent with scattering theory. Experiment and computation are now much more comparable to see the

levels of which EOT exists in these structures and what role the nanobridges play.

Both structures exemplify an advantageous transmittance peak in the IR deriving from the EOT physics of the presence of surface plasmons. But when comparing nano-bridged to separated structures, the nano-bridged have a much more exploitable feature within the peak, quite large slope. An example application scheme would involve a fixed wavelength (frequency), using $4\mu m$ for example, and there is an easy to measure transmittance value that is readily changed by structural geometric parameters. The fabrication process is additionally consistent and considered inexpensive, allowing detector devices to be developed in an intuitive way. Once again comparing the spectra for the two structures, the effect that the nanobridges contributes is quite drastic. The weak coupling they provide to the top array gives some enhanced sensitivity while stability remains integral. Underlying plasmonic physics is non-trivial in these systems but even with simple explorations of effective medium approaches being paired with CEM, one can arrive at a comprehensive understanding of these complex innerworkings. These methodologies explored here are scalable to other systems and provides a starting point for further understanding and development of unique optical phenomena in novel systems.

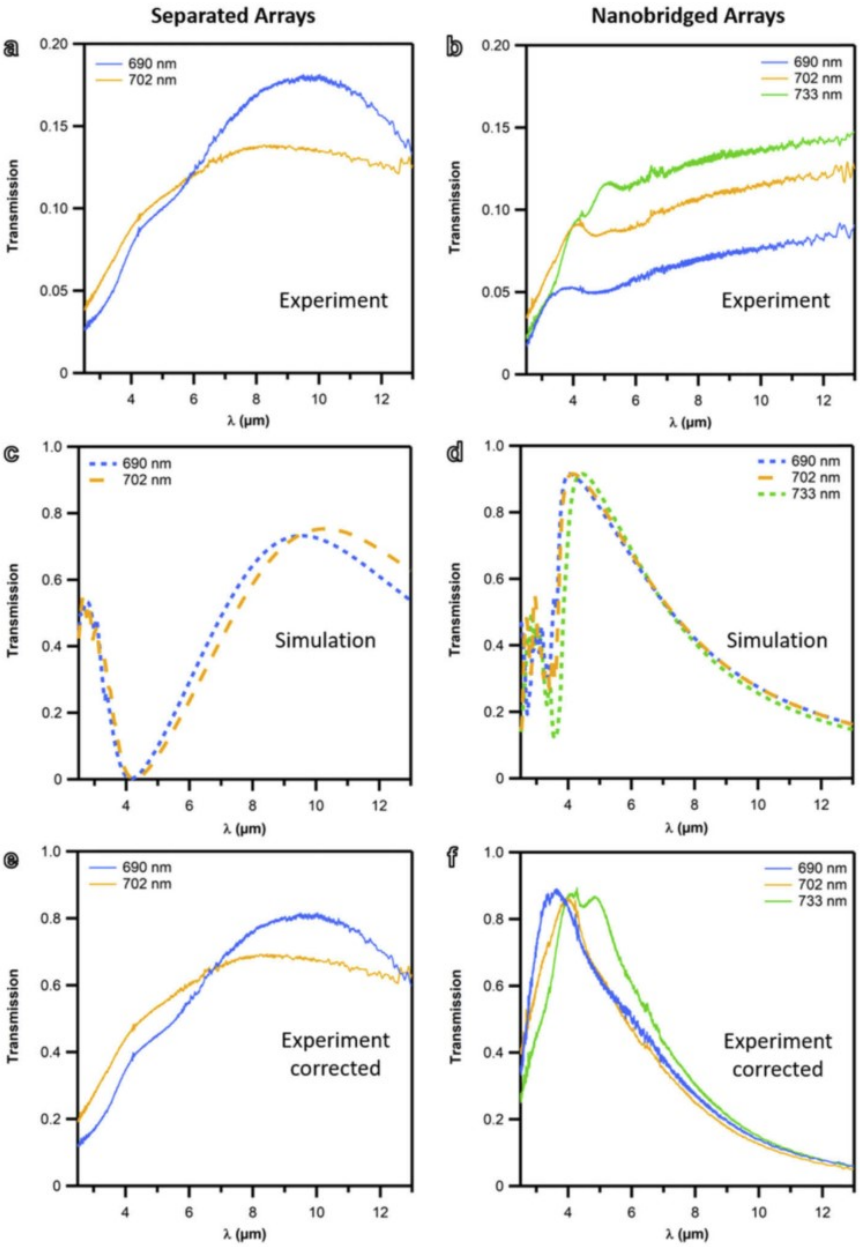

Figure 3.12: -
Spanning some of the IR spectra are the transmittance plots for (panels (a) and (b)) experimental FTIR data, (panels (c) and (d)) FIT simulation results, and (panels (e) and (f)) corresponding experiemntal spectra that are corrected for missing phenomenological scattering all split into (left) separated and (right) nano-bridged arrays each parameterized with sphere diameters. Model parameters used for (e) are: $B = 0$, and $A = 5$ ($702nm$ diameter), $A = 4.5$ ($690nm$ diameter). Model parameters used for (f) are: $B = 0.001\mu m^{-4}$, and $A = 0.0013$ ($733nm$ diameter), $A = 0.0012$ ($702nm$ diameter), $A = 0.002$ ($690nm$ diameter). Image credits [56].

CHAPTER IV

Negative Refractive Index Capabilities of Photonic Crystals

4.1 Background

For the coming chapter, a pattern of the work presented here has emerged. Slowly, the structure geometries have been building up in dimensionality. Checkerboards with infinitely thin PEC are 2D planar sheets but given a thickness when converted to real metals. Elevated further with the addition of another checkerboard layer in the bi-layered structures. That physics was carried to the nanosphere structures, 3D but solely a monolayer. By following the pattern, the next structures are just lattices of nanospheres. While not incorrect, the geometric 'step up' falls into an entirely different class of metamedia, photonic crystals, though they exist in 1D, 2D, and 3D. Take a simple atomic crystal, ordered elements arranged in a periodic pattern across all 3D space, and imagine that scaled up to the nano and even micro level. Albeit quite naïve, but for how light propagates within the crystal, natural and photonic crystals behave the same way. The scale difference only changes the regime of light wavelengths that diffract and scatter within the lattices. On atomic scales, Bragg diffraction is primarily concerned with EM waves in the x-ray spectra. While in photonic

crystals, the spectral region of interest is entirely the engineering purpose behind it. Photonic crystals can be natural themselves. For example, photonic crystals could be thought of as biomimicry, where nature provides a blueprint. Such a demonstration is seen on the wings in some butterflies, refracting optically, and in the UV, with vibrant colors and opalescence[85]. In fact, opal itself is a periodic microstructure of silica (SiO_2) molecules that exhibits the same optical effects. Generally, opal is polycrystalline at best for jewelry purposes, which is why the light refractions are all over place, defining the opalescence attribute. The composition of photonic crystals, like metamaterials, is up to the parameters and applications with various mixes of metal and dielectric. Periodicity is a powerful geometric constraint. A common analogy for the way periodicity in photonic crystals influence EM waves is the behavior of electrons under periodic potentials of semiconductors. This bridges many attributes between the uses of photonic crystals and semiconducting solar cells, a possible way to boost solar cell efficiency[86]. Inside the photonic crystal, the underlying effective dielectric function repeats contrasting high and low dielectric environments, which as a direct effect on the index of refraction of the crystal by $n = \sqrt{\varepsilon}$ (when the permeability is normal). Here interference effects dictate the light propagation, considering the wavelength is around the same size as the lattice periodicity. In the same fashion as semiconductor electrons a particular band structure full of allowed and disallowed states, so too do photonic crystals. EM waves in a photonic crystal are modes that are either allowed or forbidden to propagate along certain directions and for specific frequencies (energies). One common signature in many photonic crystals, just as in semiconductors, is the existence of a band gap. Interesting optical phenomena can arise from more complicated photonic band structures, designed to manipulate light flow.

One such example is achieving a negatively refracting material ($n \leq -1$). A

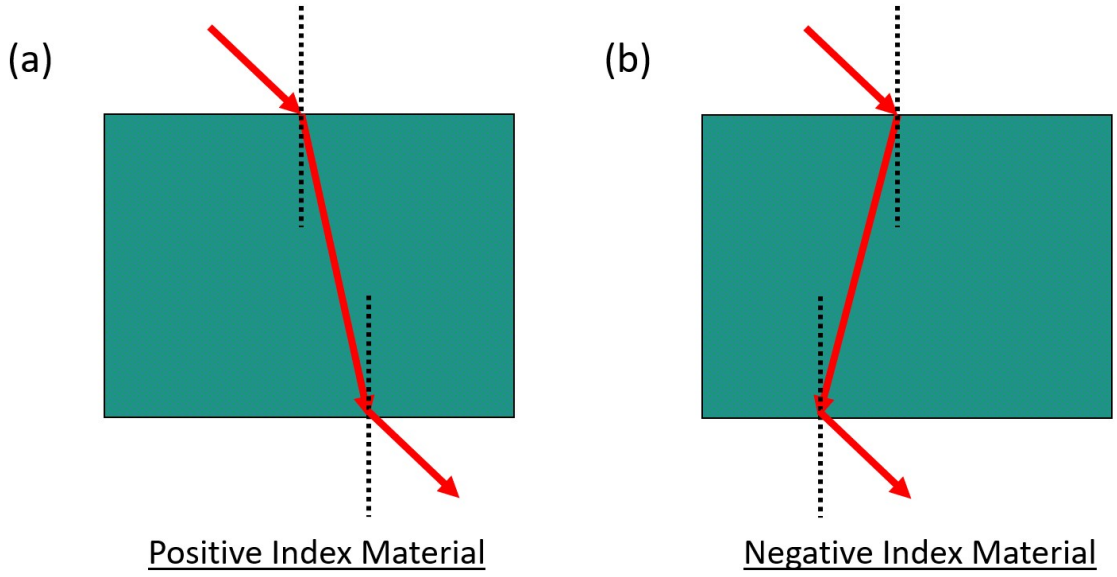

Figure 4.1: -
Snell's law defines the geometric optics of refraction at the interface of two materials. (a) Positive index materials, anything naturally existing, refract light about the surface normal. Light entering a higher index material slows down and adjusts to propafating in a new medium. (b) Negative index materials, engineered metamaterials, refract abnormally along the surface normal, appearing to bend backwards.

material of this type is truly an anomaly to how we view the world. Snell's law is the geometric optics guiding principle for light refraction between two different mediums, as shown in Figure 4.1(a). Enjoyed and taught for its simplicity, $n_1 sin(\theta_1) = n_2 sin(\theta_2)$, Snell's law determines the refraction angle of light going from one medium to another based on the two indices of refraction. A classic visualization is when a straw is placed in a glass of water and viewed from the side, giving the illusion that the straw has been bent slightly at the water's surface. The interesting twist is when one of the indices of a material is negative instead, causing the resulting refraction angle to bend along the surface normal in the opposite way. For the straw example, the bend in the straw at the water's surface would look nearly unphysical, no longer a slight kink but a full bend in

the other direction, just like Figure 4.1(b) suggests. Simple focusing lenses can be created from a flat slab of a negative index material (NIM). Photonic crystals with the ability to produce bandwidths of negative refractive index have been shown[87], with variability in scheme[88]. One of many discoveries by Pendry, utilizes a NIM in a lens that can triumph over the diffraction limit. Any conventional optical system has its best resolution capped by the law of physics. There is a direct proportionality between the wavelength of the imaging light and the smallest observable feature size[58], preventing any clear resolution for microscopes, telescopes, etc. A superlens was Pendry's proposition for capturing these fine details, with the physical basis behind it being negative refraction[23]. Metamaterials, such as the SRR, can also achieve this feat[28][89], but strong efforts in nanofabrication suggest easy scalability in photonic crystals. Neighboring idea polaritonic crystals, which can nearly be used interchangeably with photonic crystals, utilize charge polarization of customizable nanoparticles to produce similar dielectric response[90]. Commonly through any of these systems, is the crystalline structure of the engineered material. The lattice consists of spheres of one material (perhaps even coated) while surrounding them in a matrix of another material, forming a typical crystal structure like FCC (face-centered cubic) for the unit cell. An cubic example in 2D is shown in Figure 4.2 for reference where the size scaling could be on the nano- to micro-level depending on interested frequencies. Contrast amongst the various indices of refraction for the materials is generally welcomed and associated with larger photonic band gaps. Using the FCC lattice, Brillouin zone (BZ) plotted in the second panel of Figure 4.2, gives one of the closest Brillouin zone's to being isotropic. In other words, the truncated octahedron is nearly spherical, giving the advantage that along all possible directions of propagation the EM waves disperse similarly. Given all this information about the crystal, theoretical

studies can be conducted in parallel to fabrication efforts to explore the possibility of a NIM superlens.

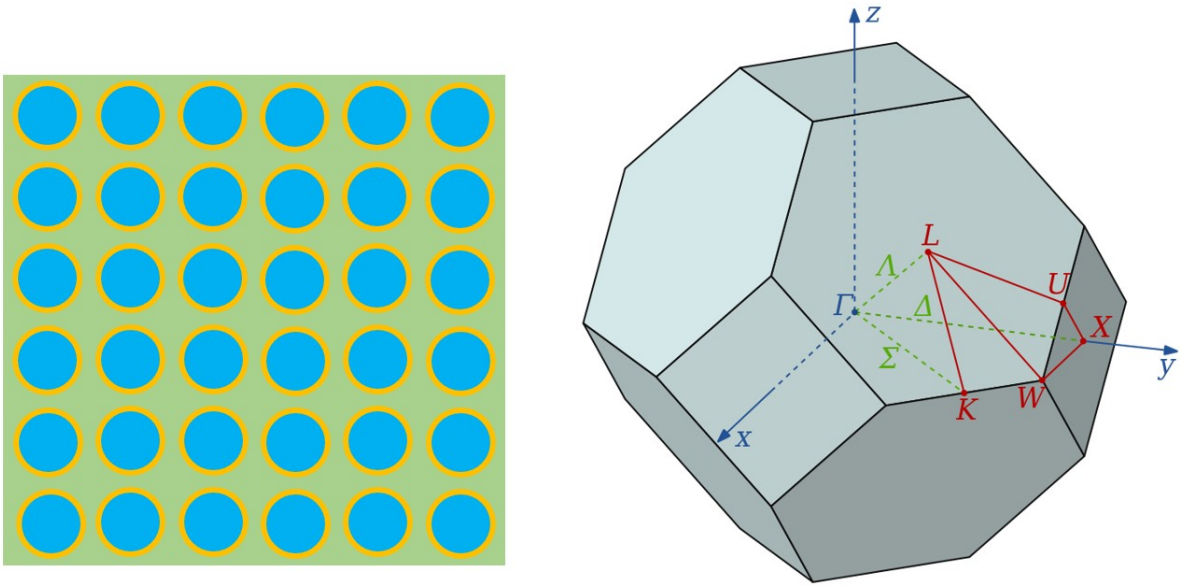

Figure 4.2: -
Spheres consisting of one material, possibly coated, inside a matrix of another material form a 2D cubic lattice of a photonic or polaritonic crystal in the left panel. When scaled up to 3D, tightly stacking spheres in a unit cell is the FCC latice which has the Brillouin zone (BZ) in the right panel. The BZ is a momentum space mapping of the crystal lattice with the high symmetry points denoted by letters (Γ, L, U, X, W, and K). Some propagation paths are denoted in green Greek letters. (BZ) Image credits [91].

4.2 Band Structure Calculations

As mentioned previously, light in photonic crystals has an analogy to the electrons of semiconductors, which is why band structure calculations are critical. In a semiconductor, bands are the allowed energies and momentum of an electron for a given direction. Analogously, bands are the frequency (energy) and momentum dictating the allowed wavelength bands for light propagation in a given direction of the photonic crystal. Generally thought of as dispersion in

photonics, the modes of the band structure map out all the details of the parameter space needed to understand the behavior of the EM waves. Photon dispersion takes the form of $\omega = kc/\sqrt{\varepsilon(\omega)}$ in a non-magnetic medium ($\mu = 1$) where ω is frequency, k is photon momentum, and c is the speed of light (in vacuum). The dielectric function $\varepsilon(\omega)$ can be replaced by its Drude form from Chapter I or Appendix A to give the plasmon-polariton dispersion. This hybrid of a plasmon and photon has a simple form for when the dampening scattering frequency in the imaginary part of the dielectric function is taken to zero.

$$\omega = \sqrt{\omega_p^2/\varepsilon + k^2c^2/\varepsilon} \tag{4.1}$$

The plasma frequency ω_p is the standard $\omega_p = \sqrt{4\pi ne^2/m}$, but is $\omega_p = 0$ when no plasmons are present. Following through with Equation 4.1 gives the allowed acoustic branch (massless photon) dispersion $\omega = kc$, otherwise known as the lightline. In the existence of plasmons $\omega_p \neq 0$, the dispersion switches from a linear to quadratic relationship $\omega = \frac{\omega_p}{\sqrt{\varepsilon}} + \frac{k^2c^2}{2\omega_p\sqrt{\varepsilon}}$ near the gap that has opened up. Size of the gap is given by $\omega_p/\sqrt{\varepsilon}$ and from the dispersion the photon has accumulated mass by coupling to the plasmon. This can be expanded to all band edges for the high symmetry points of the BZ, creating the isometric conditions necessary for good superlenses[92]. Using CEM methods, central to this dissertation, the photonic band structure of a designed crystal can be calculated. Within commercial CEM software CST Studio Suite, an eigenmode calculator, based on methods discussed in Appendix B, is used on the discretized model geometry of a until cell with appropriate periodic boundary conditions[7]. In short, the fundamental EM modes and corresponding field patterns are calculated for an excitation-less system. Various material combinations were simulated using dispersion-less and data modeled dielectric information.

Examples include using combinations of SiO_2, polystyrene, TiO_2, semiconductors like Si and Ge, air, $PbTe$, and water. Using the band structure calculations for various models, built up a small library of ~ 20 datasets with the hopes of applying that towards training material of a machine learning algorithm (discussed later). Primary focus was realizing, computational and experimentally, a NIM based on the photonic crystal for the purposes of subwavelength imaging.

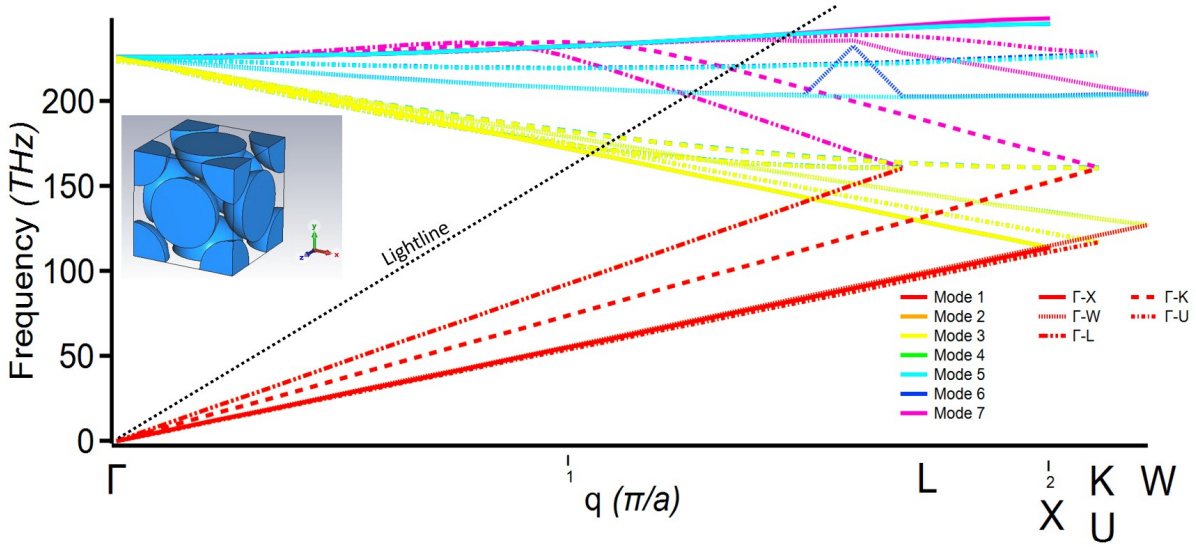

Figure 4.3: -
Calculated eigenmodes for each momentum space direction form the photonic band structure for a crystal made of SiO_2 nanoparticles in an air matrix, diameter $d = 0.725\mu m$ and period $a = 1\mu m$ (model shown in the inset). Each band is represented by different colors with red for lowest frequency up to violet for the highest. The high symmetry paths of the FCC BZ are plotted on top of each other to compare directly, each with differing line segments. Grouping of negatively sloping Umklapp bands show a refractive index of $n = -2.8$ from slope fitting.

An opal-like single crystal of silica nanoparticles is one of many examples that showed computational promise and was desired because of the simpler fabricability. One of the band structure calculations is given as an example in Figure 4.3 for a photonic crystal of silica particles in an air matrix, organized in an FCC lattice. This particular example, unit cell model shown in the inset,

used spheres with a diameter of $d = 0.725\mu m$ and index $n = 1.4$, with a lattice period of $a = 1\mu m$. Seven modes were calculated, considering some degeneracies, and span multiple directions of momentum space stemming from the high symmetry Γ point, each represented by a different color with low frequency on the red end of the spectrum moving towards violet for the higher frequency modes. For someone accustomed to examining crystal band structures, Figure 4.3 might look a bit strange in presentation. Each directional path in momentum space exists separately as lines of different dashing and thickness. Interest for this project was not to map out the band structure all possible modes of propagation but to strictly find isotropic negative refractive index (NRI), all angle negative refraction, amongst all the possible cuts of a real crystal. Therefore, the paths of interest all start at the Γ point towards the other high symmetry points on the surface of the BZ. Due to the non-spherical geometry of the FCC BZ, the momentum distance from the Γ point differs slightly for some directions but is close to uniform, denoted along the x-axis in units of π/a where a is the lattice period. As a visual aid, the lightline for vacuum is plotted on top as a scale for the relative refractive index. The first modes of the band structure (red and the degenerate orange) represent the lightline of the material. Discussed above, the acoustic branch disperses with a slope of $\frac{\partial\omega}{\partial k} = \frac{c}{\sqrt{\varepsilon}} = \frac{c}{n}$ for the assumption the refractive index is constant over the frequency range $\frac{\partial n}{\partial \omega} = 0$. These material lightlines can be used to calculate the expected refractive index for the medium anywhere the mode disperses through. Diffraction and internal interference adjust this slightly depending on which direction of propagation is taken through the crystal lattice, but generally group together. Periodicity enforces strict boundary conditions on the dispersion at the BZ edge. Umklapp scattering is the process that conserves momentum of wavevectors in periodic systems, stating that any modal point existing outside the BZ, must also exist

within the BZ[11]. Following the German instructions of the word 'umklappen', the bands 'turn over' upon reaching the BZ edge and continue on to higher energies as higher order modes. In Figure 4.3, the third (and degenerate fourth) modes for each direction work as the upper branch Umklapp of the lower branch. Noticeably, these modes have a negative slope in the dispersion, which following the relationship of the slope with refractive index implies the material is negatively refracting for that frequency range. Reaching higher frequencies (energies) than these are the higher order modes of which play an insignificant role. Light coupling to higher dispersion modes like those is a higher order effect and intrinsically less common, but are calculated to have some sense of overlap with any lower order modes. With applications in mind, grouping of the negatively slopped bands is desired and is one property of optimization. Having each mode with a nearly identical slope, thus a nearly identical refractive index, prevents any chromatic aberrations at the lens level. By toying with the materials and geometric features, it becomes possible to tune this band structure into a desired frequency range for a desired refractive index. This is just one of many band structure calculations that have now become nearly automated in setup and post-processing, allowing for rapid understanding of light dispersion properties for a desired crystal. In fact, reported band structures in the literature have been reproduced to add to this small library. The overall appearance of the band structure in Figure 4.3 is consistent with the literature. One in particular that investigates an opal-like structure in the visible spectrum achieved excellent agreement with these simulated band structures when using the same parameters[93]. Additionally, that reference saw experimental verification of the negative refraction at the expected frequency range and serves as a good guide to future endeavors on this project.

4.3 Full Wave Simulations

Band structures are informational but not necessarily demonstrative. Behavior of the bands provides the insight for the effects of the photonic crystal but doesn't mean a whole lot outside of index calculations. Which is why a common staple of the literature on this type of topic is to pair band structures with wave simulations[94]. Some examples take an effective media approach by simulating a material with an effective index of refraction that is matched to band structure calculations. Microscopic details of the photonic crystal are washed over and assumed to be working as expected by the band structure. Other examples keep these details but only simulate in 2D because of the demanding computational costs with explicitly simulating many unit cells of a photonic crystal. All these simulations are great and capture the power of negative refraction by showing image formation[92] and superlensing[90]. Even better would be demonstrating these negative refraction capabilities on a full 3D model of a photonic crystal, constructed of the unit cell details. The challenges of doing this are heavy, which is why scouring the literature yields no results. For several of the photonic crystals alluded to in the previous section, this work made incredible strides in achieving such a visualization. One example is shown in Figure 4.4 with a $PbTe$ coated, silica sphere in air matrix photonic crystal that was used to match up to the expectations of NRI geometric optics. A dipole source, oriented vertically for uniform radiation incident on the crystal, is placed a unit cell distance away. Transient electric fields show the propagation of EM waves at a constant frequency. For the crystal chosen to be displayed, silica spheres are coated with a thin $PbTe$ shell and arranged to be touching in an FCC lattice. Band structure calculations determined the expectation of negative refraction for the chosen frequency. In the 3D electric field simulations of Figure 4.4, the visualization plane is taken right through the middle of the crystal, aligned with the position

of the dipole. As discussed earlier in this chapter, a NIM can create lensing as a flat structure and when the crystal thickness is large enough, an image is formed both internally and externally. The top field map shows the propagation at a moment in time where the internal image is fully being formed, while in the bottom panel the external image comes into focus. Simulations of this caliber are rigorous, thus limiting the amount of unit cells used to replicate the exact crystal structure. Only three unit cells with periodic boundary conditions to each side are for the plane tangential to the plot and eight unit cells in length. These limitations prevent sharp, crisp images from forming, which have been improved by expanding for simpler geometries of photonic crystals that are not shown. Using Snell's law, the expressions added to Figure 4.4 are well known geometric optics expressions for ray paths provided as visual guides. The index of refraction was calculated from the slope of the simulated band structure for this crystal and was used to determine where the internal and external dipole images would be located given the distances set up in the simulation. For a successful image formation, the dipole location and crystal thickness play critical roles and have been chosen to be the best possibility of simulating a flat lens effect. Numbers from the geometric optics formulas are in excellent agreement with the simulated electric fields. Despite the supreme challenges faced with achieving a result like this that hasn't been seen before, there are still several improvements that can be made to strengthen this work much more.

Seeing the criticality that the crystal thickness has for successful image formation from a flat NIM lens, the switch to standard 2D simulations can be made. The goal of constructing a NIM lens takes more than just the verification of NRI in a material, the optics involved in image formation are essential. Figure 4.5 comes into play now for assessing the focusing power for such a lens. Simulations were performed by a colleague Rule Yi, using COMSOL

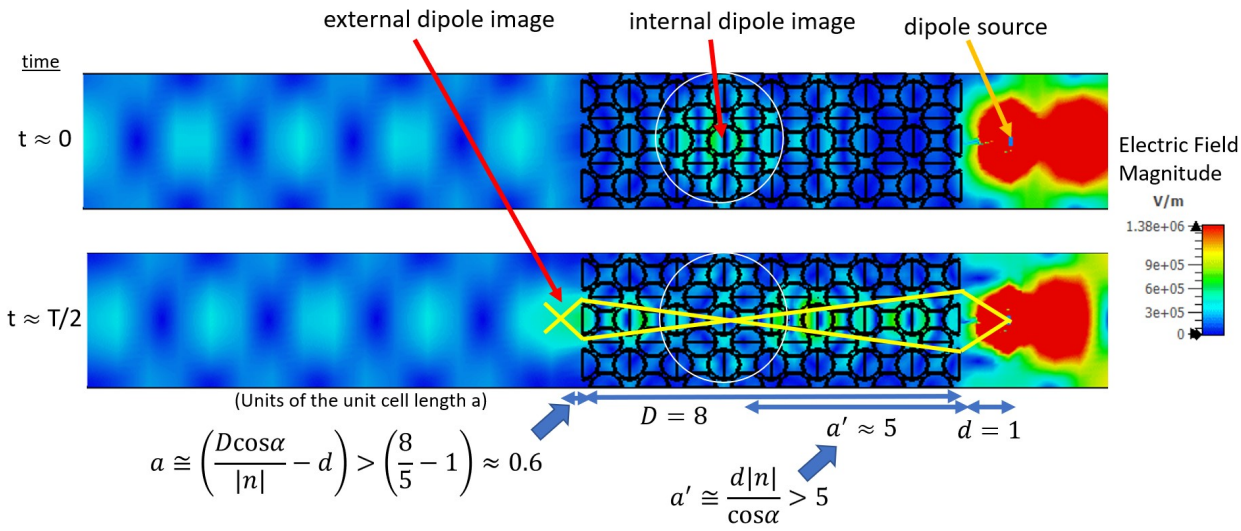

Figure 4.4: -
Full 3D EM simulations of a dipole source (one unit cell away) incident on an eight unit cell thick slab of photonic crystal. The top plot shows time condisered $t \approx 0$ where the bottom is a half-period time step later. This photonic crystal model uses silica particles coated in $PbTe$ in an air matrix. Negative refractive index is expected for this crystal at the frequency of the dipole excitation shown. Using geometric optics and Snell's law, visual guides are given to see the expected agreement with a NIM flat lens.

Multiphysics[43] to calculate the electric field magnitude of a plane wave incident on a single slit. The $6\mu m$ aperture acts as a point source, emitting isotropic EM waves of constant frequency ($100THz$) into a slab of material with an adjustable thickness. These slabs do not explicitly simulate the microscopic details of the photonic crystals, but instead use an effective refractive index for the whole lens.

Two comparisons are done between a positive index and a negative one determined from earlier band structure calculations, as well as different crystal slab thicknesses. The thinnest thickness, at $10\mu m$ is given in Figure 4.5(a) and (b) where the refractive index is set to be 1.4 and -2.9 respectively. Despite the sharp distinction in the material properties, these two plots don't look distinct from one another when comparing the overall field profile after emerging from slab lens. Negative refraction focusing power is not seen for crystals that are too

thin, which gives direction to fabrication down the line. Instead, contrasting simulations of Figure 4.5(c) and (d), where the slab thickness is now quadrupled to $40\mu m$, show strong differences. Just between them, the same indices were used and now the lensing advantages of a NIM are fully seen. Whereas for the positive index material, the EM waves continue spreading and diverging, the negative index focuses the electric field into a concentrated point before diverging. The thicker NIM slab provides the ideal lensing expected from a converging lens made of a normal material. Results from these simulations provide guidance to fabrication once the microscopic details of the photonic crystal are easily produced. Since this work was done in parallel with experimental and fabrication efforts, the following section will touch on the achievements on that front and confirming simulation/theoretical results.

4.4 Towards Fabrication

Efforts on the fabrication and confirmation side of this project were done by Nanolab Inc, famous for carbon nanotube production which is used to make one of the blackest black paints, 'Singularity Black'. Using simulation and theoretical insights, the first step is creating a crystal expected to have a NRI in a measurable bandwidth. Their work has utilized common fabrication technologies and novel processes to attempt creating self-assembled networks of spheres that can ultimately be set into an FCC lattice. Some models possess coatings on top of the spherical particles to add contrasting indices of refraction. This adds to the list of accomplishments their team pushed for fabrication of the proposed photonic crystal lenses. Shaping the lens becomes another challenge altogether, involving centrifugation. In total, the fabrication efforts are to be discussed in another place and beyond the scope of this dissertation, other than a little flavor. Example spheres on the micron-scale self-forming into a triangular lattice are

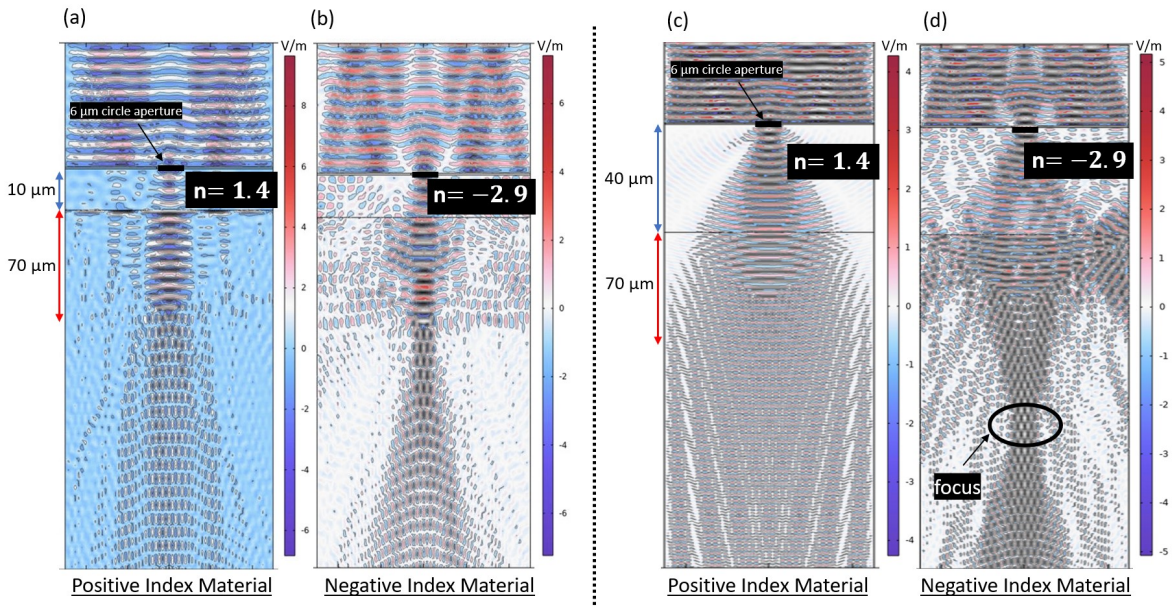

Figure 4.5: -
Using 2D computational methods, the electric field magnitude is simulated for a $100THz$ plane wave incident on an aperture. Materials are an effective medium with the microscopic details of the crystal not being explicitly simulated. Plots (a) and (b) compare positive and negative index materials at that frequency for a flat lens thickness of $10\mu m$. Plots (c) and (d) show the same but for thicker flat lenses at $40\mu m$, highlighting the criticality of thickness on lens focusing. Simulations performed by Rule Yi.

shown in Figure 4.6 as SEM images. Just as the problem with natural opal, these synthetic opal crystals show large domain boundaries. These grain boundaries inhibit the negative refraction properties that are deeply tied to the Umplapping of a BZ edge in a periodic crystal. Combined with fabrication, an experiment needs to be designed as a probe for the NRI property, both to observe and determine the value of it. The working idea is based upon literature methodologies that have set relatively straightforward procedures to the characterization of negatively refracting photonic crystals[95][96]. The general idea is to couple light directly into a photonic crystal, set up as a flat lens, where Snell's law expects a focus somewhere internally and externally of the crystal. A screen/detector is adjustable placed to be able to locate the focal point. Central

to the experiment, a material with a positive refractive index will not be able to reproduce this phenomenon and serves as an excellent control to the experiment. Figure 4.6 includes schematics that show successful and unusable setups for the experiment, simply based on geometric optics. As inspired by the work of Figure 4.5, the thickness of the photonic crystal flat lens is vital to the production of a focal point external to the crystal. Additionally, the relationship with the substrate for which the crystal is placed also influences the possibility of observing negative refraction. Relative thickness between the substrate and crystal, as well as the order of the two in which light is directed, dictates if and how far the focus will be for the detector to observe it. One consistent criterion for a successful observation is sufficiently thick photonic crystal, especially compared to standard substrate thicknesses. The success of similar experiments in the literature, coupled with the illuminating simulations, gives strong hope for the basis of negative refraction in the photonic crystals explored in this project. Transitioning all the way up to 3D systems has been quite successful from a computational and theoretical standpoint and paves the way for future work to be discussed as conclusions later.

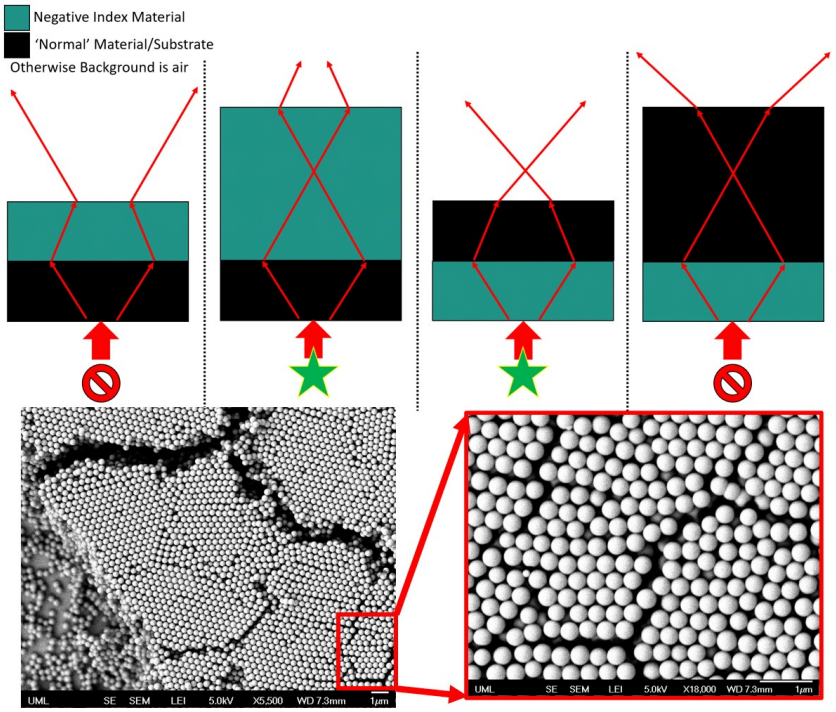

Figure 4.6: -
Four schematics provide the rays following Snell's law for a NIM and substrate experiment where light is directly coupled at the bottom to propagating upward. The order of the two layers and thicknesses are changed, showing which setups provide the possibility of observing a focusing point due to the NIM. At the bottom are micron-scale SEM images of silica particles used in the fabrication efforts of photonic crystals. SEM images taken by Nanolab Inc.

CHAPTER V

Non-Local Plasmonics

Throughout this body of work, strong definitions for the range of physical interactions have not been so explicit. For example, back in Chapter II about the checkerboard system, there was never a need to discuss the formal distinction between the inter-island(hole) and intra-island(hole) interactions. There is something to be careful of hidden in the details which is locality. As for the purposes in this work, locality is referring to the physical distance for the range of the interactions amongst objects. Electromagnetics as a whole can be thought of as non-local when compared to mechanics, simply since the forces and influences objects have on one another typically act at some separated distance. Coulomb's Law forces have far more range than say a pair of Newton's Third Law forces from two objects touching. Similarly in the checkerboard, plasmonic effects arising from island-to-island (hole-to-hole) interactions have a longer range than that of the internal island (hole) self-interactions. Though in this example, the reach is not considered to be quite large. Non-local interactions are strong interactions among neighboring unit cells of a metamaterial or even natural crystal[97][98]. Various optical phenomena can be explained by the strong electron interactions considered non-local because of a mean-free path on the scale of nanometers[99]. Quantum effects begin to show up. This is why,

generally speaking, all the work presented thus far exists in the local, or quasi-local realm where things can be taken to be local enough for a good approximation. In fact, commercial computational techniques used throughout and detailed further in Appendix B are all inherently local and can handle quasi-local problems to a good approximation. Demystifying non-local plasmonics effects requires better handling of mesh cell sizes that dip below a nanometer and the increased computational costs. To deal with anything outside those boundaries, one typically would use models based on hydrodynamics or some non-local extensions[100]. Development work is ongoing to implement non-local hydrodynamics to FDTD codes[101] as to better capture the non-local plasmonics of small feature sizes coming with the continuous improvement of nanofabrication techniques. Regardless of this computational limit for the time being, massive progress to the field still continues using non-local extensions[102] and what exactly are the differences by considering non-locality[103]. Which is exactly the case for the rest of the work detailed in this chapter, involving primarily systems where non-local effects must be considered and electron-electron interactions are strong.

5.1 Ginzburg-Kirztnitz

Superconductivity has been well-studied, and well-funded, since the very early stages of theoretical push and experimental discovery. Primarily, focuses have been about understanding how to increase the critical temperature (T_c) at which a material demonstrates the Meisner effect and has its electrical resistance drop to zero. The search for a room temperature superconductor has been extensive, which if ever fruitful, would be one of the most celebrated achievements of modern physics. Beginning with the breakthrough of cuprate superconductors of the late 1980's, critical temperatures experienced a large spike in the right

direction, up to $\sim 90K$. With reinvigoration and dedication, the cuprate family was able to produce superconducting critical temperatures up to $133K$ by 1993[104] but showing little improvement since. Theoretical explanations have even come up unclear for the driving principles and interactions of type II superconductivity displayed by cuprate materials. The central mechanism, in the conventional theory of Bardeen-Cooper-Schrieffer (BCS), is the condensation of paired electrons becoming boson carriers that are mediated by electron-phonon-electron interactions. It has already been shown that there are no expected physical limitations on BCS superconductivity blocking a push to room temperature superconductivity by Ginzburg and Kirzhnits[105]. Written first in Feynman Diagram form and then within the random phase approximation (RPA) is the full, dressed Ginzburg-Kirzhnits electron-electron interaction potential shown in Figure 5.1. It consists of two separable terms, Coulomb and Fröhlich, which specify the screened electron-electron interaction and the phonon (with frequency ω_q) mediated electron-phonon-electron interaction, respectively. The main point meant to draw attention to is the dependency on the material electrical environment properties, the dielectric function[106]. Now shown as a function of both frequency (ω) and momentum (q), due to the inclusion of non-locality, it appears in both terms in opposite flavors. Being squared in the Fröhlich term ensures that a negative dielectric environment remains strictly positive. Whereas in the standard Coulomb interaction, a negative dielectric function causes like-charges to attract and opposites to repel. There are essentially competing interactions along with thermal noise drowning out the desired electron pairing mechanisms and takes sufficiently low temperatures to induce superconductivity[107].

Coincidentally, as discussed throughout this dissertation, metamaterials are an excellent way to engineer and manipulate the dielectric function. With the

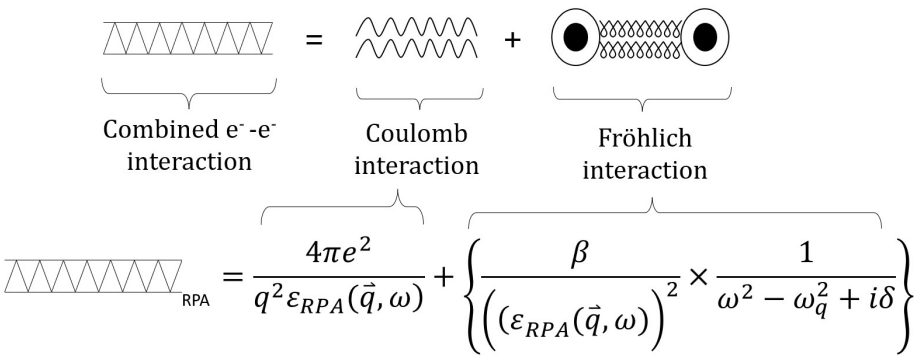

Figure 5.1: -
Feynman diagrams describing the dressed electron-electron interaction. It consists of two terms, Coulomb for the direct electron-electron interaction, and Fröhlich for the phonon mediated electron-electron interaction. Both terms are written out within the RPA formalism, with special attention to the role of the dielectric function.

reformulation of BCS theory in terms of an effective dielectric function $\varepsilon(\mathbf{q}, \omega)$ shown in Figure 5.1, there have been propositions[108] and demonstrations[109] of using metamaterials (HMM) as a way to modify the dielectric environment for a metal to improve the critical temperature. The possible exotic optical properties sponsored by metamedia have already been demonstrated in this work, which one manifestation can be an effective dielectric function with a small magnitude[110]. In the demonstrations of this combination of theory and metamaterials, it produced modest critical temperature enhancements[111] that is attributed to the locality of the effective metamedia dielectric function. So in return to the equation of Figure 5.1, there indeed is potential for boosting electron pairing but the competing interactions prove to be difficult to tip the scales sharply in favor of electron pairing.

5.2 Resonant Anti-Shielding

The anti-shielding effects a metamaterial can provide to an electron system are weak when only involving standard metamaterial effects A boost is needed. This

is where the introduction of some other effects could have the potential for better critical temperature improvement. First, let's more rigorously understand the physics of anti-shielding. Equation 5.1 takes the previous expression for the dressed electron-electron interaction potential and places it inside a jellium metal[112] consistent with Migdal-Eliashberg theory.

$$\frac{V_q}{\varepsilon} + |\frac{g_q}{\varepsilon}|^2 \frac{2\omega_q}{(\omega^2 - \omega_q^2) + i\delta} = \frac{V_q}{\varepsilon_{eff}} \tag{5.1}$$

In the equation, ε is the dielectric function for the environment, g_q represents electron-phonon scattering as a matrix element that has been averaged over all electronic states, ω_q is the phonon dispersion, δ is a small loss factor which is constant, and lastly the standard $V_q = 4\pi e^2/q^2$ for the bare Coulomb electrostatic potential. This equation represents the effective dielectric function ε_{eff} given the two interaction terms of Coulomb and Fröhlich. As described in the previous section, pairing of electrons is boosted by $|\varepsilon| < 1$, anti-shielding, but Equation 5.1 also shows pairing possibilities for frequencies around the phonon frequency $\omega \approx \omega_q$. A resonance can form which combined with an extreme dielectric environment ($|\varepsilon| \ll 1$) creates the optimal conditions for pairing, described as resonant anti-shielding (RAS). Achieving these conditions with solely just a superconductor is impossible because this metal will only have a dielectric function strictly greater than one. In the same breath, metamaterial structures alone won't be able to meet the requirements either. Sure, the resonance condition can be met, having near-zero ε when $\omega \approx \omega_q$, but this not practical for keeping locality intact. For the resonance to be met in a metamaterial, the momentum (a measure of locality) would be at $q \sim k_F$ (the Fermi wavevector). This places a geometric constraint on the metamaterial design, forcing the smallest feature sizes to be on the same order as $1/k_F$ [100].

In all, there are still two competing interactions, with the Fröhlich term accumulating the most strength by diverging $1/|\varepsilon^2|$ edging out the $1/\varepsilon$.

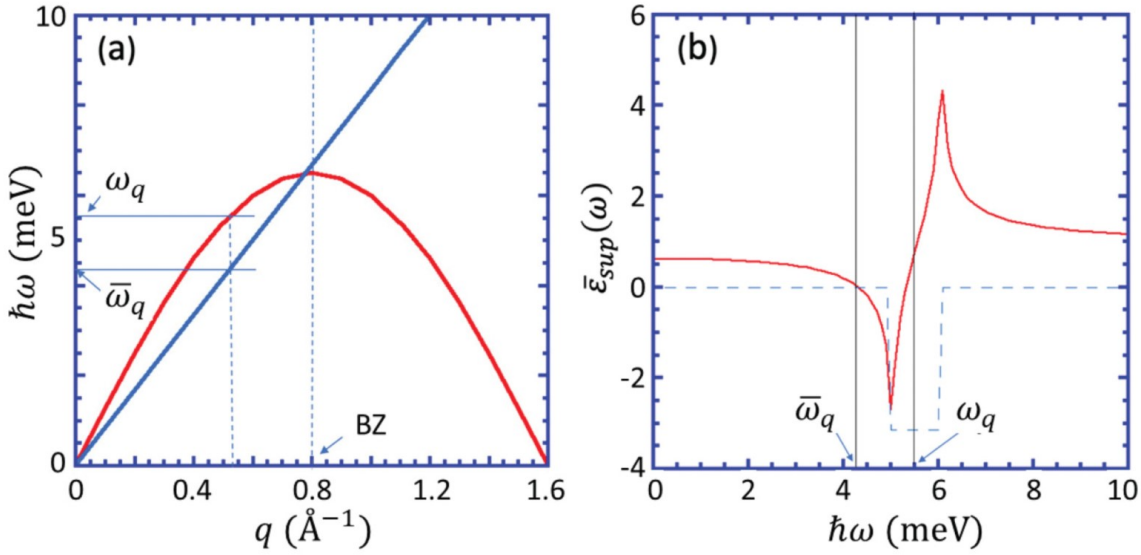

Figure 5.2: -
(a) Dispersion of two collective modes, α mode (blue line) and acoustic phonon mode (red line), for the 2D electron gas for the topological crystal Bi_2Se_3 surface. Boundary of the BZ marked and the largest frequency difference. (b) Example calculation of the dielectric function, real part (solid red line) and imaginary part (dashed blue line), using the derived relationship with the Eliashberg function. The example of a normalized step function was used for α^2F and $\kappa = 1$. Corresponding frequencies from Bi_2Se_3 carries over as vertical lines. Image credits [113].

Another way of achieving the conditions required for RAS is necessary now. Discussed in Appendix A, one set of solutions to Maxwell's equations find longitudinal modes for plasmon excitations that have $\varepsilon(q, \omega) = 0$ but at different frequencies than the phonon frequency when the momentum is on the same order as the Fermi wavevector($q \sim k_F$). Which is why typically plasmon modes won't suffice for the RAS conditions, unless they are quite abnormal. One example observed recently in the topological crystal Bi_2Se_3 is called the α mode[114]. Dispersion for this particular plasmon mode is oddly linear ($\omega \propto q$) which makes it some fixed phonon mode that will cross the Brillouin zone (BZ) without an

Umklapp folding over a mirror image due to periodicity. Plotted in Figure 5.2(a) is the interpolated experimental data for the dispersion of the α mode (blue line) alongside the typical acoustic phonon mode (red line). Follow-up work on this anomalous topological mode showed miniscule damping at a near constant rate for a wide band of momentum space that standard plasmon modes are not seen[115]. The α mode was also shown in this work to be clearly tied to the topological nature of Bi_2Se_3 since it was missing from the spectra for the other, doped form of Bi_2Se_3 that is non-topological. Instead, a typical transverse acoustic phonon mode took its place, looking similar to the Figure 5.2(a) red curve[114]. In the same theoretical follow-up study, that was consistent with experiment, the weak damping of the α mode was attributed to the forward and backward scattering being close to identical and in turn causing no Umklapp at the BZ[115]. With all these deductions about the nature of the α mode, it was reasonable to assume it lined up with the description of a plasmon-polaron, known as the collective excitation of a hybrid transverse acoustic phonon and the plasmon excitation of surface Dirac electrons[116]. This α mode in particular is tied to the topology via the 2D Dirac band surface states of Bi_2Se_3 with collective spin-charge fluctuations which makes the mode also analogous to a phonon-polariton. As a hybrid photon and phonon mode, the polariton dispersion is derived from that of photons (i.e., the light line) $\omega = qc/\sqrt{\varepsilon}$ [117], then substituting in the dielectric function from a Lyddane-Sachs-Teller phonon $\varepsilon = \varepsilon_{eff} = \frac{\omega_{LO}^2 - \omega^2}{\omega_{TO}^2 - \omega^2}$ [118]. Switching sides on the analogy, for a plasmon-polaron the starting dispersion will instead be a topological 2D Dirac plasmon[115] and now Equation 5.1 stands in as the effective dielectric function. If things are kept simple by limiting the range of phase space to only that which applies for RAS

($\omega \sim \omega_q$ and $q \sim k_F$), one will arrive at

$$\varepsilon_{TI}(q,\omega) \approx 1 + \kappa|g_q|^2 \frac{2\omega_q}{(\omega^2 - \omega_q^2) + i\delta^2} \approx \frac{(\omega^2 - \bar{\omega_q}^2)}{(\omega^2 - \omega_q^2) + i\delta^2} \tag{5.2}$$

for the effective dielectric function. The parameter κ is dimensionless is scaled by $\kappa \sim k_F/\bar{\varepsilon}^2 > 0$ with k_F specific to the electrons of Bi_2Se_3 and the frequency of the plasmon-polaron is labeled $\bar{\omega_q}^2 \approx \omega_q^2$–$2\kappa|g_q|^2\omega_q$ making it strictly smaller than the phonon frequency ($\bar{\omega_q} < \omega_q$). Having this inequality means the plasmon-polaron mode will always follow the acoustic phonon mode up to the BZ edge, but be 'lagging' behind in frequency as Figure 5.2(a) shows. Experiment and theory from the previous references on this mode confirm the negative depolarization shift in frequency.

To model and exploit the expected dielectric properties of discussed, an example sketch of a superlattice consisting of the topological crystal Bi_2Se_3 and a superconducting metal film is provided in Figure 5.3. Central to the argument is creating a dielectric environment following Equation 5.2 that is capable of promoting the RAS effect in this effective medium. Only one critical assumption is made to be a rule for this structure: the sandwiched superconducting film has a sufficiently small thickness to allow the RAS effect to permeate throughout the whole bulk of the superconducting metal ($t_{sup} < 1/q \sim 1/k_F$). The idea being that the electrons of the superconductor need to feel and experience the effective dielectric function. For that dielectric environment within this configuration, the electrons would respond according to $\bar{\varepsilon}_{sup}(q,\omega) \approx \varepsilon_{sup} + (\varepsilon_{TI}(q,\omega) - 1)$ as a combination of the standalone bulk superconductor $\varepsilon = \varepsilon_{sup}$ and the polarizability influence of the Bi_2Se_3 electrons in parentheses. Focus can now be shifted to the superconductor's phonons for control over the behavior of the plasmon-polaron. All the influential phonon bands in this part of phase space

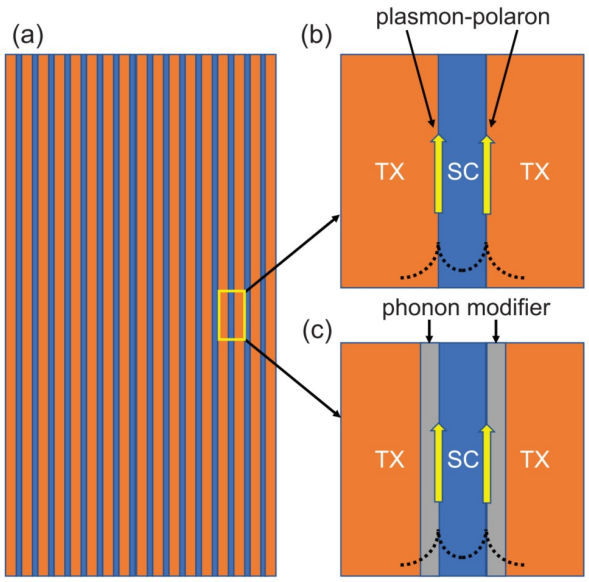

Figure 5.3: -
Schematic showing metamaterial super lattice of a topological crystal (TX, in orange) and a superconductor (SC, in blue). (a) Taking advantage of the periodicity, the structure is designed to facilitate the resonant anti-shielding (RAS) effect. (b) Zoomed in to show further detail of the expotentially decaying amplitudes away from the interfaces of the electric field produced by the plasmon-polaron propagating with the (yellow) arrows. (c) A possible optimization to the structure includes buffer layers of a phonon modifer (in gray), allowed by the topological proximity effect pushing the plasmon-polaron still to the superconducting surfaces. Image credits [113].

can be introduced to Equation 5.2 while simultaneously reducing the constraint of the jellium model. After the algebra is cleared up, which can be seen in more detail in Reference [113], the main takeaway from the new $\tilde{\varepsilon}_{sup}(\omega)$ is the transformation of the electron scattering matrix element into a form of the Eliashberg function, essentially the phonon density of states. The Eliashberg function, $\alpha^2F(\omega)$, is dimensionless, has been renormalized, and is now directly proportional to the imaginary part of the dielectric function when in the limit of increasingly smaller loss δ. For many materials, the Eliashberg function is known, either through measurements or theoretical calculations. This makes the parameter κ the main 'unknown' within the effective dielectric function of the

Figure 5.3 topological crystal-superconductor metamaterial. Estimates can be taken from standalone experiments on the topological crystal (Bi_2Se_3). For now, it is left as a tunable parameter for calculations but started with the assumption will be that $\kappa = 1$. An example Eliashberg function can be plugged in to get a feel for what the dielectric behavior will look like such as a single rectangular peak that maxes out at $\alpha^2F(\omega) = 1$ for a set frequency range, otherwise is $\alpha^2F(\omega) = 0$. Returning to Figure 5.2(b), the total effective dielectric function has the real (solid red line) and imaginary (dashed blue line) parts plotted. Both panels of the figure come together by seeing for the value $q = 0.53\mathring{A}^{-1}$ (partial vertical dashed blue line of Figure 5.2), the difference between the phonon frequency and plasmon-polaron frequency is in agreement, $\Delta = \frac{\omega_q - \bar{\omega_q}}{\omega_q} \approx 20\%$. This window of frequency shown in Figure 5.2 as thin, vertical, black lines provides the optimal window for RAS with this model effective dielectric function. Now the Eliashberg function is screened and can be written as $\alpha^2\bar{F}(\omega) = \alpha^2F(\omega)/|\tilde{\varepsilon}_{sup}(\omega)|^2$. What's left to do is apply this formalism to a real example and calculate the effects on superconducting critical temperature.

5.3 Enhancment of Superconductivity via RAS

While the scheme just outlined to modify the dielectric environment for the superconducting electrons is novel, applying that to calculate critical temperatures is well established. Ab initio calculations of the coupled Eliashberg equations[119][120][121] are solved directly and used to calculate the supercoducting critical temperature[122]. Detailed steps are provided in the guiding paper for this chapter of work and its corresponding supplemental material[113]. One main note for these calculations is the differences between the two possible equation system solvers, isotropic and anisotropic. Both solvers deal with some known inaccuracies where the isotropic tends to underestimate T_c

while the anisotropic overestimates T_c by roughly the same amount. It felt better to take the more conservative approach, so the isotropic solver was used, keeping the anisotropic results as self-consistent verification. In support of these calculations, there is the additional T_c calculation idea of the ab initio Leavens scaling method[123] to achieve an accurate electron-phonon coupling function that reduces any RAS randomness. The basis of this method is to provide the upper limit to the critical temperature and not T_c directly, seen in Equation 5.3.

$$T_c^{max} = c(\mu^*) \int_0^\infty \alpha^2 F(\omega) d\omega \tag{5.3}$$

The function $c(\mu^*)$ is of the Coulomb pseudopotential μ^* that is dependent on the Fermi energy, double Fermi surface average of the screened Coulomb potential, and density of electrons for the superconductor. Overall, this term is monotonically decreasing as a function of the Coulomb pseudopotential and can be determined from looking at experimental results on a material-by-material basis[122][123]. Rewriting Equation 5.3 now using the anti-shielding formulism for the Eliashberg function gives

$$T_c^{max} = c(\mu^*) \int_0^\infty \alpha^2 \bar{F}(\omega) d\omega = c(\mu^*) \int_0^\infty \frac{\alpha^2 F(\omega)}{|\tilde{\varepsilon}_{sup}(\omega)|^2} d\omega = \frac{c(\mu^*)}{\kappa\pi} \int_0^\infty Im(\frac{1}{\tilde{\varepsilon}_{sup}(\omega)}) d\omega \tag{5.4}$$

using the relationship established between the superconducting dielectric function and the Eliashberg function. Using both critical temperature calculation methods, each having the RAS scheme implanted, select materials can be used as an example to see if RAS gives any enhancement. Sticking to conventional BCS superconductors first, MgB_2 has been renowned as the highest T_c material (at standard pressure) of the BCS type. The layer stack-up of Figure 5.3 now considers the interfacing of MgB_2 and Bi_2Se_3 where literature gives the

value of $\mu^* = 0.16$ to be plugged in for MgB_2[122][123]. Resulting calculations for T_c^{max} by the Leavens approach (solid colored lines) and for T_c by the ab initio Eliashberg calculations (filled red circles) are plotted in Figure 5.4(a) against the parameter κ. Recall κ represents the strength of the screening effects in RAS, beginning at $\kappa = 0$ where there is no screening at all. This would represent the expected critical temperature under standard conditions with no RAS. For MgB_2, experiments have routinely shown $T_c = 39K$, significantly lower than the isotropic Eliashberg equation approach solution of $T_c = 23K$. Of course, an underestimate was expected so it is important to check what the anisotropic solver for what the overestimate is, seen as the open red circle at $\kappa = 0$ and $T_c = 54K$ on Figure 5.4. As κ increases, the critical temperature increases until a sharp maximum at $\kappa = 1.3$ where afterwards is a dramatic fall off. After hitting roughly $100K$ (4-fold enhancement), the critical temperature immediately dips below $10K$ getting to $\kappa = 1.4$. In the second method of solutions, Leavens scaling, the trend is clearly similar. Keeping in mind this is T_c^{max} now, for no shielding effects ($\kappa = 0$) the critical temperature is remarkably close at $T_c^{max} = 43K$. The curves follow along the ab initio Eliashberg points well, with deviations only occurring at the most significant point of the maximum to minimum area of $\kappa = 1.3$. Mathematically, Equation 5.4 is diverging at the RAS condition of $\tilde{\varepsilon}_{sup}(\omega)$ becoming extremely close to zero. The screened Eliashberg function becomes singular which can be resolved by artificially adding some dampening in an imaginary term to the effective dielectric function. A way to think about this contribution is by considering the inserted $i\zeta$ term as scattering from impurities with the idea in mind to damp down the divergence to something more numerically appropriate. For the different colored lines plotted in Figure 5.4 using the Leavens method, the factor for ζ was changed, leaving the general behavior the same.

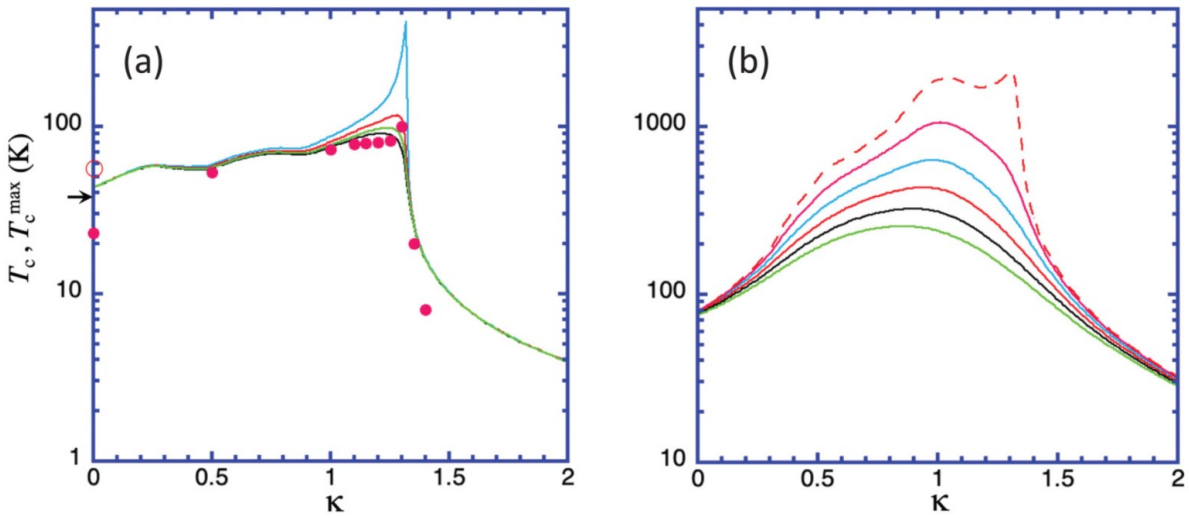

Figure 5.4: -
Using the resonant anti-shielding (RAS) with both the ab initio Eliashberg equation formalism and Leavens sscaling method, the critical temperatures can be calculated for a real superconductor in the superlattice scheme. Eliashberg equations give solutions for T_c (solid red circles for isotropic, open circle for anisotropic), while Leavens method gives T_c^{max} (lines for different damping parameter ζ), both in Kelvin. Along the x-axis is the coupling parameter κ. (a) MgB_2 where the arrow gives the experimental T_c. ζ: 0 (blue line), 0.005 (red line), 0.008 (green line), and 0.01 (black line). (b) MgB_2 with phonon modifier layer of $YBCO$. ζ: 0.01 (dashed red line), 0.05 (purple line), 0.1 (blue line), 0.15 (red line), 0.2 (black line), and 0.25 (green line). Image credits [113].

Viewing the results from both calculation methods, particularly the divergence within the Leavens scaling approach, it seems the structure stack-up can use some optimization. Having the superconducting material phonons in total control of the plasmon-polaron behavior, consequence of relaxing the jellium model constraints, is too dominant when the dielectric function vanishes. Figure 5.3(c) shows a new idea that introduces an intermediary layer to the topological crystal (Bi_2Se_3) and superconductor (MgB_2) sandwich. This layer is to serve the purpose of being a phonon modifier and should ideally be a non-phonon mediated superconductor. Enough phonon damping should be introduced yet leave the dielectric environment roughly the same. Introducing this extra

consideration to the metamaterial involves the experimental data for the Eliashberg function of $YBa_2Cu_3O_{7-\delta}$ ($YBCO$), a well-known high T_c superconductor[124]. $YBCO$, and the rest of the cuprate family, fall into the mysterious typing of superconductors with the exact mechanism of superconductivity still being an active research topic. On top of the Eliashberg data, $YBCO$ can also be found to have $c(\mu^*) = 0.2$ [122][123] making it possible to evaluate the ab initio Eliashberg function calculation in Equation 5.2 and then use the Leavens scaling approach in Equation 5.4. Figure 5.4(b) plots the results for this configuration of the metamaterial, beginning first with the absence of screening ($\kappa = 0$). Experimental results give $92K$ for the $YBCO$ critical temperature while calculations of the metamaterial scheme of Figure 5.3(c) estimate a maximum of $80K$. Similarly to the previous case, the coloring on the curves varies ζ the damping parameter. Once again, the region of interest with the largest T_c^{max} that rapidly falls off is at $\kappa = 1.3$ but in this scheme there is more of a plateau for the highest max critical temperatures. The sharp divergence for the higher values of κ is significantly reduced with the incorporation of larger ζ values, becoming a smooth curve for $\zeta \geq 0.1$. Taking the modest reaches for these curves, one could suspect that these structures are capable of providing room temperature superconductivity ($T_c > 300K$). Evidence suggesting superconductivity within already studied materials can be enhanced, raising the critical temperature, by this metamedium approach is tied to the parameter κ. The primary way for this to be adjusted is directly through the topological crystal. Since the plasmon-polaron is harbored within, the dispersion features really set the coupling parameter. Controlling the Fermi surface of the topological insulator, by playing with doping levels, affects k_F and in turn the direct proportionality of κ. Otherwise, indirectly messing with the metamaterial superlattice geometric properties, like thicknesses and/or extra

dispersive materials, can result in changes to the background dielectric constant $\bar{\varepsilon}$. Future work set on realization of these materials could be investigating further these parameter spaces. One such unique effect that has recently come to attention, the topological proximity effect, could help couple the plasmon-polaron of the topological crystal better to the phonons of the superconductor. Seen at the interface of a sibling material to the topological crystal explored here, $TlBiSe_3$, and BCS superconductor Pb, the topological state was able to bleed into the 20 monolayers of the Pb superconducting film without any state mixing[125]. Combining this with the phonon modifier layers concept would also expect a strengthened coupling of the quasi-particles and increase to a more homogeneous dielectric environment. Such materials could be made chemically versus through nano-engineering though. The previously discussed cuprate family of superconductors are known for their $CuO2$ layers surrounded by the non-conducting heavy metal oxide layers (yttrium, bismuth, etc.). These already have a familiar look when compared to the structures proposed in Figure 5.3. If some topological characteristics could be incorporated (chalcogenide layers), then these materials might have a similar dielectric environment capable of hosting RAS. One trick to all this was covered up a little by the use of MgB_2 as the superconductor. The Eliashberg function of MgB_2 is active at higher frequencies than other superconductors, Pb for example. Phonons are more active in the relevant phonon frequencies, allowing for such a large effect to take place. Nonetheless, this should only begin the worthwhile study of applying the coupling of a topological crystal surface plasmon-polaron and electron-electron interaction of a superconductor. Resonant anti-shielding (RAS) is effective regardless of the mediation and pairing mechanism for the Cooper pairs. The possibility of superconducting critical temperatures being enhanced through a fabricable geometry is theoretically shown, leaving

experimental verification up in the air.

CHAPTER VI

Conclusions

6.1 Reflection, Discussion, and Outlook

As the bookend to this sequence of extensive work, I thought it would be nice to shift the voice and break the narration character I've stuck to throughout this dissertation. I want to make my conclusions from my own voice and perspective. A significant amount of effort has been put into it from the very start of my research, even the start of my higher physics education, and I would like the chance to wrap it up. In my mind, it is safe to say that from covering these topics over the years and pushing on the forefront of research, my knowledge is among the best. Not in a bragging way, but in a way to establish my credentials further. It's no secret that I enjoy educating others on these topics and physics/EM as a whole. My hope is that in reading this, you have taken something away. Whether that is practical and can be applied to your work or even just as an interesting bit of knowledge you found consumable, either way accomplishes what I've set out to do. The rest of this chapter will be working to fill in that gap in case you are still unsatisfied. For each chapter, my thoughts and ideas, at the end of writing each, will cap off the topic. I'll provide a little outlook on the future, suggesting possible directions to go. Each chapter holds merit to me, and I thoroughly support anything that builds off it. Comments,

expansion, criticism, whatever, it's all valid and appreciated.

6.1.1 Checkerboard Series Plasmonics

For myself, the work on checkerboard structures will be one of my most favorite projects. Not only did the origin feel organic, but it also felt personal. Little did I know how much work out there was already done on the structure, and even by my own advisor. It felt natural to jump into it. As an avid chess player for some time now, though not great, the geometry of the board is so simple but can be used in the most mind blowing of ways. Indeed, it was not so surprising to find that even in plasmonic ways, this simple checker pattern can really make you think. For starters, I couldn't even get the unit cell correct without a little extra thought. The bowtie series of patterns spawned out of this and found an interesting spot to have as a novel comparison. But spanning through the percolation threshold really interested me. You can immediately see the phase of the structure change and the physicist in you will scream that there must be interesting physics there. The same simplicity but hidden complexity in an idea can be carried over to the Babinet principle. Without much thought, the special circumstance of the checkerboard being self-complimentary is a connection between the two that holds much intrigue. Fascinating but seemingly trivial, a flashlight on a sheet of checkerboard and holes gets half the intensity through. Then taking that to the interesting length scales only further entrenched the plasmonics standpoint. Arriving at the colormaps for the transmittance, I'm astounded how vibrant those came out. A plot like that I think right away is depicting good science and great data. Lobster diagrams have become something for me that I see something new and interesting each time I look one over. There's a lot of data to appreciate in color plots like this that made seeing one in the literature more captivating. Breaking the Babinet principle was unexpected,

but the hints had been there from some of the other work that is tied to Chapter III. This is one thing that you need to double check, again and again, to ensure that you're getting the right results. When everything you've tried continues to come to the same conclusion, a certainty builds up. Resemblence to the Hofstadter butterflies in the literature is remarkable and shows just how much more there could be to explore on such a simple topic. This is one project I want the most discussion from. There needs to be questions and debate, all leading to further testing. That would really excite me to follow where it goes and what can be uncovered. Frequencies in the EM spectra span a great deal of ranges. It would be nice to see what else can be explored on other scales. Geometry clearly wasn't all tied to the square shape. Various other lattices of geometric patterns could be designed to add a whole other layer of complexity, like with the hypocycloids. Additional dielectric pieces set into the geometry added a welcome twist. Really honing in on what role dielectrics can add and optimimizing those material properties stands as a good future project. Especially gearing towards the semiconductor type of corner contacts. I think there is an engineering problem there at this point about explore the ways to exploit the doping of a material making up the contacts of an underpercolated checkerboard. To sum up this work, it really was the combination of two simple ideas and finding the right way to combine them. The literature on this topic is quite enjoyable. References with Chapter II make for a good push to expand on the topic. I'd like to know, what did you appreciate the most in this chapter?

6.1.2 Multi-layer Structure Extraordinary Optical Transmittance

With my feelings towards the standard checkerboard patterns of Chapter II, the care and effort put into the scaled up multilayer series should come as no shock. Chronologically, first came the work on the nanosphere structures. Once again

there is something so trivial, where normal incidence looks to be completely reflecting. However, the added height gained from their being two complementary layers stacked on each other throws doubt into the simplicity. Stemming from the novel fabrication techniques touched on in the chapter, having a system ready to be modeled so that simulations can be compared to already performed experiments is a fun approach. The refinement of the model, the mesh, and the constant comparisons felt like an untraditional method of running simulations. It always feels like calculations are naturally run first. Of course, designed to help prototyping and narrowing down on a design before production, simulations also need their benchmark moments. This was certainly it. Comparisons directly were very tough because creating the exact conditions of the experiment on the computer was not straightforward. The decision of incorporating the missing scattering into the experiment is tricky. Typically, experimental data is the gospel. I've heard before a couple times now that everyone believes in an experiment except for who performed it, and no one believes simulations except for who set them up. In this example, modifying the experimental data to better reflect what the simulations were calculating felt like the better choice. Not only was it easier to incorporate phenomenological scattering, but it also makes more sense than to un-consider it in simulations. Cutting something out of the accurate model of reality is to compare to an experiment which ignored that something feels like an omission of truth. Typically, models are an overly simplified system, but in this case, it took fewer assumptions. Really, it is just unfortunate that we couldn't figure out a setup or redo any experiment that better captured the whole system. All this and still I think there is exceptional agreement between simulation and experiment. Unfortunately, the same can't be extended to the multilayer checkerboards. My feeling is that there can be a lot done to better the modeling and simulation side.

I find that there a still several inconsistencies with the checkerboard transmittance calculations that need to be resolved before criticizing any experiment. There is a relationship to the scaling parameter of the checkerboard complimentary pairs that doesn't seem correct the further you dive into it. One of the parts that does hold a lot of promise would be how the thicker spaced models show the Rayleigh-Woods anomaly feature. There are strong similarities with the checkerboards that have a large spacing and the systems typically discussed with the Rayleigh-Woods anomaly. I would suggest continuing with this topic for some interesting plasmonics to arise and other EOT testing grounds. Overall, the EOT effect is interesting but not unexpected. Though the systems in Chapter III are simple to the naïve, toy models and literature searches tell you that these multilayered structures are dip into a broader understanding of the underlying plasmonics. CEM proves to be invaluable when exploring such areas. Nothing is more powerful though when simulations can be combined with measurement. Agreement on two fronts makes any study that much more respectable. As with most of the work in this dissertation, I wish to see more experimental follow up and comparison to simulations. For the nanospheres, it becomes closer to an engineering problem now. There is preliminary work on using devices like those studied here as different types of sensors. Use of the checkerboards in possible filter applications can be a significant push pending better investigation. Nanodevices and structures are capable of some really cool feats and technologies based on them could become groundbreaking. It feels good to contribute to that effort. I'll be curious to see what turns into common use out of this field. With that though I'll leave off with a question to you the reader, what is most promising for applications in this work?

6.1.3 Negative Refractive Index Photonic Crystals

There is a natural line of logic that follows from learning about Snell's law, which is taught typically fairly early in physics curriculum. After seeing diffraction and putting math to the phenomenon you see in the world quite often, the fact that the index of refraction is bound to being only 1 for a vacuum and strictly greater for 'any other' medium is quite odd. This, of course, is rooted in Maxwell's equations being relativistic with no fuss and that anything other than that bound on the index of refraction would allow for faster than light speeds. It feels like a very hard and set rule that can't be broken. Seeing any other index of refraction, negative for example, feels like an absolute violation of relativity. But then as a student you move on to see how the index of a material is related to the electric and magnetic properties. In this case particularly, the dielectric function of a material is the critical component to the frequency dependence of the index. Moving into my line of work, where manipulating the dielectric function is the entire purpose, the strange possibilities seem more attainable. In fact, negative refractive index is not some fable or fantasy or even some inconsistency, the literature has been showing it repeatedly since the seminal work of Pendry. Conceptually, the idea of light bending backwards when refracting can seem a little rough around the edges. I think that when you start to see the animations and color plots, 2D and now 3D, of the electric field patterns inside a capable material, it begins to click. The wave patterns evolving over the course of the crystal lattice, bouncing around until focusing, is a great demonstration. Probably is the reason why it is so common in the literature for the topic. All this work is done with collaboration, something that makes reporting specific data and exact numbers a little touchy. So, excuse my vagueness in that chapter for this reason. But with the amount data collected, there is a small library to peruse through when getting involved with this work.

Numerous combinations of materials and geometric sizes with the goal in mind working towards training data for a machine learning algorithm. Designing and fabricating a negative refraction lens is one feat, but another is to have the design so parameterizable that with the machine learning algorithm any set of important qualities can be input. Perhaps there is a specific frequency band of interest or an exact lens size that must be considered. Ideally, given a vast library of data on photonic crystal band structures, the algorithm could search for the right geometries and materials to give a band structure that meets the specifications. This is a real long term and will require a lot deeper of an understanding on the connection the band structure has to the operability of a lens constructed out of the given parameters. Near term steps is the reproduction of the experiments suggested in Chapter IV. Seeing negative refraction in a designed crystal and measuring the index of refraction to match simulations is a monumental step. Our collaborators are working hard on the fabrication and measurement side, so there is hope that this can be realized soon. Improvements can definitely be made on the simulation end. Simulations of the full 3D crystal and lensing effect are not trivial, as discussed in the chapter. Several steps can be taken to better those and create really outstanding images and movies of the phenomenon. Band structure calculations on the other hand are like clockwork. Nearly automated and fit well when compared to similar structures in the literature. Plotting the band structures in an unconventional way is one thing that requires adjustment. If you're used to seeing plots like this in the context of real crystals, perhaps with semiconductors or topological crystals, it feels like overkill. But ensure the best possible lens requires true isotropy that avoids any chromatic aberrations. Understanding these plots isn't about the behavior of each band on its own, but about how the bands group together. A unique twist to any condensed matter physicists typical view on the topic. Nonetheless, I find

the material to be easy to explain and of course even better to demonstrate via simulations. My hope is that you've see how straightforward something as alien-like as negative refraction is. Snell's law and band structures are things well understood to many of my readers but are just taken to a different level. One question I have for you, how exotic do you really find negative refraction?

6.1.4 Non-Local Plasmonics

I know the chapter was dedicated to non-local plasmonics and the application was to superconductivity, but how can we not discuss superconductivity more. Superconductors are fascinating to me. It is somewhat of a shame that superconductivity hasn't become formally entrenched in the physics curriculum. We hear about it all the time, in many contexts, yet still there isn't a common course, or even dedicated chapter of a course, offered that really builds up the well-studied topic. Until it possibly comes up in your research, there is mostly only self-teaching on the subject. However, in the academic community, superconductivity remains very active. Throwing in the little twist of metamaterials and plasmonics, there has been enough shown to hint at some valuable work to be had in this crossover. For this chapter, more 'pen and paper' theory needs to guide along any computational efforts. Since commercial CEM softwares are limited without non-local extensions, the same conveniency as some of the previous work isn't afforded. But that doesn't make exploring the topic impossible. Using two calculation schemes here, one calculating the critical temperature while the other finds its limit, adds some self-consistency I find necessary in simulations. Traditionally, using different algorithms in opposite domains is a strong way to get a good check on results. As done for work in the previous chapters, comparisons between two sources of data boost the confidence of the results significantly more, especially when opening up to the community.

Although, declaring results that might be a little too good to be true was certainly a fear. There is always a constant search for an error being made when you want to claim something as illustrious as 'room temperature superconductivity'. I'd like to take the opportunity to be clear again about this though, the calculation estimates the maximum critical temperature. It is entirely possible for one reason or another, impurities, approximations, etc., that measurements won't see such peak values. Speaking of measurements, this would be the obvious follow-up to our work. Whether using the suggested systems or venturing into the organic, naturally layered high temperature superconductors, there is the expectation of interesting evidence in support of the calculations. Fabrication of the topological insulator and superconductor sandwich lattice would take effort and numerous attempts. Then measuring transport, 4-probe for example, is equally challenging to set up, but could be very worthwhile. That is ultimately what I hope to have shown to you. The experimental push and pursuit of this endeavor would be fruitful, either confirming or disagreeing with the theory. A more recent development on this topic is once again a cross-over back to the tried-and-true checkerboard pattern. Taking a look at the calculated dielectric function of the effective layer made up of checkerboard, similar desirable qualities are noticed that can be applied in RAS. Simulations show scaling of the checkerboard geometry to be consistent with scaling of the spectral features, so shifting to applicable energy (frequency) ranges of the Eliashberg function is not out of the question. Perhaps the addition of hole structure geometry to the metamaterial structure would only bring benefit to the onset of superconductivity via phonon coupling. With the connection between the checkerboard and nearly all the work presented in this dissertation, it feels like it should be in the title. The real physics though, lies in the hidden plasmonic intricacies of the structure and has made for an enlightening system to test out

strange optics, and more. I appreciate all the work of the collaborations involved with the projects in Chapter V and know that there is hopefully more to come on the project. For my final question to the audience, I'd be interested in hearing, how potentially game-changing can you see this approach being?

6.2 Closing Remarks

Collecting and compiling all my graduate schoolwork into one centralized location has been satisfying. Not often do I feel like a full-on scientist but in seeing all the accomplishments come together, it's hard not to feel like there has been advancement. Certainly, on my individual level this is true. I dream of advancement in a broader sense, pushing the forefront of knowledge. The contributions made to a doctorate reach this level of achievement, so my hope is you walk away feeling that is true. Each project I've worked on has been intellectually challenging and rewarding. I've always found interest in what I do and hope that has carried over into writing this piece. I am proud to forever be attached to this work. If even one person can use something gained from learning from me, the goal will be accomplished. Science progresses, and to will that continue to be passed down, as it has to me. One quote I've come across that perfectly concludes any body of scientific work is by René Decartes, an extraordinary mathematician. So as the for closure and the last thought, I leave his words as a wonderful finale.

"I hope that posterity will judge me kindly, not only as to the things which I've explained, but also to those which I have intentionally omitted so as to leave to others the pleasure of discovery."

-René Decartes

APPENDICES

APPENDIX A

Introduction to Electrodynamics and Relevant Physics Background

A.1 Introduction to Electrodynamics and Relevant Physics Background

Electromagnetics, as a field of study, predominately started solely as empirical observations of near-magic, invisible phenomena. Even magicians in modern times still utilize electromagnetic effects in attempts to hide the underlying trick. However, no trick can go unexplained now. After a rigorous 19th century revolution in mathematics, physicists began to accurately describe these mysterious electromagnetic forces and have developed one of dominate theories in all of physics, classical electromagnetism. As a pillar of modern physics, every student of the subject finds themselves taking multiple classes on EM. While this appendix is no attempt to supplant that information, it should serve to supply enough relevant background on EM for a comprehensive understanding of this dissertation.

A.2 Maxwell's Equations

At the foundation of EM, the mathematical framework for which electrical and optical technologies are built upon, are Maxwell's equations (A.1a)–(A.1d) (differential form) and the Lorentz force law (A.2). Under Maxwell's description of EM, the intense tangling between electricity and magnetism is quickly noticed. On both sides of the equations there are electric fields (E) and magnetic fields (B) that make this classical field theory work in harmony. The equations themselves can be written in several different equivalent forms, including integral and within a given media, but written as coupled partial differential equations, we can come to a heuristic understanding.

$$\nabla \cdot \mathbf{E} = \frac{\rho_e}{\varepsilon_0} \qquad \text{Gauss's law} \tag{A.1a}$$

$$\nabla \times \mathbf{E} = -\frac{\partial \mathbf{B}}{\partial t} \qquad \text{Faraday's law} \tag{A.1b}$$

$$\nabla \cdot \mathbf{B} = 0 \qquad \text{Gauss's law for magnetism} \tag{A.1c}$$

$$\nabla \times \mathbf{B} = \mu_0 \mathbf{J} + \mu_0 \varepsilon_0 \frac{\partial \mathbf{E}}{\partial t} \qquad \text{Ampère's law} \tag{A.1d}$$

$$\mathbf{F} = q\mathbf{E} + q\mathbf{v} \times \mathbf{B} \tag{A.2}$$

In descending order, first, there is Gauss's law that relates an electrical source to its corresponding field. Electrical charges, defined as a charge density (ρ), are the standard producers of electric fields as explained by Gauss's law. The divergence operator (∇) takes the vector (directional) electric field and gives in its place the scalar (single number) field that corresponds to the quantity of sources (to the vector field) for each point, i.e., charge density. Equivalently seen in the integral form Gauss's law, one can imagine a closed surface (Gaussian surface) or study

the illustration of Figure A.1, encompassing some charge, and the net flow electric field produced by those charges going through that surface is directly proportional to how much charge is enclosed. The constant of proportionality is the permittivity of free space (ε_0), a universal constant describing the density of electric fields permitted from a source of charges in a vacuum. Predominately used in standard unit systems as a unit place holder, so we can treat it as such like any notorious theorist. Beyond this, Gauss's law serves as one of the top headaches for plenty of introductory students.

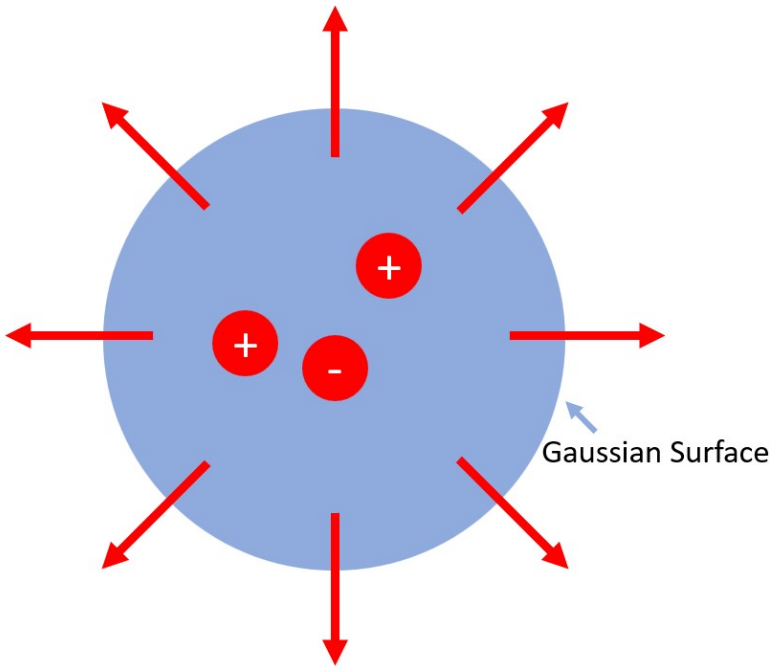

Figure A.1: -
Illustration for a Gaussian sphere surrounding charges. Gauss's law states that the flux of electric field through any imagined Gaussian surface is directly proportional to the amount of charge enclosed.

Second on the list doesn't really go by a name but is being adopted more regularly as Gauss's law for Magnetism due to the similar appearance of the divergence operator. Now magnetic fields take center stage as the operated on vector field but with one striking asymmetry to electrical Gauss's law: instead of

a charge distribution there is nothing. Profound ideas can be drawn from asymmetries, seen in this dissertation, but few rival the conclusion of this Maxwell equation. This zero in the equation states that there are no magnetic analogues for electrical charge. Electric charge comes in two flavors, positive and negative, each of which can be isolated as a monopole. In magnetism, north and south, magnetic flavors, cannot exist individually. Instead, magnetic fields are attributable to dipole sources. Thinking about the integral form of this equation, it becomes easy to see why this must be the case. The flux of magnetic fields through a surface enclosing some magnetic 'charges' being strictly equal to zero leads to saying the total magnetic charges sum up to zero. In other words, they must always come in pairs as to cancel each other out, for any and all closed surfaces you can imagine. Magnetic fields being constructed of solely dipoles additionally gives a great way to view the distinction from electric and magnetic fields now. Magnetic dipoles are generally represented by loops of current (or inseparable north and south poles). By drawing the magnetic field lines of a dipole, it's seen that they are simply just loops, with no beginning or end. This counters electric fields which have positive and negative charges as the start and end points for the electric field lines, respectively. It is well worth pointing out that there has been (and to some extent still is) an extensive search for isolated magnetic monopoles[3]. This is one way to help answer questions about charge quantization, but for our purposes, there are no magnetic monopoles.

Transitioning back to electric fields, the third Maxwell equation is known as Faraday's law. Michael Faraday *sparked* the investigation into electromagnetics, mainly empirically, and is rewarded with bearing name to a fabled Maxwell equation. Faraday's law might possibly be the hardest subject matter introductory students face in EM. From the conceptual nature of Lenz's law to the now intertwining of electric and magnetic fields, by far students struggle.

Here however, stripping down Faraday's law will begin with the new operation the del operator is taking on the electric field, the curl. Mathematically, taking the curl of a vector field, an electric field in this case, returns another vector field where the length and directions correspond to strong circulation of the electric field. A circulation density if you will. We see that is equivalent to the time rate of change for the magnetic field. Moving away from the more mathematical language, this is called induction. Spatial circulation changes of an electric field directly correspond to time-varying magnetic fields. Taking this a step further and looking at the integral form of Faraday's law, a changing magnetic flux can create and change an electric field, while spatial changes in the electric field can create and change magnetic flux. It takes work to move a charge around a closed loop, and by Faraday's law, this is equal to the rate of change of magnetic flux through the enclosed surface. Some can overgeneralize this to the point where we can electric fields can induce magnetic fields and vice versa. Induction is widely used in modern electronics as a scheme to transition one form of energy into another (mechanical into electrical energy for example). The connection between electricity and magnetism cannot be overstated. We see now that one doesn't exist without the other, they go hand in hand. Things are now stunningly interesting in the world of EM, with still one Maxwell equation to go.

Last and certainly not least of Maxwell's equations is Ampère's law. Applying the curl operator now to the magnetic field gives us the last building block of EM theory. Once again, it is easy to notice how different the equation appears when compared to its electric counterpart, Faraday's law. Magnetic fields just have one more layer of complexity to them it seems. On one side we have the curl operation on the magnetic field representing that vector field of infinitesimal circulations within the magnetic field. The other side has now two terms to describe the corresponding to this equivalence. Historically, Ampère's law only

had the singular term that introduced magnetic sources to the picture. Similar to Gauss's law where there were electrical sources, magnetism uses current as its source, denoted as current density (J). This also introduces, in the standard unit system, another universal constant. This time for magnetism, the permeability of free space (μ_0) serves as a quantifier for the relative strength of magnetic fields produced by currents. In the original Ampère's law, it is quite similar to Gauss's law but instead for equating the generation of magnetic fields with the amount of current inside a closed loop (where it was charges and closed surfaces for electricity). In the form stated in Equation A.1d, there is an additional term necessary that was apparent to Maxwell (Maxwell's Correction). In static cases, Ampère's law didn't make much sense, prompting the introduction of the displacement current. This shows that not only electric currents are associated with magnetic fields, but now these displacement currents, which refer to electric flux, do as well. This now completes the circle of self-generation of fields. Electric fields changing to induce magnetic fields. Magnetic fields changing to induce electric fields.

Electromagnetics has now come full circle, finally arriving at the personal conclusion drawm from Maxwell's equations: electricity and magnetism are synonymous. Don't take this super literally, for what is being conjectured is that there is not a discussion of one without the other, they must go together. These are not two separate phenomena, but instead one, with carefully intertwined and twisted components. And while it can be thought of as the comnclusion of EM theory since everything is encapsulated here, this is also the start. From here, the rules have been layed out and the game can begin. Now, electromagnetic theory can explode.

A.3 Electromagnetic Waves

To start on EM waves, a quick description of a wave in general would be helpful. A wave is the collective disturbance of some medium, which is about as general and vague as it gets. Since waves come in many shapes and types, it's hard to really define them all in one shot. They can be propagating, like transverse and longitudinal waves, or a standing wave which doesn't propagate at all. The wave velocity isn't necessarily fixed that depends on the medium. A medium may not even be required at all, as is the case with EM waves. Many more qualifiers can be attached, so it is better to start with repetition of the disturbance. Mathematically, this looks something like $f(z,t) = f(z - vt, 0) = g(z - vt)$ which simply states that whatever shape of this waves disturbance f is, it gets repeated at some time later after a distance shift of vt where v is the wave velocity propagating in the +z-direction. Many functions adhere to this simple constraint and can all be considered valid waves. However, the truest test to get narrow down the specific waves that can exists for a system, is if they are solutions to the wave equation.

$$\frac{\partial^2 f}{\partial z^2} = \frac{1}{v^2}\frac{\partial^2 f}{\partial t^2} \tag{A.3}$$

Here is the classical wave equation in 1D, a linear, second-order differential equation. All solutions are of the form described broadly above and since Equation A.3 is linear, then the sum of any two solution is also a valid solution. Without diving too much into the specifics of wave physics, for which there are textbooks and courses worth of material, this can be applied to EM immediately for the purposes of this appendix. Taking Maxwell's equations (A.4a)–(A.4d) in the source-less context, with no charge or current, and in vacuum, they can be algebraically massaged to decouple the two fields E and B.

$$\nabla \cdot \mathbf{E} = 0 \tag{A.4a}$$

$$\nabla \times \mathbf{E} = -\frac{\partial \mathbf{B}}{\partial t} \tag{A.4b}$$

$$\nabla \cdot \mathbf{B} = 0 \tag{A.4c}$$

$$\nabla \times \mathbf{B} = \mu_0 \varepsilon_0 \frac{\partial \mathbf{E}}{\partial t} \tag{A.4d}$$

Starting by applying a curl operator to both Equation A.4b and Equation A.4d and using some differential calculus identities

$$\nabla \times (\nabla \times \mathbf{E}) = \nabla(\nabla \cdot \mathbf{E}) - \nabla^2 \mathbf{E} = \nabla \times -\frac{\partial \mathbf{B}}{\partial t} = -\frac{\partial}{\partial t}(\nabla \times \mathbf{B}) = -\mu_0 \varepsilon_0 \frac{\partial^2 \mathbf{E}}{\partial t^2} \tag{A.5}$$

and

$$\nabla \times (\nabla \times \mathbf{B}) = \nabla(\nabla \cdot \mathbf{B}) - \nabla^2 \mathbf{B} = \nabla \times \mu_0 \varepsilon_0 \frac{\partial \mathbf{E}}{\partial t} = \mu_0 \varepsilon_0 \frac{\partial}{\partial t}(\nabla \times \mathbf{E}) = -\mu_0 \varepsilon_0 \frac{\partial^2 \mathbf{B}}{\partial t^2} \tag{A.6}$$

Finally applying the other equations in the set, Equation A.4a and Equation A.4c arrives at

$$\nabla^2 \mathbf{E} = \mu_0 \varepsilon_0 \frac{\partial^2 \mathbf{E}}{\partial t^2}, \qquad \nabla^2 \mathbf{B} = \mu_0 \varepsilon_0 \frac{\partial^2 \mathbf{B}}{\partial t^2} \tag{A.7}$$

3D, separated wave equations for E and B. They are of the exact form of Equation A.3 where the velocity then becomes $v = \frac{1}{\sqrt{\mu_0 \varepsilon_0}} = c = 2.99 \times 10^8 m/s$. Light is an EM wave and better yet is forcible transverse, meaning that there is no oscillation in the direction of propagation, due to the pair of Gauss's laws. Faraday's law takes the relationship of the two fields even further. Recall how E and B are co-generating each other, as concluded earlier from Faraday's and Ampère's law. From this the relation between the amplitude of the two

oscillating fields that are forcibly in phase and mutually orthogonal is $B_0 = E_0/c$. To aid in visualization of the wave, Figure A.2 shows a simple example of an x-direction polarized EM wave propagating in the z-direction. The wavelength and frequency of an EM wave are related through $f = c/\lambda$ and spans the whole EM spectra presented in Chapter I. By imposing boundary conditions on the wave equations and understanding how they differ for each medium (see the next section), virtually any problem can be approached.

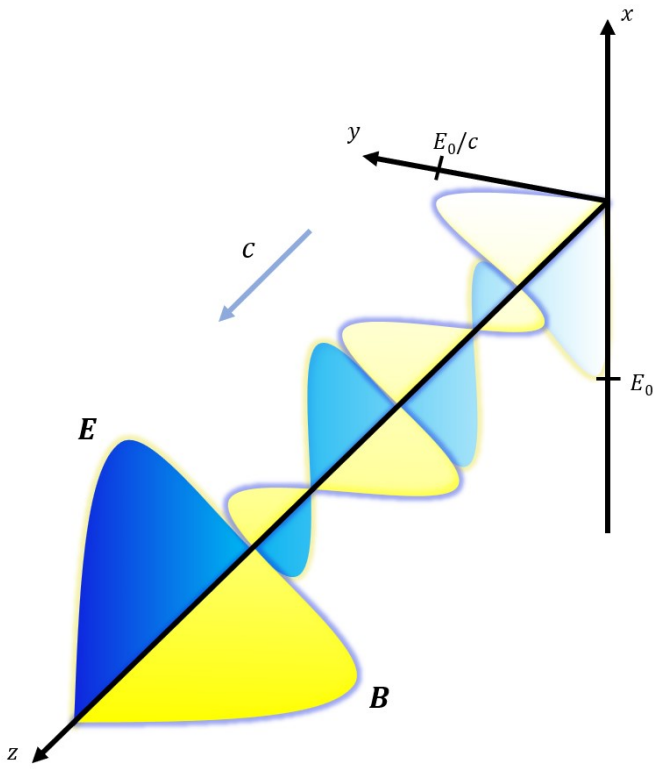

Figure A.2: -
Using the solutions to the wave equation, one possibility is a transverse plane wave where the electric and magnetic fields oscillate in orthogonal directions, while propagating perpendicular to both. In a vacuum, c is the speed of light and the field magnitudes are related by $B_0 = E_0/c$. This example shows the electric field polarized to in the x-direction.

The first condition applied to the EM waves that extends to real world problems, like those of Chapter II and III, is guided waves. A waveguide is assumed to

continue to infinity and be made of PEC such that the hard boundary condition of no fields penetrating the material is enforced ($\mathbf{E}^{\parallel} = 0$ and $B^{\perp} = 0$). Maxwell's equations in the set of (A.4a)–(A.4d) still make the rules for the waves confined in this manner but are also constricted to the boundary conditions. One big difference with confined waves now is the possibility of being longitudinal, having oscillating field components in the direction of propagation. Figure A.3 sets the example geometry for the waveguide. So, in the wave equation that has the 3D ∇^2 operator, each component can have a term. Solving the wave equation this generally requires the use of the separation of variables technique and is going to yield deeply coupled field equations. By knowing the longitudinal components, the rest can be determined with some differentiation, so by following the details of Reference [1] or [3], those components are plugged into Maxwell's equations to arrive at the uncoupled form

$$\left[\frac{\partial^2}{\partial x^2} + \frac{\partial^2}{\partial y^2} + (\omega/c)^2 - k^2\right] E_z = 0, \qquad \left[\frac{\partial^2}{\partial x^2} + \frac{\partial^2}{\partial y^2} + (\omega/c)^2 - k^2\right] B_z = 0 \quad \text{(A.8)}$$

These equations determine what are the allowed forms to waves that conform to the boundary conditions of a waveguide. For example, taking $E_z = 0$ are the transverse electric (TE) modes where there is no electric field component in the propagation direction. Counter to this is the solution when $B_z = 0$ with no magnetic field component in the propagation direction, designated as transverse magnetic (TM) modes. For a hollow waveguide, as illustrated in Figure A.3, no TEM mode can exist since there is no valid solution if both propagation direction components are non-existent. This can be remedied if a separate conductor is placed in the middle of the waveguide, creating a coaxial transmission line type of situation. In such a case, TEM modes can exist since the potentials of the walls and center surfaces aren't necessarily equivalent.

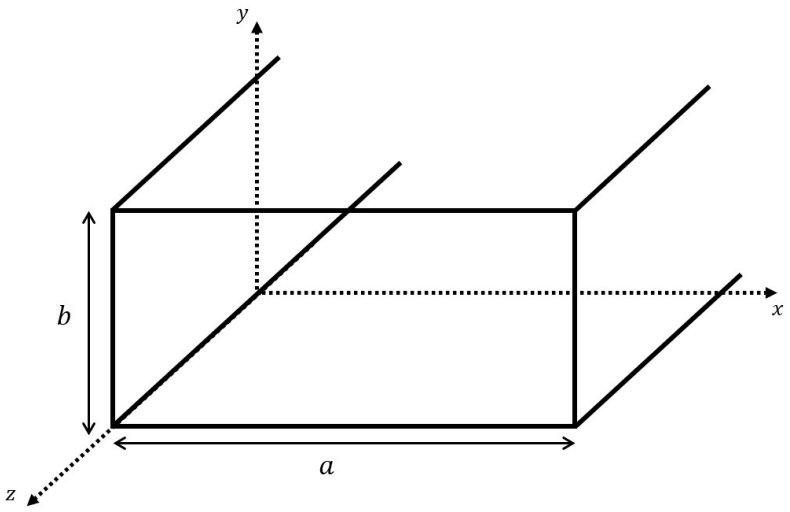

Figure A.3: -
A rectagular waveguide with edge lengths a and b supports the propagation of fundamental propagating modes like TE and TM.

To solve Equations A.8 for the particular geometry of Figure A.3, separation of variables is once again applied to both the E_z and B_z equations. This insures separable x and y solutions for the fields which after the algebra comes to a general solution of $f(i) = Asin(k_i i) + Bcos(k_i i)$ for both terms $i = x, y$. Required by the earlier boundary conditions, the waves need to disappear at $x = 0$, $y = 0$, $x = a$, and $y = b$. Forcibly, coefficient A needs to vanish as will since a sine wave with no phase isn't capable of abiding by this. In the end, only suitable values of k will suffice to fit in the waves, leaving the final conditions that

$$k_x = m\pi/a \quad (m = 0, 1, 2, \dots), \qquad k_y = n\pi/b \quad (n = 0, 1, 2, \dots) \tag{A.9}$$

Values of the integers m and n signify the mode number for the TE_{mn} modes and a similar derivation can be done for the corresponding TM_{mn} modes. Returning the conditions of Equation A.9 to the general separation of variables solution, gives the exact expression of Equation 2.3 in Chapter II telling exactly

what frequency waves will have exponential attenuation in the waveguide. The details and derivations are beyond what is necessary here are outside the scope and illustration accompaniment this appendix has for this work. Feel free to reach out to any favorite EM textbook[1][3] to satisfy any missing curiosities.

A.4 Within a Medium

Matter, of course, adds dramatic effects to EM behavior. If everything happened in a vacuum, there'd be nothing fun to study. Generally, and for the purposes of this work, materials fall into two lump categories: conductors and insulators.

Conductors, like metals, have free valence electrons, allowing them to disassociate from any nucleus and move about the material wherever necessary. Insulators on the other hand, do not permit their electrons to have the same luxury. Materials such as dielectrics have only bound charges and only have an atomic sized amount of wiggle room to work with. The contrasting behavior of these two classes of mediums is what makes the metamaterials that combine the two studied in this work so interesting. Confinement is something electrons in either material can experience, whether that is around an atom for insulators or the edges of metallic structures for conductors. This is what makes these two material types polarizable. That is to say, if an external electric field is applied, the electrons necessarily respond (importance of the dielectric function), shifting to an energetically favorable location. In conductors, the electrons will travel to the furthest edge they can, following the potential gradient. The resulting positive ions left behind and shifted electrons form a dipole like concept bound to the metallic structure. Depending on the shape of said structure, more exotic fields can be created for on an oversimplified example, the structure has become polarized into a dipole. Similar in dielectrics as well, only on the smaller scale of being bound to an atom. Electrons being tied to the nucleus with only small

shifts the electron cloud possible, creates built up negative and positive charges on opposite ends of the atom/molecule. Miniature dipoles with the material are formed in this external electric field that when all summed together for the collective medium, effectively create an induced dipole of the whole insulating system. Atomic polarizability is the term used in this situation which can be used to determine the internal, induced electric field within the material. More pertinent details on the dielectric response of a material have already been supplied in Chapter I the introduction. The parallel discussion about an external magnetic field acting on a medium is omitted, as the details aren't directly related to the interest of this work. Albeit quite interesting themselves, standard EM[1] or solid state[11] textbooks go into much better detail than what can be provided here.

General discussions of EM in matter are hard to do without either getting into specific qualifiers or taking up chapters of work. To refrain from either, this section is meant to just give enough background material for the work provided in this dissertation. The previous section began EM waves from their origin in Maxwell's equations. However, inside a medium other than vacuum, there first are adjustments to this equation set. Firstly, the displacement field takes the place of the electric field within a material and differentiates it from any external field. Similarly, the same goes for the magnetic field, which is turned into the auxiliary field when inside matter. Cumulations of bound charges and currents within materials make it more convenient to use that notion instead. The reasoning being that those bound sources an intrinsic to the materials response and not directly controlled, thus rewriting Maxwell's equations to refer explicitly only to the free charge and currents that are controlled makes it simpler. Which is when the smoke clears of including the polarization and magnetization, Maxwell's equations become Equations (A.10a)–(A.10d) for inside a medium.

Further simplification can be made if generality is lost and the material is assumed to be linear or has a frequency dependent response or is away from any free charge/current, as seen in Chapter I.

$$\nabla \cdot \mathbf{D} = \rho_{free} \qquad \text{Gauss's law} \tag{A.10a}$$

$$\nabla \times \mathbf{E} = -\frac{\partial \mathbf{B}}{\partial t} \qquad \text{Faraday's law} \tag{A.10b}$$

$$\nabla \cdot \mathbf{B} = 0 \qquad \text{Gauss's law for magnetism} \tag{A.10c}$$

$$\nabla \times \mathbf{H} = \mathbf{J}_{free} + \frac{\partial \mathbf{D}}{\partial t} \qquad \text{Ampère's law} \tag{A.10d}$$

Under the assumption that the material is indeed linear ($\mathbf{D} = \varepsilon \mathbf{E}$ and $\mathbf{H} = \frac{1}{\mu}\mathbf{B}$), is where the adjustment happens for how fast light moves once in a medium. The free space permittivity and permeability now take into account the materials response and then EM wave velocity becomes

$$v = \frac{1}{\sqrt{\varepsilon \mu}} = \frac{c}{n} \tag{A.11}$$

where the index of refraction is defined as $n \equiv \sqrt{\frac{\varepsilon \mu}{\varepsilon_0 \mu_0}}$. This becomes particularly important in Chapter IV when relating the materials dielectric response function to the index of refraction. In most cases, including those important to this work, again the magnetic response is not of keen interest and for the materials in question $\mu \simeq \mu_0$ (and for most materials). Leaving the index of refraction of a medium as $n \cong \sqrt{\varepsilon}$. The consequence of this is that light inside a medium is nearly always less than c, therefore slower, aside from a few special circumstances. For EM waves at the interface between two mediums, there are two possibilities: reflect or transmit. This forms a simple conservation statement that whatever percentage of the wave goes either direction, the total must be

equal to what was incident. Coefficients are given to the reflection and transmission, R and T respectively, to serve as a measure of the energy that falls into either category. By energy conservation, $R+T=1$ for the interface between two contrasting indices of refraction. More complicated systems, like the reflection and transmission through a whole material (or metamaterial) also will have the additional absorption coefficient since there is more than the one interface. For now, R and T are ratios of the intensity at that interface. Intensity is the average power per unit area and is directly proportional to the square of the field (E for example). Through careful consideration of the boundary at the interface and the material properties on either side, expressions for the coefficients can be written down explicitly in terms of the indices of refraction.

$$R \equiv \frac{I_R}{I_I} = \left(\frac{E_R^0}{E_I^0}\right)^2 = \left(\frac{n_1 - n_2}{n_1 + n_2}\right)^2 \tag{A.12}$$

$$T \equiv \frac{I_T}{I_I} = \frac{\varepsilon_2 v_2}{\varepsilon_1 v_1}\left(\frac{E_T^0}{E_I^0}\right)^2 = \frac{4n_1 n_2}{(n_1+n_2)^2} \tag{A.13}$$

These expressions are for normal incidence. Switching the assumption to an oblique angle if incidence is how the law of reflection, Snell's law (law of refraction), Fresnel's equations, and Brewster's angle can be derived, as done in an EM textbook[1][3]. The point being that the multitude of geometric optics expressions are explicitly derived from EM and are rather straightforward compared to other subfields. Work in optics goes hand in hand with the rules of EM, and only becomes more involved and intertwined from here when other considerations are met (non-linearities for example).

References cited in this chapter serve as the basis for material presented with the select chose topics meant to only scratch the surface of EM but be sufficient in covering most details used in this work. For any additional questions and reading on the background material, the references are highly suggested and warrant a

massive amount of credit for the understanding necessary to get to this point.

APPENDIX B

Techniques in Computational Electromagnetics

B.1 Techniques in Computational Electromagnetics

Maxwell's equations are the governing analytical expressions for a theoretical understanding of EM in virtually any system, see Appendix A. While in principle this is outstanding, in practice there are complications that can make achieving a thorough analytical solution quite rigorous, in some cases borderline impossible. There are longstanding fields dedicated to exploring accurate and reasonable approximations that have their place but when it comes to problems with complex geometries, tricky scaling, and intense interactions, searching for analytical expressions seems insane. And it is! The amount of work it would take to understand solely the electric fields of a single SRR at one particular frequency is already daunting. Let alone including other calculable quantities, parametric adjustments, interactions, broadband sweeping, etc. would compound the effort. By giving up on the pipedream of arriving at a closed form solution to Maxwell's equations the world becomes immediately more explorable. Algorithms in CEM step in to make all of these problems a lot more tractable.

The multiple forms and representations of Maxwell's equations, combined with numerous mathematical techniques, form the several standard algorithms that are used in CEM. In general, and covering the usage within this dissertation, the formulation revolves around discretizing space and time into a meshed cell grid where Maxwell's equations can be solved for each point. Electric and magnetic fields throughout the calculation grid are the typical results for which numerous other properties can then be determined. With the various approaches and approximations splitting off from there, the main branches will be detailed further. Two, generally competing, strategies are divided by calculation domains. There is the time domain, with EM excitations and responses calculated transiently in discrete time steps. There is also the frequency domain, with Maxwell's equations written in a Fourier transform to be expressed and solved as functions of frequency. With other approaches out there beyond just these two, each algorithm focuses on its advantages to fit into a particular niche of problems. Mathematics within each method of solution tends to bode well for certain problems compared to others. The problem parameter space is usually depicted along two orthogonal axes. One is how electrically large the system of study is which provides a gauge for the amount of computational power required, in terms of memory, needed to solve the problem. To put it into different terms, this scale is also an identification for the size of electrical features in the problems, how intricate the details are. For the other axis in this parameter space, the problem can be categorized by the size of the bandwidth being investigated. Problems with sharp resonant features would require only narrow windows of frequency to be probed while other systems might require a bigger picture of the spectra. Regardless of the demands of the problem, the point is that there exists an optimal algorithm to investigate, and that choice is indeed important. Of course, there is overlap between these solvers, which provides a

unique window to have added verification and self-consistency within these problems. In each of the following sections, the solvers used in this dissertation are broken down to provide an overview into the calculations performed and algorithmical advantages.

B.2 Time Domain

Calculations within the time domain are colloquially clustered under the banner name FDTD (finite-difference time domain) and is quite common and popular because of its ease of use. This is a full wave solver, meaning that there are no simplifications made to Maxwell's equations at the beginning and the full EM wave propagation is calculated. Additionally, the discretization of space and time is done volumetrically into a lattice grid, comprised usually of hexahedrons. Maxwell's equations are taken in their form of partial differential equations with respect to space and time and discretized by a mathematical method known as central difference approximations. With the collection of the mesh cell grid and partial differential equations allocated to each cell, the solutions are formed by leapfrogging. Exampled in Figure B.1, leapfrogging is where the solution at one particular field (electric or magnetic) is built upon the previous time step of that field and the intermediary time step of the opposite field (magnetic or electric). The process is done until a predetermined stop criteria is reached. Due to the transient nature of the calculation and stepping forward in time, the stop criteria is usually some desired steady state of the EM fields. This for example could be energy based, like in the TD calculations in this dissertation, where there needs to be a set energy decay from the domain, normalized to the peak value. Methods following this general approach have been around for a long time in other contexts, fluid dynamics for example[126], so there exists many offshoots that trying to focus on certain strengths or improving upon weaknesses.

Advantages of FDTD, beyond its ease of use for starters, stem around the transient dynamics of the algorithm. Problems where there is a transient effect trying to be understood have a more direct means of calculation in this domain when compared to others. This adds a strong versatility to types of problems that can be solved where they can both be wide ranging in electrical size and size of the bandwidth. In terms of computational resources, the cost of solving problems this way scales linearly with the amount of mesh cells and allows for easy to implement GPU acceleration techniques[7]. Disadvantages in this domain arise because of the transient nature. For example, in systems with multiple excitations, each individual source is typically calculated in series with one another. For large systems, this could cost plenty of time. Similarly, with the time domain being advantageous for broadband calculations, narrowband poses some difficulties. The time signal pulses, usually Gaussian, have a length in time that is inversely proportional to the frequency band under investigation. In these narrowband problems, the time signal pulse could be extraordinarily lengthy and take a long simulation time to reach the stop energy decay criteria. Exactly in the same resonant structures could also create issues. The stop criteria requiring energy to decay to an appropriate amount for an adequate solution significantly goes against resonant behavior having energy be trapped in the system some. More nuanced pros and cons exist for time domain EM calculations, which can be saved to be explored in further resources[127], but for this is satisfactory for a surface level understanding desired in this appendix.

Specific to the commercial software used for this dissertation, there are two, time domain, full wave solvers for EM in CST Studio Suite. The flagship solver being based on the finite integration technique (FIT) that has its foundations in topologically protecting conserved quantities like energy and charge. Instead of using Maxwell's equations as partial differential equations, the FIT algorithm

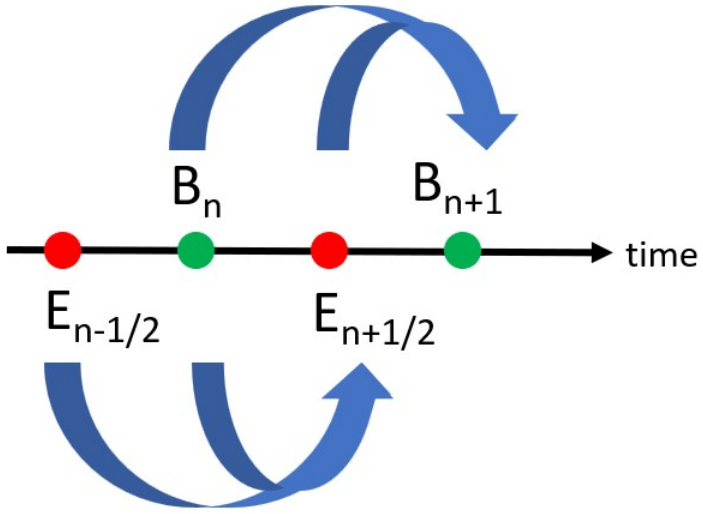

Figure B.1: -
Diagramatically showing how time domain solvers leapfrog in time. Each field at a particular time step is dependent on the corresponding field at the previous time step and differing field at the previous half time step.

takes them in the integral form on a hexahedral mesh grid discretization. There is flexibility in the modeling and material properties that make the FIT algorithm one of the most versatile, and when combined with leapfrogging, achieves a computational resource efficient protocol. The other critical solver algorithm used with this bod of work, usually for verification purposes, is the transmission line matrix (TLM) method. A matrix/grid is set up to be a network representation of electric circuit elements, essentially working off an analogy between EM fields and transmission line grids. A similar versatility to the FIT algorithm and is quite powerful in specific applications/models. Achieving agreement between FIT and TLM solvers is not necessarily a challenge, generally, but stands as a useful resource for obtaining confidence in CEM solutions.

B.3 Frequency Domain

Within the frequency domain, this general class of algorithms is dubbed FDFD (finite-difference frequency domain). Transforming Maxwell's equations into a reciprocal representation in frequency space opens a cluster of other mathematical techniques and tricks for numerically arriving at a solution. Algorithms following this sequence are also an industry staple and widely used in the applied world. As will any of the differential, not integral, solution methods in the time domain, the basis is finite-difference approximations taken on the partial differential equations. Each derivative operator is replaced by tiny differences where the approximation improves the closer these differences get to infinitesimally small. With the equations transformed into frequency space, solutions for the fields are determined for a single constant frequency. This allows for a matrix representation where the advantages of linear algebra can be exploited. To solve for a range of frequencies, algorithms can employ various interpolation or discretization strategies[128]. Discretization is still critical, with the necessity mirroring that of time domain methods for all the same reasons: uniform handling of boundaries, increasing mathematical ease for manipulating curl equations, and a conscious avoidance of divergences. Of course, there are no time steps in this method, differing from FDTD. This allows calculations to be done out of sequence which can be a double-edged sword. Compared to the time domain counterpart, FDFD methods can be computationally costly. Computers do handle large linear systems with many unknowns quite well, but there can be system and model complexities that compound the resources required, especially memory. This scaling between the electrical system size and the computational resources depends on whether the frequency solver is taking an iterative or a direct approach, but regardless scales faster than time solvers. With this in mind, the ideal calculation is traditionally narrow in bandwidth. Because the frequency

solver is working at a constant frequency for a set resolution of sampling points, the wider the bandwidth creates a significantly longer simulation time. The advantage of this is seen when looking at resonant structures, a weakness in the time domain. Scanning narrow bandwidths allows for supreme resolution for sharp peaks caused by system resonances. Additionally, the stop criteria is based off residuals instead of energy decay in the domain, allowing for more accurate and quicker calculations when the electric energy is more efficiently stored by the system for longer time scales. A further unique advantage in the frequency domain is when a system has multiple excitations. By not taking time steps, each excitation can be simulated simultaneously with ease, counter to the time domain where this is sequential. There are a significant portion of problems that fall standard to FDFD algorithms because of this. Overall, it is important to consider both time and frequency domain solvers for a problem at the beginning and allow for specifics to narrow the ideal methodology.

Within the work for this dissertation, the commercial software CST Studio Suite has a frequency domain solver using the FEM (finite element method). The corresponding meshing is based on tetrahedrons, which is not as robust as the hexahedral mesh used in the time domain[129]. However, for the applications and models simulated in this body of work, there is a lot of overlapping coverage between frequency and time methods. Of course each has their advantages, but because these problems can be approached by both types of algorithms, one can use them as self-check. The power in CEM is being able to test and study a system with unparalleled ease and with high accuracy. There's no better consistency in these terms than achieving agreement on multiple solvers, using completely different meshes and mathematical techniques. Theoretically, Maxwell's equations are the ultimate truth for EM, and showing that a problem gets to the same numerical answer via distinct solutions provides enormous

confidence moving forward with experiments. CEM is toolbox with many tools inside that can get the job done, and ultimately to provide the guidance and support to strong experimental verification.

B.4 Miscellaneous

Beyond time and frequency domain calculations, there are some lesser used solvers but still serving equal importance. Just as there are strengths and weaknesses to the previously outlined solvers, the various other miscellaneous solvers have their areas applications. For example, some other solver methods widely used are: MoM (method of moments), BEM (boundary element method), FMM (fast multipole method), PEEC (partial element equivalent circuit), MLFMM (multilevel fast multipole method), SBR (shooting bouncing ray) method, AKS (advanced Krylov subspace) method, JDM (Jacobi-Davidson method), and so many more. This large handful of an even more massive set of solvers that exist, each with unique application spaces. Some are still based in frequency space, MoM and MLFMM for example, with others falling under completely different categorization[130]. In some way or another, this list of numerical methods has some effect on the work in this dissertation, albeit small in many cases. The purpose of this section is to give some light to some of the lesser-known solvers and their impact on this body of work.

A powerful analysis for investigating systems without excitations uses either AKS or JDM algorithms. Calculations of fundamental EM modes and their corresponding field patterns can provide insight into certain effective media, which would be calculated using one of these methods. Beyond EM applications, these solvers expand into sensitivity analysis by calculating structural deformation from detuning effects. Meshing is naturally still critical but allows for more freedom of choice between hexahedral and tetrahedral meshes. In

general, these methods are categorized as eigenmode solvers. A fitting name because they essentially are just solving eigenvalue equations for the electric and magnetic fields[131]. By combining Maxwell's equations to form the notorious wave equations for both fields, and writing them as functions of frequency, these methods solve for those eigen-frequencies and corresponding eigenmodes. Specific to the AKS method, input parameters are required to give estimates for the highest eigenmode desired. On the other hand, JDM is more robust but more computationally costly for calculating more numbers of modes. It can handle degenerate modes quite well, which makes it a prime candidate for applications in photonic band structure calculations for photonic crystals. Nonetheless, the eigenmode solvers are still iterative like many of the listed CEM methodologies, so nailing down an accurate answer will always take some physical intuition of the system.

From the very first codes and algorithms to the modern, high-powered solvers with parametric 3D graphics, computation of electromagnetics has found its base as an integral step for any analysis of EM systems. Whether the applications are for a new product or for fundamental research, there is power in taking the initiative to understand the problem from the perspective that is the closest representation to pure theory. Numerical methods are only improving and being able to handle more complex models. Being able to explore a system, making countless changes, at a fraction of the fabrication costs and time, is something that benefits all our further advancement of knowledge. When used properly, with the strong understanding of EM, there is no doubt that high accuracy results can be achieved, with confidence.

BIBLIOGRAPHY

[1] Jackson, J. D. *Classical Electrodynamics*. 2rd. United States of America: John Wiley & Sons, 1975.

[2] The Radicati Group. *Forecast number of mobile devices worldwide from 2020 to 2025*. http://www.statista.com. Statista, 2022.

[3] Griffiths, David J. *Introduction to Electrodynamics*. 4th. United States of America: Pearson Education, 2013.

[4] Burger, Sven Zschiedrich, Lin Pomplun, Jan and Schmidt, Frank. "Finite-element based electromagnetic field simulations: Benchmark results for isolated structures". In: *Proc. SPIE Photomask Technology* 8880 (2013). DOI: {10.1117/12.2026213}.

[5] Hoffman, Johannes Hafner, Christian Leidendenberger, Patrick Hesselbarth, Jan and Burger, Sven. "Comparison of electromagnetic field solvers for the 3D analysis of plasmonic nanoantennas". In: *Proceedings of SPIE Europe Optical Metrology* (2009). DOI: {10.1117/12.828036}.

[6] Sankaran, Krishnaswamy. "Are yoy using the right tools in computational electromagnetics?" In: *Engineering Reports* (2019). DOI: {10.1002/eng2.12041}.

[7] *CST Studio Suite*. http://cst.com/products/cstmws. Version 2018/19/20/21/22/23. Dassault Systèmes.

[8] Chen, Zhizhang Wang, Chao-Fu and Hoefer, Wolfgang J. R. "A Unified View of Computational Electrodynamics". In: *IEEE Transactions on Microwave Theory and Techniques* 70 (2 2022), 955–969. DOI: {10.1109/TMTT.2021.3138911}.

[9] Toll, John S. "Causality and the Dispersion Relation: Logical Foundations". In: *Physical Review* 104 (6 1956), 1760–1770.

[10] Lou, Liang-fu. *Introduction to Phonons and Electrons*. 1st. United States of America: World Scientific Publishing, 2003.

[11] Ashcroft, Neil W. and Mermin, N. David. *Solid State Physics*. 1st. Canada/United States of America: Brooks/Cole Cengage Learning, 1976.

[12] Wang, Y. Plummer, E. W. and Kempa, K. "Foundations of Plasmonics". In: *Advances in Physics* 60 (5 2011), 799–898.

[13] Ritchie, R. H. "Plasma Losses by Fast Electrons in Thin Films". In: *Physical Review* 106 (5 1957), 874–881.

[14] Mahan, G. D. *Many-particle physics*. Springer Science & Business Media, 2013.

[15] Kong, J. Rose, A. Yang, C. Wu, X. Merlo, J. Burns M. Naughton, M. and Kempa, K. "Hot electron plasmon-protected solar cell". In: *Optics Express* 23 (2015).

[16] Tsuei, K. D. Plummer, E. W. Liebsch, A. Kempa, K. and Bakshi, P. "Multipole Plasmon Modes at a Metal Surface". In: *Physical Review Letters* 64 (1 1990), 44–47.

[17] Tsuei, K. D. Plummer, E. W. Liebsch, A. Pehlke, E. Kempa, K. and Bakshi, P. "The normal modes at the surface of simple metals". In: *Surface Science* 247 (1991), 302–326.

[18] Cummings, Jorden A. and Sanders, Lee. *Introduction to Psychology*. 1st. Canada: Simple Book Publishing Pressbooks, 2019.

[19] Lubik, S. and Garnsey, E. "Commecializing nanotechnology innovations from university spin-out companies". In: *Nanotechnology Perceptions* 4 (3 2008), 225–238. DOI: {10.4024/N23LU08A.ntp.04.03}.

[20] McGovern, C. "Commoditization of nanomaterials". In: *Nanotechnology Perceptions* 6 (2010), 155–178. DOI: {10.4024/N15GO10A.ntp.06.03}.

[21] Schurig, D. Mock, J. J. Justice, B. J. Cummer, S. A. Pendry, J. B. Starr, A. F. and Smith, D. R. "Metamaterial Electromagnetic Cloak at Microwave Frequencies". In: *Science* 314 (2006), 977–980.

[22] Alù, Andrea and Engheta, Nader. "Achieving transparency with plasmonic and metamaterial coatings". In: *Physical Review E* 72 (2005). DOI: {10.1103/PhysRevE.72.016623}.

[23] Pendry, J. B. "Negative Refraction Makes a Perfect Lens". In: *Physical Review Letters* 85 (18 2000), 3966–3969.

[24] Fang, Nicholas Lee, Hyesog Sun, Cheng and Zhang, Xiang. "Sub-Diffraction-Limited Optical Imaging with a Silver Superlens". In: *Science Reports* 308 (2005), 534–537.

[25] Landy, N. I. Sajuyigbe, S. Mock, J. J. Smith, D. R. and Padilla, W. J. "Perfect Metamaterial Absorber". In: *Physical Review Letters* 100 (2008). DOI: {10.1103/PhysRevLett.100.207402}.

[26] Aliei, Kamil Boratay and Ekmel, Özbay. "Radiation properties of a split ring resonator and monopole composite". In: *Physica Status Solidi (b)* 244 (4 2007), 1192–1196. DOI: {10.1002/pssb.200674505}.

[27] Modi, Anuj Y. Alyahya, Meshaal A. Balanis, Constantine A. and Birtcher, Craig R. "Metasurface-Based Method for Broadband RCS Reduction of Dihedral Corner Reflectors With Multiple Bounces". In: *IEEE Transactions on Antennas and Propagation* 68 (3 2020), 1436–1447.

[28] Pendry, J. B. Holden, A. J. Robbins, D. J. and Stewart, W. J. "Magnetism from Conductors and Enhanced Nonlinear Phenomena". In: *IEEE Transactions on Microwave Theory and Techniques* 47 (11 1999), 2075–2084.

[29] Cutraro, Jennifer. “How Creativity Powers Science”. In: *Science News Explores* (2012).

[30] Kumar, N. Suresh Naidu, K. Chandra Babu Banerjee, Prasun Babu, T. Anil. and Reddy, B. Venkata Shiva. “A Review on Metamaterials for Device Applications”. In: *Crystals* 11 (5 2021), 518. DOI: {10.3390.cryst11050518}.

[31] Kempa, K. “Percolation effects in the checkerboard Babinet series of metamaterial structures”. In: *Physica Status Solidi RRL* 4 (2010), 218–220.

[32] Urade, Y. Nakata, Y. Nakanishi, T. and Kitano, M. “Frequency-Independent Response of Self-Complimentary Checkerboard Series”. In: *Physical Review Letters* 114 (23 2015).

[33] Wilson, Kenneth G. “Renormalization Group and Critical Phenomena”. In: *Nobel lecture, Cornell University* (1982).

[34] da Costa, R. A. Dorogovstev, S. N. Goltsev, A. V. and Mendes, J. F. F. “Explosive Percolation Transition is Actually Continuous”. In: *Physical Review Letters* 105 (2010), 255701. DOI: {10.1103/PhysRevLett.105.255701}.

[35] Babinet, A. “Memoires d’optique meteorologique”. In: *Compt. Rend. Acad. Sci.* 4 (1837), 683.

[36] Booker, H. G. “Slot Aerials and Their Relation to Complementary Wire Aerials (Babinet’s Principle)”. In: *Journal of the Institution of Electrical Engineering* 93 (4 1946), 620–626.

[37] Tan, Z. M. and McDonald, K. T. “Babinet’s Principle for Electromagnetic Fields”. In: *Princeton University* (2016).

[38] Chen H-T. O’Hara, J. F. Taylor, A. J. Averitt, R. D. Highstrete, C. Lee, M. and Padilla, W. J. “Complementary planar terahertz metamterials”. In: *Optics Express* 15 (2007), 1084.

[39] Zentgraf, T. Meyrath, T. P Seidel, A. Kaiser, S. Giessen, H. Rockstuhl, C. and Lederer, F. “Babinet’s principle for optical frequency metamaterials and nanoantennas”. In: *Physical Review B* 76 (2007).

[40] Pendry, J. B. Martin-Moreno, L. and Garcia-Vidal, F. J. “Mimicking surface plasmons with structured surfaces”. In: *Science* 305 (2004), 847.

[41] Balanis, C. A. *Antenna Theory; Analysis and Design*. 3rd. United States of America: Wiley-Interscience, 2005.

[42] Lodge, O. J. “Electric Telegraphy”. Pat.

[43] *COMSOL Multiphysics*. https://comsol.com/. Version 4, 5, 6. COMSOL Inc.

[44] Chen, W. C., Landy, N. I. Kempa, K. and Padilla, W. J. “A subwavelength extraordinary-optical-transmission channel in Babinet metamaterials”. In: *Advances in Optical Materials* 1 (2013), 221–226. DOI: {10.1002/adom.201200016}.

[45] Zeman, E. J. and Schatz, G. C. "An accurate electromagnetic theory study of surface enhancement factors for silver, gold, copper, lithium, sodium, aluminum, gallium, indium, zinc, and cadmium". In: *Journal of Physical Chemistry* 91 (3 1987), 634–643.

[46] Joe, Yong S. Satanin, Arkady M. and Kim, Chang Sub. "Classical analogy of Fano resonances". In: *Physica Scripta* 74 (2006), 259–266. DOI: {10.1088/0031-8949/74/2/020}.

[47] Hofstadter, D. R. "Energy levels and wave functions of Bloch electrons in rational and irrational magnetic fields". In: *Physical Review B* 14 (6 1976), 2239.

[48] Kuhl, U. and Stöckmann, H. J. "Microwave Realization of the Hofstadter Butterfly". In: *Physical Review Letters* 80 (15 1998), 3232–3235.

[49] Wu, R. F. Pan, W. Shi, S. L. and Han, R. B. "Critical behaviors of the conductivity and dielectric constant of Ti3SiC2/Al2O3 hybrids". In: *Journal of Applied Physics* 102 (5 2007).

[50] Last, B. J. and Thouless, D. J. "Percolation Theory and Electrical Conductivity". In: *Physical Review Letters* 27 (25 1971), 1719–1721.

[51] Cardy, J. *Scaling and Renormalization in Statistical Physics*. Cambridge University, 1996.

[52] Bergman, D. J. and Imry, Y. "Critical Behavior of the Complex Dielectric Constant near the Percolation Threshold of a Heterogeneous Material". In: *Physical Review Letters* 39 (19 1977), 1222–1225.

[53] Chen, C. C. "Transmission through a Conducting Screen Perforated Periodically with Aperatures". In: *IEEE Transmission Microwave Theory Technology* 18 (9 1970), 627–632. DOI: {10.1109/TMTT.1970.1127298}.

[54] Garcia de Abajo, F. J. "Light scattering by particle and hole arrays". In: *Reviews of Modern Physics* 79 (4 2007), 1267–1290. DOI: {10.1103/RevModPhys.79.1267}.

[55] Maqsood, M. M. Mehfuz, R. and Chau, K. J. "High-throughput diffraction-assisted surface-plasmon-polariton coupling by a super-wavelength slit". In: *Optics Express* 18 (21 2010), 21669–21677. DOI: {10.134/OE.19.010429}.

[56] Akinoglu, E. M. Luo, L. Dodge, T. Akinoglu, G. E. Wang, X. Shui, L. Zhou, G. Naughton, M. J. Kempa, K. and Giersig, M. "Extraordinary optical transmission in nano-bridged plasmonic arrays mimicking a stable weakly-connected percolation threshold". In: *Optics Express* 28 (2020), 31425. DOI: {10.1364/OE.403034}.

[57] Hecht, E. *Optics*. 2nd. United States of America: Addison Wesley, 2002.

[58] Born, M. and Wolf, E. *Principles of Optics*. 7th. Cambridge University Press, 1999.

[59] Cai, Yuan Zhou, Sheng Ma, Xiaofeng and Lui, Dingquan. "Fabrication of short-wavelength infrared dual-band-pass filter based on combination of Fabry-Perot filters". In: *Applied Optics* 55 (33 2016), 9412–9416. DOI: {10.1364/AO.55.009412}.

[60] Jen, Yi-Jun Lee, Cheng-Chung Lu, Kun-Han Jheng, Ci-Yao, and Chen, Yu-Jen. "Fabry-Perot based metal-dielectric multilayerd filters and metamaterials". In: *Optics Express* 23 (26 2015), 33008–33017. DOI: {10.1364/OE.23.033008}.

[61] Sakai, Kiyomi Fukui, Takashi Tsunawaki, Yoshiaki and Yoshinaga, Hiroshi. "Metallic Mesh Bandpass Filters and Fabry-Perot Interferometer for the Far Infrared". In: *Japanese Journal of Applied Physics* 8 (8 1969), 1046. DOI: {10.1143/JJAP.8.1046}.

[62] Sardana, Neha Talalaev, Vadim Heyroth, Frank Schmidt, Georg Bohley, Christain Sprafke, Alexander and Schilling, Joerg. "Localized surface plasmon resonance in the IR regime". In: *Optics Express* 24 (1 2015), 254. DOI: {10.1364/OE.24.000245}.

[63] Goodman, J. *Introduction to Fourier Optics*. 2nd. McGraw-Hill, 1996.

[64] Tavakoli, Mehdi Jalili, Yousef Seyed and Elahi, Seyed Mohammad. "Rayleigh-Wood anomaly approximation with FDTD simulation of plasmonic gold nanohole array for determination of optimum extraordinary optical transmission characteristics". In: *Superlattices and Microstructures* 130 (2019), 454–471. DOI: {10.1016/j.spmi.2019.04.035}.

[65] Kim, Kyoung-Youm Chong, Xinyuan Ren, Fanghui and Wang, Alan X. "Slow-light effect via Rayleigh anomaly and the effect of finite gratings". In: *Optics Letters* 40 (22 2015), 5339–5342. DOI: {10.1364/OL.40.005339}.

[66] Luo, Lingpeng Akinoglu, Eser Metin Wu, Lihua Dodge, Tyler Wang, Xin Zhou, Guofu Naughton, Michael J. Kempa, Krzysztof and Giersig, Michael. "Nano-bridged nanosphere lithography". In: *Nanotechnology* 31 (2020). DOI: {10.1088/1361-6528/ab7c4c}.

[67] Haynes, C. L. and van Duyne, R. P. In: *Journal of Physical Chemestry B* 105 (2001), 5599.

[68] Zhang, X. Yonzon, C. R. and van Duyne, R. P. In: *Journal for Matter Research* 21 (2006), 1083.

[69] Han, S. Hao, Z. Wang, J. and Luo, Y. In: *Journal of Vac. Science Technology B* 23 (2005), 1585.

[70] Fan, H. J. Fuhrmann, B. Scholz, R. Syrowatka, F. Dadgar, A. Krost, A. and Zacharias, M. In: *Journal of Crystal Growth* 287 (2006), 34.

[71] Brinkert, K. Richter, M. H. Akay, Ö. Liedtke, J. Giersig, M. Fountaine, K. T. and Lewerenz, H. J. In: *Nature Communications* 9 (2018), 2527.

[72] Jensen, T. R. Malinsky, M. D. Haynes, C. L. and van Duyne, R. P. In: *Journal of Physical Chemestry B* 104 (2000), 10549.

[73] Peng, Y. Marcoux, C. Patoka, P. Hilgendorff, M. Giersig, M. and Kempa, K. In: *Applied Physics Letters* 96 (2010).

[74] Ctistis, G. Papaioannou, E. Patoka, P. Gutek, J. Fumagalli, P. and Giersig, M. In: *Nano Letters* 9 (2009).

[75] Tian, S. Wang, J. Jonas, U. and Knoll, W. In: *Chemical Materials* 17 (2005), 5726.

[76] Wood, M. A. In: *Journal of R. Soc. Interface* 4 (2007).

[77] Cai, Y. and Ocko, B. M. In: *Langmuir* 21 (2005), 9274.

[78] Li, W. D. Ding, F. Hu, J. and Chou, S. Y. "Three-dimensional cavity nanoantenna coupled plasmonic nanodots for ultrahigh and uniform surface-enhanced Raman scattering over large area". In: *Optics Express* 19 (5 2011), 3925–3936.

[79] Gu, Y. Zhang, L. Yang, J. K. W. Yeo, S. P. and Qiu, C. W. "Color generation via subwavelength plsmonic nanostructures". In: *Nanoscale* 7 (15 2015), 6409–6419.

[80] Akinoglu, G. E. Mir, S. H. Gatensby, R. Rydzek, G. and Morkarian-Tabari, P. "Block Copolymer Derived Vertically Coupled Plasmonic Arrays for Surface-Enhanced Raman Spectroscopy". In: *ACS Applied Material Interfaces* 12 (20 2020), 23410–23416.

[81] Tira, C. A. Ly, I. Vallee, R. A. L. Astilean, S. and Farcau, C. "Shaping light spectra and field profiles in metal-coated monolayers of etched microspheres". In: *Optical Materials Express* 7 (8 2017), 2847–2859.

[82] Akinoglu, G. E. Akinoglu E. M. Kempa, K. and Giersig, M. "Plasmon resonances in coupled Babinet complementary arrays in the mid-infrared range". In: *Optics Express* 27 (16 2019), 22939–22950.

[83] Williams, C. Rughoobur, G. Flewitt, A. J. and Wilkinson, T. D. "Nanostructured plasmonic metapixels". In: *Science Reports* 7 (1 2017), 7745.

[84] Cox, A. J. DeWeerd, A. J. and Linden, J. "An experiment to measure Mie and Rayleigh total scattering cross sections". In: *American Journal of Physics* 70 (6 2002), 620–625.

[85] Proietti Zaccaria, Remo. "Butterfly wing color: A photonic crystal demonstration". In: *Optics and Lasers in Engineering* 76 (2016), 70–73. DOI: {10.1016/j.optlaseng.2015.04.008}.

[86] Hwang, Dae-Kue Lee, Byunghong and Kim, Dae-Hwan. "Efficiency enhancement in solid dye-sensitized solar cell by three-dimensional photonic crystal". In: *Royal Society of Chemistry Advances* 3 (9 2013), 3017–3023. DOI: {10.1039/C2RA22746K}.

[87] Luo, Chiyan Johnson, Steven G. Joannopoulos, J. D. and Pendry, J. B. "All-angle negative refraction without negative effective index". In: *Physical Review B* 65 (2002), 201104. DOI: {10.1103/PhysRevB.65.201104}.

[88] Joannopoulos, J. D. Meade, R. D. and Winn, J. N. *Photonic Crystals: Molding the Flow of Light*. United States: Princeton University Press, 1995.

[89] Smith, D. R. Padilla, Willie J. Vier, D. C. Nemat-Nasser, S. C. and Schultz, S. "Composite Medium with Simultaneously Negative Permeability and Permittivity". In: *Physical Review Letters* 84 (18 2000), 4184. DOI: {10.1103/PhysRevLett.84.4184}.

[90] Rose, A. and Kempa, K. "Negative refraction in three-dimensional point-dipolelike polaritonic crystals". In: *Journal of Applied Physics* 108 (2010), 094301. DOI: {10.1063/1.3500323}.

[91] Jasmin, H. B. "Theoretical and Experimental Study For (CdSe) Nanoparticles". In: *ResearchGate / University of Baghdad Ph.D. Thesis* (2014).

[92] Wang, X. and Kempa, K. "Negative refraction and subwavelength lensing in a polaritonic crystal". In: *Physical Review B* 71 (2005), 233101. DOI: {10.1103/PhysRevB.71.233101}.

[93] Gorelik, V. S. and Shchavlev, V. V. "Negative Refraction in the Visible Range in Water-Infiltrated Opal Photonic Crystals". In: *Inorganic Materials* 48 (5 2012), 476–479. DOI: {10.1134/S0020168512050056}.

[94] Wang, X. and Kempa, K. "Effects of disorder on subwavelength lensing in two-dimensional photonic crystal slabs". In: *Physical Review B* 71 (2005), 085101. DOI: {10.1103/PhysRevB.71.085101}.

[95] Gorelik, V. S. "Optics of Globular Photonic Crystals". In: *Laser Physics* 18 (12 2008), 1479–1500. DOI: {10.1134/S1054660X08120153}.

[96] Gorelik, V. S. Bi, Dongxue and Fei, Guang Tao. "Optical properties of mesoporous photonic crystals filled with dielectrics, ferroelectrics, and piezoelectrics". In: *Journal of Advanced Dielectrics* 7 (6 2017), 1750038. DOI: {10.1142/S2010135X17500382}.

[97] Pollard, R. J. Murphy, A. Hendren, W. R. Evans, P. R. Atkinson, R. Wurtz, G. A. Zayats, A. V. and Podolskiy, V. A. "Optical nonlocalities and additional waves in epsilon-near-zero metamaterials". In: *Physical Review Letters* 102 (2009), 127405.

[98] Ginzburg, P. and Zayats, A. V. "Localized surface plasmon resonances in spatially dispersive nano-objects: phenomenological treatise". In: *ACS Nano* 7 (2013), 4334–4342.

[99] Krasavin, Alexey Ginzburg, Pavel Wurtz, Gregory and Zayats, Anatoly. "Nonlocal nonlinear plasmonics". In: *SPIE News* (2016).

[100] Shvonski, A. J. Kong, J. and Kempa, K. "Nonlocal extensions of the electromagnetic response of plasmonic and metamaterial structures". In: *Physical Review B* 95 (2017), 045149.

[101] Baxter, Joshua Lesina, Antonio Calà and Ramunno, Lora. "Parallel FDTD Modeling of Nonlocality in Plasmonics". In: *IEEE Transactions on Antennas and Propagation* 69 (7 2021), 3982–3994. DOI: {10.1109/TAP.2020.3044579}.

[102] Yang, Fan Wang, Yao-Ting Huidobro, Paloma A. and Pendry, John B. "Nonlocal effects in singular plasmonic metasurfaces". In: *Physical Review B* 99 (2019), 165423. DOI: {10.1103/PhysRevB.99.165423}.

[103] Yang, Fan Galiffi, Emanuele Huidobro, Paloma Arroyo and Pendry, J. B. "Nonlocal effects in plasmonic metasurfaces with almost touching surfaces". In: *Physical Review B* 101 (2020), 075434. DOI: {10.1103/PhysRevB.101.075434}.

[104] Schilling, A. Cantoni, M. Guo, J. D. and Ott, H. R. "Superconductivity above 130K in the Hg-Ba-Ca-Cu-O system". In: *Nature* 363 (1993), 56–58. DOI: {10.1038/363056a0}.

[105] Ginzburg, V. L. and Kirzhnits, D. A. "On the problem of high temperature superconductivity". In: *Physics Reports* 4 (7 1972), 343–356. DOI: {10.1016/0370-1573(72)90017-8}.

[106] Kirzhnits, D. A. Maksimov, E. G. and Khomskii, D. I. "The description of superconductivity in terms of dielectric response". In: *Journal of Low Temperature Physics* 10 (1973), 79–93. DOI: {10.1007/BF00655243}.

[107] Ginzburg, V. L. "The Problem of High Temperature Superconductivity II". In: *Soviet Physics Uspekhi* 13 (3 1970), 335. DOI: {10.1070/PU1970v013n03ABEH004256}.

[108] Smolyaninov, Igor. I. and Smolyaninov, Vera N. "Theoretical modeling of critical temperature increase in metamaterial structure". In: *Physical Review B* 93 (2016), 184510. DOI: {10.1103/PhysRevB.93.184510}.

[109] Smolyaninov, Vera N. Jensen, Christopher Zimmerman, William Prestigiacomo, Joseph C. Osofsky, Michael S. Kim, Heungsoo Xing, Zhen Qazilbash, Mumtaz and Smolyaninov, Igor I. "Enhanced superconductivity in aluminum-based hyperbolic metamaterials". In: *Scientific Reports* 6 (2016), 34140. DOI: {10.1038/srep34140}.

[110] Smith, D. R. Pendry, J. B. and Wiltshire, M. C. K. "Metamaterials and Negative Refractive Index". In: *Science* 305 (5685 2004), 788–792. DOI: {10.1126/science.1096796}.

[111] Smolyaninov, Igor. I. and Smolyaninov, Vera N. "Metamaterial superconductors". In: *Nanophotonics* 7 (5 2018), 795–818. DOI: {10.1515/nanopho-2017-0115}.

[112] Mattuck, R. D. *A Guide to Feynman Diagrams in the Many-Body Problem*. United States: Dover, 1976.

[113] Kempa, Krzysztof Protik, Nakib H. Dodge, Tyler Draxl, Claudia and Naughton, Michael J. "Enhancing superconductivity with resonant antishielding and topological plasmon-polarons". In: *Physical Review B* 107 (2023), 184518. DOI: {10.1103/PhysRevB.107.184518}.

[114] Jia, Xun Zhang, Shuyuan Sankar, Raman Chou, Fang-Cheng Wang, Weihua Kempa, K. Plummer, E. W. Zhang, Jiandi Zhu, Xuetao and Guo, Jiandong. "Anamalous Acoustic Plasmon Mode from Topologically Protected States". In: *Physical Review Letters* 119 (2017), 136805. DOI: {10.1103/PhysRevLett.119.136805}.

[115] Shvonski, Alex Kong, Jiantao and Kempa, Krzysztof. "Plasmon-polaron of the topological metallic surface states". In: *Physical Review B* 99 (2019), 125148. DOI: {10.1103/PhysRevB.99.125148}.

[116] Bozovic, Ivan. "Low-energy collective electronic excitations in a polaron gas". In: *Physical Review B* 48 (1993), 876. DOI: {10.1103/PhysRevB.48.876}.

[117] Burns, G. *Solid State Physics*. United States: Academic, 1985.

[118] Lyddane, R. H. Sachs, R. G. and Teller, E. "On the Polar Vibrations of Alkali Halides". In: *Physical Review* 59 (1941), 673. DOI: {10.1103/PhysRev.59.673}.

[119] Marsiglio, F. and Carbotte, J. P. (Edited by Bennemann, K. H. and Ketterson, J. B. *Electron-Phonon Superconductivity*. Germany: Springer, 2008, 73–162.

[120] Marsiglio, F. "Eliashberg theory: A short review". In: *Annals of Physics* 417 (2020), 168102. DOI: {10.1016/j.aop.2020.168102}.

[121] Eliashberg, G. M. "Interactions between electrons and lattice vibrations in a superconductor". In: *Soviet Physics JETP* 11 (1960), 696.

[122] Margine, E. R. and Giustino, F. "Anisotropic Migdal-Eliashberg theory using Wannier functions". In: *Physical Review B* 87 (2013), 024505. DOI: {10.1103/PhysRevB.87.024505}.

[123] Leavens, C. R. "A least upper bound on the superconducting transition temperature". In: *Solid State Communications* 17 (12 1975), 1499–1504. DOI: {10.1016/0038-1098(75)90982-5}.

[124] Maksimov, E. G. Kulić, M. L. and Dolgov, O. V. "Bosonic Spectral Function and the Electron-Phonon Interaction in HTSC Cuprates". In: *Advances in Condensed Matter Physics* 2010 (2010), 423725. DOI: {10.1155/2010/423725}.

[125] Trang, C. X. Shimamura, N. Nakayama, K Souma, S. Sugawara, K. Watanabe, I Yamauchi, K. Oguchi, T. Segawa, K. Takashashi, T. Ando, Yoichi and Sato, T. "Conversion of a conventional superconductor into a topological superconductor by topological proximity effect". In: *Nature Communications* 11 (2020), 159. DOI: {10.1038/s41467-019-13946-0}.

[126] Von Neumann, J. and Richtmyer, R. D. "A Method for the Numerical Calculation of Hydrodynamic Shocks". In: *Journal of Applied Physics* 21 (3 1950), 232–237. DOI: {10.1063/1.1699639}.

[127] Taflove, Allen and Hagness, Susan C. *Computational Electrodynamics: The Finite-Difference Time-Domain Method*. 3rd. Artech House Publishers, 2005.

[128] Chew, W. C. Jin, J.-M. Michielssen, E. and Song, J. *Fast and Efficient Algorithms in Computational Electromagnetics*. Artech House Publishers, 2001.

[129] Jin, J. *The Finite Element Method in Electrodynamics*. 2nd. Wiley-IEEE Press, 2002.

[130] Harrington, R. F. *Field Computation by Moment Methods*. Wiley-IEEE Press, 1993.

[131] Albani, M. and Bernardi, P. "A numerical method based on the discretization of Maxwell's equations in intergral form". In: *IEEE Transactions on Microwave Theory and Techniques* 22 (4 1974), 446–450. DOI: {10.1109/TMTT.1974.1128246}.